Towards Brains in the Cloud

A Biophysically Realistic Computational Model of Olfactory Bulb

by

Justas Birgiolas

A Dissertation Presented in Partial Fulfillment
of the Requirements for the Degree
Doctor of Philosophy

Approved November 2019 by the
Graduate Supervisory Committee:

Sharon Crook, Chair
Richard C. Gerkin
Ronald Calhoun
Janet Neisewander
Brian H. Smith

ARIZONA STATE UNIVERSITY

December 2019

ABSTRACT

The increasing availability of experimental data and increases in computational power have resulted in increasingly detailed and sophisticated models of brain structures. Biophysically realistic models allow detailed investigations of the mechanisms that operate within those structures. In this work, published mouse experimental data were synthesized to develop an extensible, open-source platform for modeling the mouse main olfactory bulb and other brain regions. A "virtual slice" model of a main olfactory bulb glomerular column that includes detailed models of tufted, mitral, and granule cells was created to investigate the underlying mechanisms of a gamma frequency oscillation pattern ("gamma fingerprint") often observed in rodent bulbar local field potential recordings. The gamma fingerprint was reproduced by the model and a mechanistic hypothesis to explain aspects of the fingerprint was developed. A series of computational experiments tested the hypothesis. The results demonstrate the importance of interactions between electrical synapses, principal cell synaptic input strength differences, and granule cell inhibition in the formation of the gamma fingerprint. The model, data, results, and reproduction materials are accessible at https://olfactorybulb.org. The discussion includes a detailed description of mechanisms underlying the gamma fingerprint and how the model predictions can be tested experimentally. In summary, the modeling platform can be extended to include other types of cells, mechanisms and brain regions and can be used to investigate a wide range of experimentally testable hypotheses.

ACKNOWLEDGMENTS

Firstly, I would like to express my sincere gratitude for the guidance and mentorship of my advisor, Dr. Sharon Crook. Without her support as I started the Ph.D. program and her help throughout its course, I could not be where I am today. She has provided me with invaluable knowledge about research, grant writing, and lab leadership. In addition to Dr. Crook, I would like to thank Dr. Gerkin, Dr. Neisewander, Dr. Smith, and Dr. Calhoun for being a part of my committee and helping me during my time at ASU. Without their guidance and support I would not have learned nearly as much as I have. I would also like to thank other Ph.D. students in the ICON and Dr. Smith's labs: Vergil Haynes, Russell Jarvis, and Christopher Jernigan for answering questions, providing guidance, and withstanding intense, quantum-level discussions. I would also like to thank the National Institute on Deafness and Other Communication Disorders, Google, and the Arizona State Interdisciplinary Graduate Program in Neuroscience for sponsoring my research.

Thank you to all of the friends that I have made here that have contributed in their own way to my success here and in the future. Thank you, Mom, Dad, and Paulina, for your continued support. Lastly, thank you Karen Hastings for your unflinching support during the transition to graduate school and throughout the program while I started to pursue my dream to build 'the machine'.

I am truly lucky that I am surrounded by such amazing people.

TABLE OF CONTENTS

LIST OF TABLES

Table Page

LIST OF FIGURES

1 INTRODUCTION

1.1 Value of Studying the Olfactory Bulb

The mammalian main olfactory bulb is involved in neurodegenerative, mood, and substance abuse disorders. For example, olfactory impairment is predictive of future Parkinson's disease onset before the onset of motor symptoms (Ansari & Johnson, 1975; Haehner et al., 2009). While the sense of smell in humans is subtler and more underestimated than vision or hearing (McGann, 2017), its impairment can have a profound effect on well-being. Anosmia, the loss of the ability to smell, is associated with depression in humans and animal models (Gopinath, Anstey, Sue, Kifley, & Mitchell, 2011; Kelly, Wrynn, & Leonard, 1997; Negoias et al., 2010). Depression, in turn, is associated with increased likelihood of substance abuse (Kenny, 2011; Markou, Kosten, & Koob, 1998; Weiss, Griffin, & Mirin, 1992). Thus, understanding how the olfactory system functions will lead to a better understanding and treatments of these disorders.

The olfactory system is also interesting from a machine learning perspective. Each olfactory receptor can be thought as a molecular feature detector. Since animals can have thousands of different olfactory receptor types (Fleischer et al., 2009; Shepherd, 2011), the output of olfactory receptor neurons can be viewed as a high dimensional vector that encodes odor information. How these high-dimensional odor vectors, which vary with time, odor concentration, and odor mixtures, are decoded by the brain as stable odor experiences, and how such decoding could be replicated with machine learning algorithms is an interesting and open research problem. If solved, such algorithms would have important implications for diagnostic, agricultural, national security, and defense applications (Fitzgerald, Bui, Simon, & Fenniri, 2017; Pobkrut, Eamsa-ard, & Kerdcharoen, 2016; Wang, Zhuang, Zou, & Hsia, 2015).

1.2 Role of the Olfactory Bulb in Odor Processing

The main and the accessory olfactory bulbs are the first regions of the brain that process olfactory information from olfactory receptor neurons in the nasal epithelium and transmit it to regions of the cortex for further downstream processing (Shepherd, 2011). Here I focus on the main olfactory bulb.

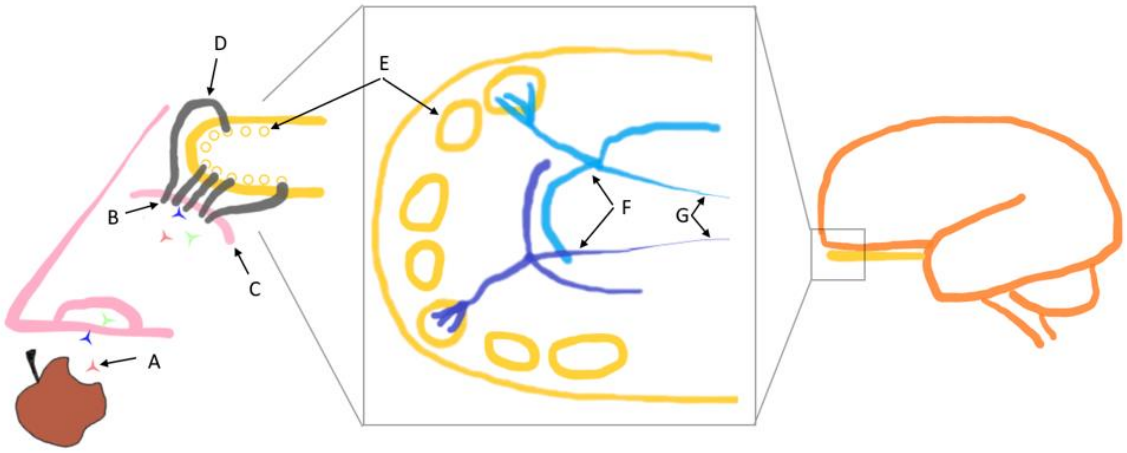

Figure 1: Overview of the Olfactory System. Odor molecules (a) enter through the nose and bind to receptors on olfactory receptor neurons (b) in the olfactory epithelium, exciting them (c). Receptor neuron axons (d) converge onto glomeruli (e) located in the outer layer of the olfactory bulb. A given glomerulus receives input from receptor neurons that express the same type of olfactory receptor. Information from the glomeruli is processed by principal projection neurons (f) in the olfactory bulb. The projection neurons relay odor information via their axons (g) to downstream brain regions for further processing.

Volatile odors enter the nasal cavity (Figure 1) and bind to antibody-like olfactory receptors that are expressed by the olfactory receptor neurons in the epithelium located in the dorsal interior nasal passage (Fleischer et al., 2009). Receptor neurons specialize in expressing a single type of olfactory receptor (Fleischer et al., 2009). The axons of receptor neurons expressing a given receptor type will converge onto one or two glomeruli, which are spherical bundles of neuropil located throughout the glomerular layer close to the surface of the olfactory bulb (Maresh, Gil, Whitman, & Greer, 2008). Mice have approximately 1,800 glomeruli, which is approximately twice the number of olfactory receptor types (Maresh et al., 2008).

The olfactory bulb is organized into a hemisphere-like concentric laminar structure (Golgi, 1875; Shepherd, 2011). The most superficial glomerular layer is followed by the deeper external plexiform layer. Next are the mitral, internal plexiform, and granule cell layers.

Within a glomerulus (Figure 2), sensory receptor neuron axons excite the apical dendrites of two main types of neurons: mitral and tufted cells (Shepherd, 2011). The somas of tufted and mitral cells are located in the external plexiform and mitral cell layers respectively (Mori, Kishi, & Ojima, 1983; Shepherd, 2011). Both tufted and mitral cells have secondary dendrites that project laterally to the surrounding portions of the external plexiform layer.

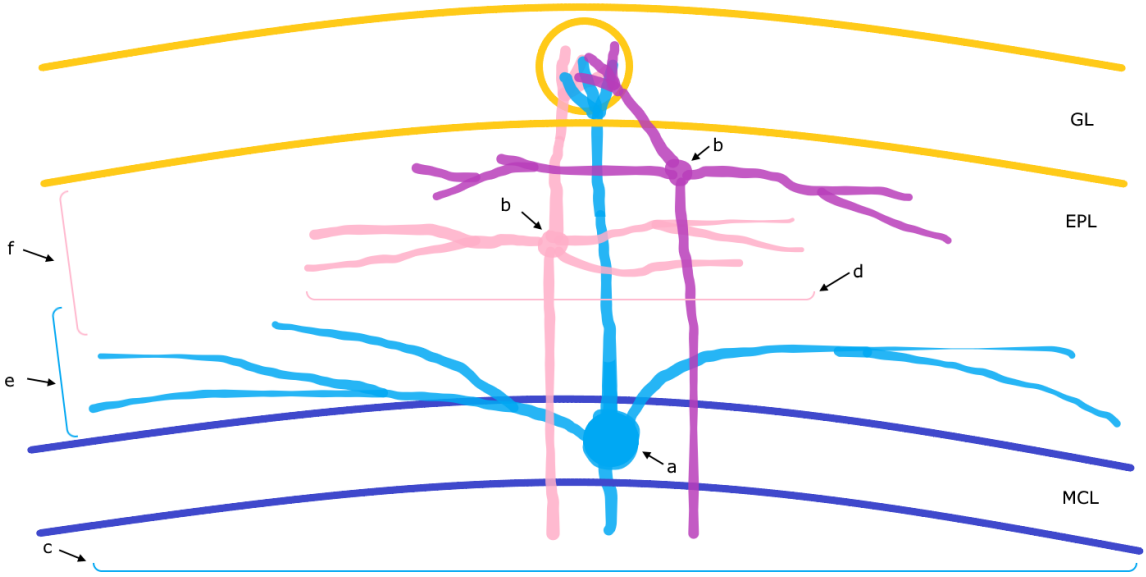

Figure 2: Morphology Differences Between Mitral and Tufted Cells. Mitral cell somas (a) are larger than tufted cell somas (b). For every mitral cell, there are 2-3 tufted cells (Benson, Ryugo, & Hinds, 1984; Purves et al., 2001; Shepherd, 1972). The extent of mitral cell lateral dendrites (c) is larger than the extent of tufted cell lateral dendrites (d). Mitral cell lateral dendrites tend to be confined to the deeper portion (e) of the external plexiform layer (EPL), while the tufted cell lateral dendrites tend to be confined to the superficial portion (f) of the EPL.

Lateral dendrites of tufted and mitral cells interact with another type of cell: the granule cell. Granule cell somas are located within the granule cell layer (Shepherd, 2011). Granule cells do not have axons, but instead they project dendrites into the

external plexiform layer where they form synapses with mitral and tufted cell dendrites (Mori et al., 1983, p. 198; Orona, Scott, & Rainer, 1983). The granule-mitral/tufted cell synapses are special dendro-dendritic reciprocal synapses (Rall, Shepherd, Reese, & Brightman, 1966). The mitral/tufted cells release excitatory glutamate onto the granule cells, while the granule cells release inhibitory γ-aminobutyric acid (GABA) back onto the mitral/tufted cells (Shepherd, 2011). Granule cells can form synapses with one or more mitral and/or tufted cells. Depending on where their apical dendrites terminate within the external plexiform layer, granule cells will preferentially form synapses with either tufted, mitral, or both cell types (Christie, Schoppa, & Westbrook, 2001; Mori et al., 1983; Shepherd, 2011).

Mitral and tufted are the only cells that project axons to the cortex (Shepherd, 2011). Both cell types project to the olfactory cortex via the lateral olfactory tract (Mori & Manabe, 2014). Top-down feedback connections from the olfactory cortex also exist. For example, the pyramidal cells in the olfactory cortex project axons into the granule cell and glomerular layers of the olfactory bulb and indirectly modulate mitral and tufted cell activity (Boyd, Kato, Komiyama, & Isaacson, 2015; Mori, 2014).

1.3 Odor Processing Parallelism

Parallel processing is a common motif in neural sensory systems. For example, the visual system divides information into color and motion pathways (Maunsell, Nealey, & DePriest, 1990), the auditory system into sound identity and location (Arnott, Binns, Grady, & Alain, 2004), and the spinal cord into touch (Brown, 1973) and pain (Jr, 1985).

The olfactory system has two pathways as well – tufted and mitral cells form two parallel pathways for relaying stimulus information from olfactory glomeruli to downstream cortical regions (Burton & Urban, 2014; Christie et al., 2001; Fukunaga, Herb, Kollo, Boyden, & Schaefer, 2014; Igarashi et al., 2012; Kishi, Mori, & Ojima,

1984; Manabe & Mori, 2013; Mori et al., 1983; Nagayama, Homma, & Imamura, 2014; Nagayama, Igarashi, Manabe, & Mori, 2014; Nagayama, Takahashi, Yoshihara, & Mori, 2004; Shao, Puche, Liu, & Shipley, 2012).

The nature and functional significance of information processing performed by each pathway is not well understood. However, cell- and network-level differences have been found between the two pathways, which provide hints for how the two sub-systems process odor information.

1.4 Mitral and Tufted Cell Sub-networks

1.4.1 Glomerular Organization Differences

The receptor neuron axons that terminate in the glomeruli release glutamate and excite the primary apical dendrites of mitral and tufted cells (Shepherd, 2011). Additionally, small, GABAergic periglomerular cells (Najac, Jan, Reguero, Grandes, & Charpak, 2011; Shao et al., 2012), and superficially located, bursting, glutamatergic external tufted cells (Nagayama et al., 2004) are excited by the receptor neurons. The periglomerular cells and the external tufted cells differentially inhibit and excite mitral and tufted cell apical tufted dendrites (Kikuta, Fletcher, Homma, Yamasoba, & Nagayama, 2013; Shao et al., 2012). Higher inhibition by periglomerular cells of mitral cells than tufted cells is thought to reduce mitral cell synaptic input and contribute to the differences in mitral and tufted cell spiking onsets within the sniff cycle (Fukunaga, Berning, Kollo, Schmaltz, & Schaefer, 2012).

Additionally, electrical synapses have been identified between the dendritic tufts of mitral cells within a glomerulus (Bourne & Schoppa, 2016; Najac et al., 2011), likely contributing to increased synchronization of mitral cells that project dendrites to the same glomerulus (O'Connor, Angelo, & Jacob, 2012). It is not clear whether tufted cell dendritic tufts are connected by similar electrical synapses.

1.4.2 Morphology Differences

Mitral cells are the largest cells in the olfactory bulb (Shepherd, 2011). They project secondary lateral dendrites to the deeper portions of the more superficially located external plexiform layer. These dendrites have a disk-like projection pattern and can span up to half-way across the bulb (Orona et al., 1983). On the other hand, the smaller tufted cells are found more superficially in the external plexiform layer (Orona et al., 1983). Similar to the mitral cells, tufted cells also have secondary lateral dendrites that project in the external plexiform layer. Deeper tufted cells tend to have more extensive lateral dendrites and project to the deeper portions of the external plexiform layer, while the more superficial tufted cells have smaller lateral dendrite extents and project more superficially within the external plexiform layer (Christie et al., 2001; Orona et al., 1983). Overall, tufted cells appear like more compact and more superficially located versions of the mitral cells.

1.4.3 Differences of Granule Cell Interactions

The mitral, tufted, and granule cells project their dendrites into the external plexiform layer where they interact via dendro-dendritic synapses (Mori et al., 1983; Rall et al., 1966; Shepherd, 2011). Mitral/tufted cells excite granule cells, which in turn inhibit mitral/tufted cell dendrites.

Granule cell somas are located throughout the granule cell layer and form three types of projection patterns (Mori et al., 1983). Some granule cells project to the superficial portion of the external plexiform layer where they form synapses with tufted cells. The somas of such granule cells tend to be located in the superficial portions of the granule layer. Other granule cells, which are distributed throughout the depths of the granule layer, project their dendrites either to the deep portions of the external plexiform layer (and thus synapse with mitral cells) or throughout the depths of the external plexiform layer (and thus synapse with both mitral and tufted cells). This

results in granule cells that preferentially interact with either mitral or tufted cells, forming parallel, mostly-separate projection networks within the olfactory bulb (Burton & Urban, 2014; Nagayama, Igarashi, et al., 2014). Granule cells that connect to both mitral and tufted cells provide means for the two pathways to interact. About 23% of granule cells mostly synapse with tufted cells, about 29% with mostly mitral cells, and about 48% synapse with both types (Mori et al., 1983).

1.4.4 Cortical Projection Differences

Mitral and tufted cells project their axons through the lateral olfactory tract into the olfactory cortex (Shepherd, 2011). However, tufted cells tend to project into the anterior part of the olfactory cortex, while the mitral cells project to the remaining areas (Nagayama, Igarashi, et al., 2014). The anterior olfactory cortex projects to the orbitofrontal cortex (Ekstrand et al., 2001; Mori, 2014; Shepherd, 2011). Thus, the tufted/mitral cell signal segregation begins in the glomerular layer and continues to be segregated in the cortex.

1.4.5 Excitability Differences

Both tufted and mitral cells fire synchronized action potentials within each sniffing cycle (Phillips, Sachdev, Willhite, & Shepherd, 2012). However, tufted cells are intrinsically more excitable (Burton & Urban, 2014; Phillips et al., 2012), respond to lower concentration odors (Fukunaga et al., 2012; Igarashi et al., 2012), and during sniffing fire in a higher gamma range (100-120 Hz) than mitral cells (40-50 Hz) (Igarashi et al., 2012; Phillips et al., 2012). Tufted cells also respond earlier in the sniff cycle than mitral cells (Igarashi et al., 2012; Phillips et al., 2012). Furthermore, mitral cell response shifts forward in the sniff cycle when the odor concentration is high (Fukunaga et al., 2012).

1.4.6 Synaptic Input Differences

Within glomeruli, both mitral and tufted cells are excited by axons of olfactory receptor neurons (Pinching & Powell, 1971; Shepherd, 2011; White, 1973), however tufted cells receive greater effective input than mitral cells. For example, in response to olfactory nerve stimulation, glomerular synapses deposit 2-3 times more charge onto tufted cells than onto mitral cells, eliciting 3-4 times more spikes in tufted than mitral cells (Burton & Urban, 2014; Gire et al., 2012). This may be due to differences in synaptic input or due to greater intra-glomerular glutamate spillover (Christie & Westbrook, 2006). Together with excitability differences between tufted and mitral cells, greater effective input is believed to cause earlier spiking onset and greater firing rates of tufted cells (Burton & Urban, 2014; Igarashi et al., 2012).

Also within glomeruli, electrical coupling and electrical synapses have been observed between pairs of mitral cells (Christie et al., 2005; Maher, McGinley, & Westbrook, 2009). Electrical synapses might exist between pairs of tufted cells (Kosaka & Kosaka, 2005); however in that study, tufted and mitral cells were not differentiated, and it is not clear if the synapses were between pairs of mitral-mitral, tufted-mitral, or tufted-tufted cells. More recently, electrical coupling has been reported between pairs of tufted cells (Ma & Lowe, 2010), suggesting the existence of electrical synapses between pairs of tufted cells. The existence of electrical synapses between tufted cells could help synchronize their spike times (Migliore, Hines, & Shepherd, 2005).

1.5 The Gamma Fingerprint

When an extracellular electrode is implanted in a rodent olfactory bulb, the resulting voltage waveform shows a stereotypical response in the gamma frequency (30-130 Hz) range. The response starts at approximately the same time relative to the onset of each sniff and contains two clusters: the early cluster oscillates at high-

gamma frequency, while the later cluster oscillates at lower gamma frequency (Fourcaud-Trocmé, Courtiol, & Buonviso, 2014; Fukunaga et al., 2014; Manabe & Mori, 2013; Zhuang, Zhang, Qin, & Wang, 2019). Here, these clusters are referred to as the "gamma fingerprint" (see Figure 2C of Manabe & Mori (2013) and Figure 2A of Zhuang et. al. (2019) for examples).

Because synaptically isolated tufted cells are more excitable than mitral cells and mostly interact with different populations of granule cells, the first cluster is attributed to activity in the tufted cell network, while the second cluster is attributed to activity of the mitral cell network. Granule cell involvement was confirmed when optogenetically silencing granule cells reduced the gamma clusters (Fukunaga et al., 2014). Similarly, multi-electrode analysis showed that gamma oscillations originate in the superficial halves of external plexiform and granule cell layers (Fourcaud-Trocmé et al., 2014), consistent with synchronized tufted and granule cell activity.

These descriptions can be further improved with a detailed, mechanistic computational model that could be used to explicitly explore the cellular and network-level mechanisms underlying the gamma fingerprint.

1.5.1 A Mechanistic Hypothesis

Experimentally observed fingerprints consist of two clusters, separated by approximately 50 ms (Manabe & Mori, 2013). The second cluster is attributed to synchronized activity in the mitral-granule cell network. However, the delay of the second cluster presents a puzzle: if mitral and tufted cells receive their inputs from a glomerulus, what causes a 50 ms delay in synchronized mitral cell activity? The combination of lower mitral cell excitability and reduced glomerular activation of mitral cells (relative to tufted cells) could result in a spike onset delay on the order of a few milliseconds, but would not be sufficient to cause a 50 ms delay. In experiments described in sections that follow, I test the hypothesis that the second cluster delay is

caused by early inhibition of mitral cells by shared granule cells activated by the more excitable and more strongly activated tufted cells. When a sufficient number of input odor spikes accumulate to offset the early inhibition, mitral cells, synchronized by electrical synapses, start spiking, resulting in the second cluster. In this hypothesis, the following components play key roles:

1) **Electrical synapses** between tufted dendrites of mitral and tufted cells cause independent synchronization of tufted and mitral cell populations, which is observable as distinct gamma clusters.
2) **Reduced mitral cell input strength** relative to tufted cells results in mitral cells requiring more time to accumulate enough excitation to start spiking.
3) Once tufted cells spike before mitral cells, they activate **granule cell inhibition** of mitral cell spikes. Only after granule cell inhibition starts subsiding do mitral cells receive enough glomerular excitation to spike.

1.6 Computational Modeling

1.6.1 Biophysically Realistic Models

Biophysically realistic models of neural systems describe cells and synapses between them as systems of coupled differential equations. These types of models explicitly model cell morphology by subdividing dendritic sections into series of cylindrical compartments (frusta) and model the ionic channel currents (e.g. Na^+, K^+, Ca^{2+}) that enter and leave the compartments (Dudani, Ray, George, & Bhalla, 2009; Hines & Carnevale, 1997; Rall et al., 1966, p. 196; Wilson, Bhalla, Uhley, & Bower, 1989). The formalism for modeling the gating of the ion channels typically follows the conductance based approach of the well-known Hodgkin-Huxley model of the giant axon of the squid (Hodgkin & Huxley, 1952). The sophistication and complexity of such models has grown with increased availability of experimental data and computing power. By utilizing supercomputers, some of these models have been used to model

entire brain regions (Bezaire, Raikov, Burk, Vyas, & Soltesz, 2016; Markram et al., 2015).

Simulations of biophysically realistic models are ideally suited for replicating common experimental interventions. Such simulations of these models allow for the simultaneous observation of the activity of modeled cells at micron and millisecond precision (Hines & Carnevale, 1997; Wilson et al., 1989). Arbitrary, deterministically reproducible simulation experiments can be performed to test mechanistic hypotheses.

For example, the effects of chemical compounds that either block or agonize ion channels or synapses can be simulated by programmatically changing ion channel or synapse model conductance parameters. The effects of opto- or chemogenetic methods that target specific cell types can be modeled by programmatically altering the properties of specific cell type models. Lesions can be simulated by programmatically excluding cells from a region of a model and truncating dendritic trees. Similarly, patch clamp, extra-cellular, and electroencephalogram recordings can be simulated by modeling the physics of the recording electrode and the propagation of electrical signals through brain tissue and bone (Dura-Bernal et al., 2016; Hines & Carnevale, 1997; Lindén et al., 2014; Parasuram et al., 2016). Overall, such models are only limited by the resources available to collect, program, and simulate the necessary level of detail (Birgiolas, Gerkin, & Crook, 2018).

1.6.2 Current Model

Extending previous modeling studies (Gilra & Bhalla, 2015a; Li & Cleland, 2013; Migliore, Cavarretta, Hines, & Shepherd, 2014; O'Connor et al., 2012; Short, Morse, McTavish, Shepherd, & Verhagen, 2016) and my group's work on validating biophysically realistic models (Birgiolas, Gerkin, & Crook, 2016; Gleeson et al., 2019), I created a biophysically detailed network model of the mouse olfactory bulb that

includes the tufted and mitral cell pathways and is validated against publicly available experimental data.

In this work, I surveyed previous olfactory bulb modeling literature to understand the progress towards understanding the components of the local field potential gamma fingerprint. This review identified several areas needing improvement within existing models. The current model builds upon the strengths of the previous models and includes modifications as described below to advance the mechanistic understanding of the dynamics of the gamma fingerprint.

1.6.2.1 Inclusion of Detailed Tufted, Mitral, and Granule Cell Models

Earlier models of the olfactory bulb do not model the tufted cells explicitly (Davison, Feng, & Brown, 2003; Li & Cleland, 2013; Migliore et al., 2015; Yu et al., 2013). Most often tufted cells are excluded or modeled as part of the same population as the mitral cells. One model does include tufted cells, but considers them as abstract point cells (Polese, Martinelli, Marco, Natale, & Gutierrez-Galvez, 2014). Because mitral and tufted cells have different electrophysiological and morphological features, which are hypothesized to contribute to the gamma fingerprint, modeling the tufted cell population separately is necessary. Similarly, different sub-populations of granule cells preferentially form synapses with the tufted or mitral cells. Thus, including detailed, morphologically realistic granule cells increases the accuracy of local field potential simulations. One model that does include detailed tufted cells (Cavarretta et al., 2018), uses reduced granule cell models consisting of few compartments. In this project, reconstructed cell morphologies were used to implement the morphology of mitral, tufted, and granule cells.

1.6.2.2 Cell Models are Rigorously Validated

Measurement error and natural and inter-species heterogeneities make it difficult to evaluate whether a cell model accurately models a neuron type. Here, I

utilized a multi-dimensional statistical validation framework implemented using the NeuronUnit package (Gerkin, Birgiolas, Jarvis, Omar, & Crook, 2019; Omar, Aldrich, & Gerkin, 2014) to evaluate how well previously-published cell models reproduce neuron behaviors. To do this, I first reviewed the olfactory bulb literature and assembled a database of adult mouse mitral, tufted, and granule cell electrophysiological and morphological measurements. Then, I assembled all previously developed mitral, tufted, and granule cell models and used NeuronUnit to subject them to the same experimental protocols that were used to obtain the assembled measurements. Finally, I evaluated how the responses of the previous models corresponded to the experimentally obtained measurements.

This approach is in contrast to other modeling studies, because here, all validation data were collected from a single species (adult mice) and protocols of each study (e.g. temperature, current injection waveform) were replicated computationally to obtain the model response to the same protocol via a simulation study. One result of the approach is a set of novel cell models that recapitulates experimental data (see "Validation of Cell Model Electrophysiology and Morphology" section).

1.6.2.3 Reconstructed Anatomical Laminar Structure

The laminar structure of the olfactory bulb does not follow a simple geometrical pattern. However, earlier models used simplified geometry. For example, one model used a linear approximation (Polese et al., 2014) of glomeruli location, which is useful in an abstract sense. Another model (Davison et al., 2003) used a planar approximation, which is accurate on a local, few-glomeruli scale. Depending on the cross-sectional orientation, the bulb is approximately spherical or ellipsoidal. A few models used this approximation (Cavarretta et al., 2018; Migliore et al., 2015; Yu et al., 2013). Because local field potentials are greatly influenced by distances to current sources, using reconstructed layer boundaries for cell placement and orientation is

expected to increase the accuracy of the simulated local field potential, which is a goal of this model.

Here, I used reconstructed mouse olfactory bulb layers from the Allen Mouse Brain Atlas ("Interactive Atlas Viewer: Atlas Viewer," 2019; Oh et al., 2014) and known mouse cell densities (Benson et al., 1984; Breton-Provencher, Lemasson, Peralta, & Saghatelyan, 2009; Gheusi et al., 2000; Pomeroy, LaMantia, & Purves, 1990; Purves et al., 2001; Royet, Souchier, Jourdan, & Ploye, 1988; Shepherd, 1972; Shepherd, Migliore, & Willhite, 2010) to populate and orient cells in the network. Additionally, the 3D layer information was used to confine mitral and tufted cell lateral dendrites to the appropriate regions within the layers. This is similar to the forcing function applied in one ellipsoidal model (Migliore et al., 2014); however, here it was made suitable for arbitrarily shaped layers. Finally, because reconstructed mouse bulb layers and cell densities were used, a proximity rule between cell dendrites (Peters & Feldman, 1976) could be used to form synapses.

1.6.2.4 An Open Olfactory Bulb Modeling Platform

In this model, significant effort was made to make the model and the new software tools used to create it accessible and easy to use. The accessibility features include: use of Python throughout the project, comments in the model code itself, adherence to Python coding style guidelines (Van Rossum, Warsaw, & Coghlan, 2001), availability of the code on open-source social-coding platform GitHub (https://github.com/justasb/olfactorybulb), model and tool documentation on how to run and modify the model, and parameterized scalability of the model. This last feature allows it to be run on single machines with multiple CPU cores (Migliore, Cannia, Lytton, Markram, & Hines, 2006), rented cloud clusters like those available through Amazon Web Services, or supercomputers at the Neuroscience Gateway

(Sivagnanam et al., 2014). In addition, all tables in this manuscript can be downloaded from the repository in Microsoft Excel format.

1.7 Results Summary

Using experimental data, previous models, and newly developed software packages, I created a biophysically realistic model of the mouse olfactory bulb that modeled the two pathways and reproduced the experimentally observed gamma fingerprint. I then performed a series of model manipulations while assessing how they affect the gamma fingerprint. These experiments demonstrate that electrical synapses, relative mitral cell input strength, and granule cell inhibition are among the major determinants of the key components of the gamma fingerprint.

The experimental data used for validation, the model source code, the documentation and tutorials, and the new software tools created to develop the model have been made available for access and extension by the neuroscience community. The new tools can be used to inspect the model and extend it with additional detail, cell types, and input and output systems.

2 METHODS

To construct this model of the olfactory bulb, I first created detailed validated models of mouse mitral, tufted, and granule cells. The cell models were then placed and oriented within the reconstructed mouse olfactory bulb layers. Mitral and tufted cell model dendrites were confined to fit within their respective regions within the external plexiform layer. A proximity algorithm was used to form reciprocal synapses between mitral/tufted and granule cells. Electrical synapses were added to the tufted dendrites of mitral and tufted cells. Odor input was simulated using a model of sniffing. During simulations, soma membrane potentials were recorded and local field potentials were computed. Band-pass filters and wavelet transforms were performed to visualize the network gamma signature. Network parameters were manually adjusted until the gamma fingerprint was observed. Finally, a series of experiments manipulating network and cell properties were performed to assess their effect on the gamma fingerprint.

2.1 Validation of Cell Model Electrophysiology and Morphology

To validate cell models, I first aggregated literature-reported relevant electrophysiology and morphology measurements of mitral, tufted, and granule cells. The experimental electrophysiology data were stored in an SQLite database and protocols and conditions used to measure it were codified within the NeuronUnit (Gerkin et al., 2019) framework as automated model tests. Then, previously developed NEURON models of mitral, tufted, and granule cells were retrieved from ModelDB (Hines, Morse, Migliore, Carnevale, & Shepherd, 2004), and subjected to the tests, resulting in measures of model deviation from experimental measurements.

Similarly, morphologies of previous models were analyzed using L-Measure (Scorcioni, Polavaram, & Ascoli, 2008) and compared to reconstructed morphologies of the three cell types. Next, ion channels from best performing models and

representative reconstructed morphologies were recombined into novel sets of models of each cell type. An optimization algorithm was used to search ion channel conductance space for parameter combinations with smaller deviations than the best earlier models. These novel models were then used in subsequent network construction.

2.1.1 Experimental Data Database

To validate cell models, 499 measurements of cell electrophysiology and morphology properties were collected from 45 publications (see next two sections for sources). An SQLite database for experimental data was developed to manage the complexity. Each publication was considered as a source of each measurement. Each measurement, consisting of a mean, standard deviation, and sample size, measured a particular electrophysiological or morphological property. Because each publication can report multiple measurements of different properties, measurements need to be linked to their source publications. Similarly, because each cell property can have multiple measurements, which can come from different publications, each measurement needs to be linked to a record of a property.

To accommodate this information structure, three tables were added to the database: source, property, and measurement (see Figure 3). The tables were linked with foreign keys that linked measurements to their properties and to their publication sources. The source table stored information about each publication, like the short author name (e.g. Shepherd et al. (2010)), article/chapter title, journal or book title, and a URL that can be used to locate the publication. The property table stored the names of cell properties like "rheobase" and "resting potential". The measurement table stored the summary statistics of each measurement and linked to records in the property and source tables.

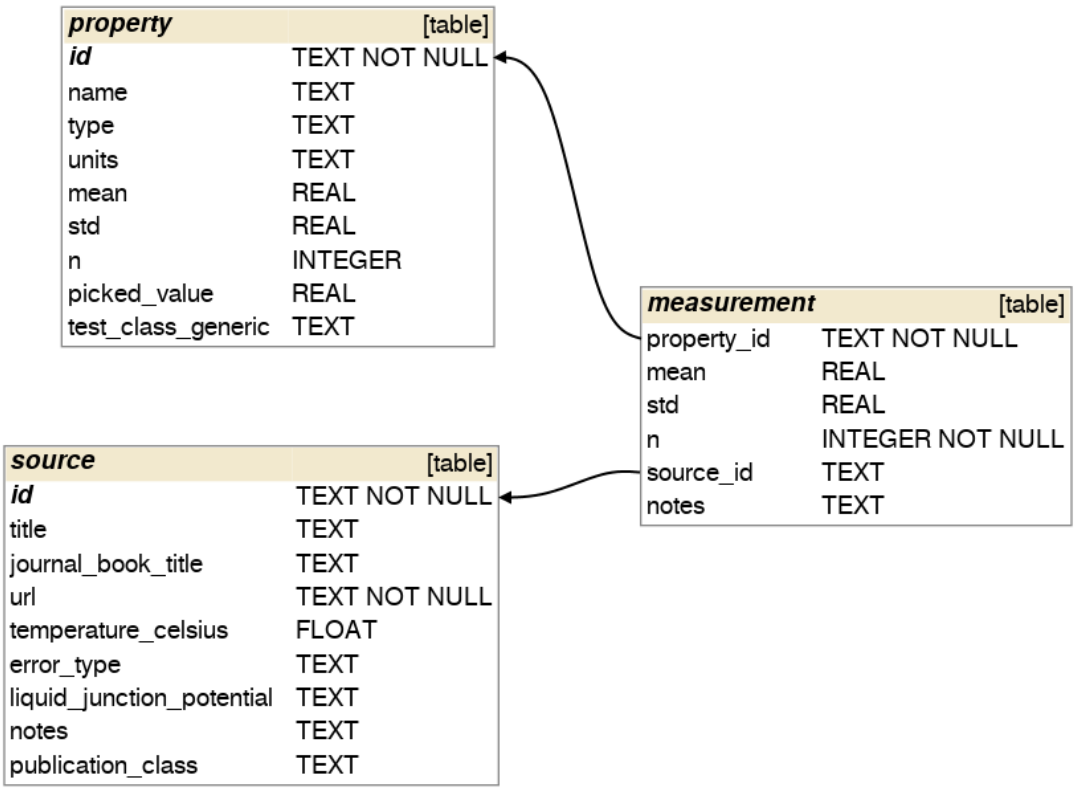

Figure 3: Experimental Data Database Tables. Measurement table contains records of measurements of experimental properties, their means, standard deviations, and sample sizes. One-to-many foreign keys (arrows) link each measurement to the experimental property it measures and to the publication (source) in which the measurement was reported. Each property can have multiple measurements (in different publications), and each publication can report multiple measurements (of different properties). When appropriate, multiple measurements of a property can be pooled together to obtain the aggregate property summary statistics.

Once all measurements from all the relevant publications were entered into the database, results from simulations of earlier cell models could be compared to these measurements easily. The peewee (Leifer, 2010/2019) object-relational mapping framework (Barry & Stanienda, 1998) was used to create Python classes that map to the database tables and write Python expressions to query the database.

2.1.2 Electrophysiology Experimental Data

A literature review was performed to identify publications reporting summary statistics (mean, sample size, and standard deviation or error) of adult mouse olfactory

bulb cell electrophysiology properties. Some publications were found via cell and species filtered search on NeuroElectro.org (Tripathy, Savitskaya, Burton, Urban, & Gerkin, 2014), others via citations in previously published models or review articles, and via NIH PubMed keyword searches. Publications were excluded if intracellular electrodes were not used, the cells were not synaptically isolated, or the publication did not report details of the stimulation protocol, or sample size and standard deviation/error. Where necessary, values were extracted from figures using WebPlotDigitizer (Rohatgi, 2011). Table 1, Table 2, and Table 3 list the electrophysiology properties whose summary statistics were collected from the previously published literature (Abraham et al., 2010; Angelo et al., 2012; Burton & Urban, 2014, 2015; Christie et al., 2005; Fukunaga et al., 2012; Hovis, Padmanabhan, & Urban, 2010; Hu, Ferguson, Whiteus, Meijer, & Araneda, 2016; Johnston & Delaney, 2010; Shpak, Zylbertal, Yarom, & Wagner, 2012; Stroh et al., 2012; Yu, Burton, Tripathy, & Urban, 2015; Zibman, Shpak, & Wagner, 2011).

Granule Cell Electrophysiology Properties

Property	μ ± σ (n)	Source
AP Afterdepolarization Depth (mV)	0 ± 2 (49)	Stroh et al. (2012)
AP Afterdepolarization Duration (ms)	42 ± 22 (49)	Stroh et al. (2012)
AP Amplitude (mV)	55.2 ± 12 (31)	Burton and Urban (2015)
AP Half-Width (ms)	1 ± 0.19 (31)	Burton and Urban (2015)
AP Threshold (mV)	-41.9 ± 7.8 (31)	Burton and Urban (2015)
Capacitance (pF)	46.1 ± 11.7 (28)	Burton and Urban (2015)
FI Curve Slope (Hz/nA)	860 ± 330 (30)	Burton and Urban (2015)
Input Resistance (MOhm)	603.2 ± 363.4 (32)	Burton and Urban (2015)
	1070 ± 390 (20)	Stroh et al. (2012)
Membrane Resting Voltage (mV)	-92 ± 4 (17)	Stroh et al. (2012)
	-84.2 ± 8.5 (40)	Burton and Urban (2015)
Membrane Time Constant (ms)	27.3 ± 13.2 (28)	Burton and Urban (2015)
Rebound Potential Presence	0 ± 1 (1)	Burton and Urban (2015)
Rheobase (pA)	37.1 ± 21.2 (31)	Burton and Urban (2015)
Sag Amplitude (mV)	-4.6 ± 1.56 (5)	Hu et al. (2016)
Spiking Rate Accommodation (Hz)	0 ± 1 (1)	Burton and Urban (2015)

Table 1: Granule Cell Electrophysiology Property Measurements

Tufted Cell Electrophysiology Properties

Property	μ ± σ (n)	Source
AHP Amplitude (mV)	16.8 ± 3.3 (12)	Burton and Urban (2014)
AHP Duration (ms)	20.5 ± 20.1 (28)	Burton and Urban (2014)
AP Amplitude (mV)	72.1 ± 5.5 (12)	Burton and Urban (2014)
AP Threshold (mV)	-55.5 ± 2.9 (12)	Burton and Urban (2014)
AP Width at Half-height (ms)	0.87 ± 0.1 (12)	Burton and Urban (2014)
Capacitance (pF)	188.8 ± 110 (28)	Burton and Urban (2014)
FI Curve Slope (Hz/nA)	406 ± 144 (28)	Burton and Urban (2014)
ISI Coefficient of Variation	0.8 ± 0.43 (28)	Burton and Urban (2014)
Input Resistance (MOhm)	89.8 ± 34.8 (6)	Fukunaga et al. (2012)
	111.8 ± 51.6 (28)	Burton and Urban (2014)
Membrane Resting Voltage (mV)	-68.5 ± 4.7 (28)	Burton and Urban (2014)
Membrane Time Constant (ms)	18.8 ± 8.6 (28)	Burton and Urban (2014)
Rebound Potential Presence	1 ± 1 (28)	Burton and Urban (2014)
Rheobase Current (pA)	94.6 ± 49.7 (28)	Burton and Urban (2014)
Sag Amplitude (mV)	-4.4 ± 6.1 (28)	Burton and Urban (2014)
Spiking Rate Accommodation (Hz)	-20.2 ± 19.1 (28)	Burton and Urban (2014)
Spiking Rate Accom. Time Const. (ms)	585 ± 664 (28)	Burton and Urban (2014)

Table 2: Tufted Cell Electrophysiology Property Measurements

Mitral Cell Electrophysiology Properties

Property	μ ± σ (n)	Source
AHP Amplitude (mV)	14.8 ± 3.2 (10)	Burton and Urban (2014)
	19.5 ± 6.2 (48)	Yu et al. (2015)
AHP Duration (ms)	5.2 ± 1.8 (48)	Yu et al. (2015)
	58.2 ± 77.5 (35)	Burton and Urban (2014)
AP Amplitude (mV)	63.2 ± 10.4 (48)	Yu et al. (2015)
	76.2 ± 5.4 (10)	Burton and Urban (2014)
AP Half-Width (ms)	1.06 ± 0.2 (10)	Burton and Urban (2014)
	1.2 ± 0.2 (48)	Yu et al. (2015)
AP Peak (mV)	16.4 ± 9 (48)	Yu et al. (2015)
AP Threshold (mV)	-55.2 ± 3 (10)	Burton and Urban (2014)
	-46.8 ± 8.7 (48)	Yu et al. (2015)
Capacitance (pF)	235.1 ± 137.1 (48)	Yu et al. (2015)
	236.4 ± 94.6 (35)	Burton and Urban (2014)
FI Curve Slope (Hz/nA)	196 ± 76 (35)	Burton and Urban (2014)
ISI Coefficient of Variation	0.31 ± 0.33 (48)	Yu et al. (2015)
	0.45 ± 0.29 (35)	Burton and Urban (2014)
Input Resistance (MOhm)	19 ± 7 (5)	Hovis et al. (2010)
	59 ± 30 (29)	Abraham et al. (2010)
	68 ± 21.9 (30)	Christie et al. (2005)
	76.2 ± 22.3 (3)	Fukunaga et al. (2012)
	94.3 ± 40.5 (35)	Burton and Urban (2014)
	128.2 ± 53.4 (48)	Yu et al. (2015)
	240 ± 110 (20)	Shpak et al. (2012)
	299 ± 135 (35)	Zibman et al. (2011)
Membrane Resting Voltage (mV)	-74.65 ± 2.7 (20)	Shpak et al. (2012)
	-71.2 ± 5.5 (48)	Yu et al. (2015)
	-66.9 ± 4 (35)	Burton and Urban (2014)
	-57 ± 17 (29)	Abraham et al. (2010)
Membrane Time Constant (ms)	14 ± 4.5 (5)	Hovis et al. (2010)
	21.3 ± 9.4 (35)	Burton and Urban (2014)
	28.1 ± 16.5 (48)	Yu et al. (2015)
	42.5 ± 16.1 (35)	Zibman et al. (2011)
Rebound Potential Presence	0 ± 1 (35)	Burton and Urban (2014)
	0 ± 1 (35)	Johnson and Delaney (2010)
Rheobase Current (pA)	111.4 ± 55.7 (35)	Burton and Urban (2014)
Sag Amplitude (mV)	-5 ± 2.93 (6)	Hu et al. (2016)
	-3.8 ± 4.1 (45)	Yu et al. (2015)
	-3.43 ± 5.8 (105)	Angelo et al. (2012)
	-2 ± 2.6 (35)	Burton and Urban (2014)
Spiking Rate Accommodation (Hz)	-9.43 ± 17.83 (35)	Burton and Urban (2014)
	15.9 ± 24.5 (35)	Zibman et al. (2011)
Spiking Rate Accom. Time Const. (ms)	113 ± 58.8 (35)	Zibman et al. (2011)
	398 ± 562 (35)	Burton and Urban (2014)

Table 3: Mitral Cell Electrophysiology Property Measurements

Some publications using rat slices reported subthreshold oscillations or bi-stability in mitral cells (Chen & Shepherd, 1997; Desmaisons, Vincent, & Lledo, 1999; Heyward, Ennis, Keller, & Shipley, 2001); however no published articles reporting summary statistics of these properties in mice were found in the literature search. Because all other experimental data to validate this model were based on mouse data, cell models were not validated against these properties.

2.1.3 Experimental Morphology Data

Morphology data to validate mitral, tufted, and granule cell model morphologies was obtained by analyzing the morphologies of reconstructed cells (Belnoue, Malvaut, Ladevèze, Abrous, & Koehl, 2016; Breton-Provencher et al., 2009; Burton, LaRocca, Liu, Cheetham, & Urban, 2017; Burton & Urban, 2014; Case et al., 2017; Dahlen, Jimenez, Gerkin, & Urban, 2011; Daroles et al., 2016; Denizet, Cotter, Lledo, & Lazarini, 2017; Fukunaga et al., 2012; Ke, Fujimoto, & Imai, 2013; McDole, Isgor, Pare, & Guthrie, 2015; Murai et al., 2016; Pun et al., 2012; Sailor et al., 2016; Siopi et al., 2016). Cell reconstructions of all three cell types were obtained from NeuroMorpho.org (Ascoli, Donohue, & Halavi, 2007) by performing a filtered search of adult mouse olfactory cell reconstructions in the control experimental condition. Each SWC morphology file in the resulting archives was manually inspected for reconstruction issues using neuTube (Feng, Zhao, & Kim, 2015). Reconstructions that did not include markers for somas or showed extremely large dendrite radius variations were excluded. Mislabeled or missing cell dendrites (e.g. all labeled as basal) were relabeled. Mitral and tufted cell reconstructions that had misplaced tufted dendrites (e.g. oriented correctly but translated ~100μm away from the soma) were corrected by translating them back to the soma. Reconstructions that did not include radius information (e.g. constant or extremely small) were labeled to not be used when

computing morphology metrics that utilized radius information. Reconstructions that did not show cell appropriate radial symmetries (e.g. thin slices) were labeled to not be used when computing morphology metrics that used depth information. No additional steps were taken to adjust for shrinkage. (However, see "2.1.5 Novel Cell Model Development" section below.)

Once the reconstructions were cleaned, a set of morphology metrics were computed for each mitral, tufted, and granule cell reconstruction (Table 4, Table 5, and Table 6). The set of metrics that are shown in the detailed view of reconstructions on NeuroMorpho.org were the metrics chosen to analyze cell reconstructions. The pyLMeasure Python package (Birgiolas, 2019/2019c) that wraps L-Measure (Scorcioni et al., 2008) functionality was used when writing NeuronUnit morphology tests and to compute all metrics. The definitions of each metric and how they are computed can be seen in L-Measure documentation ("L-Measure functions," n.d.). Once computed, the metrics were pooled across publications to obtain summary statistics (mean and standard deviation) for each metric for each cell type.

Morphology Metrics of Mitral Cell Reconstructions

Number of Stems		5.56 ± 1.69 (61)
Soma Surface Area (μm^2)		1,479.25 ± 667.19 (61)
	Apical Dendrite	*Basal Dendrite*
Mean Bifurcation Angle Local (°)	85.88 ± 14.59 (52)	74.93 ± 21.61 (61)
Mean Bifurcation Angle Remote (°)	68.65 ± 17.10 (52)	43.52 ± 18.33 (61)
Mean Contraction	0.78 ± 0.16 (52)	0.74 ± 0.07 (48)
Mean Diameter (µm)	1.52 ± 1.36 (52)	0.99 ± 0.29 (48)
Mean Rall's Ratio	1.20 ± 0.21 (52)	0.99 ± 0.35 (48)
Fractal Dimension	1.05 ± 0.13 (52)	1.04 ± 0.02 (61)
Max Branch Order	8.30 ± 2.84 (52)	2.85 ± 2.06 (61)
Max Euclidean Distance (µm)	252.40 ± 57.82 (52)	667.44 ± 209.90 (61)
Max Path Distance (µm)	346.41 ± 91.53 (52)	847.76 ± 208.91 (61)
Number of Bifurcations	18.30 ± 8.66 (17)	9.18 ± 7.32 (26)
Number of Branches	32.07 ± 19.52 (17)	20.87 ± 10.53 (26)
Overall Depth (µm)	114.15 ± 48.82 (17)	180.29 ± 96.33 (26)
Overall Height (µm)	137.19 ± 67.80 (52)	898.30 ± 359.43 (61)
Overall Width (µm)	165.84 ± 73.02 (52)	329.05 ± 234.91 (61)
Partition Asymmetry	0.47 ± 0.15 (52)	0.33 ± 0.20 (61)
Total Length (µm)	730.59 ± 182.25 (17)	4,644.17 ± 2,630.20 (26)
Total Surface (μm^2)	3,737.63 ± 1,021.03 (17)	21,375.40 ± 8,921.32 (13)
Total Volume (μm^3)	3,016.61 ± 635.19 (17)	7,225.05 ± 3,575.24 (13)

Sources:
Burton and Urban (2014), Burton et al. (2017), Case et al. (2017), Fukunaga et al. (2012), Ke et al. (2013), Murai et al. (2016)

Table 4: Statistics of Morphology Metrics of Mitral Cell Reconstructions

Morphology Metrics of Tufted Cell Reconstructions

Number of Stems		4.23 ± 2.21 (37)
Soma Surface Area (μm^2)		1,097.46 ± 587.27 (37)
	Apical Dendrite	*Basal Dendrite*
Mean Bifurcation Angle Local (°)	91.71 ± 6.84 (37)	79.99 ± 32.04 (37)
Mean Bifurcation Angle Remote (°)	70.75 ± 6.26 (37)	46.44 ± 21.16 (37)
Mean Contraction	0.79 ± 0.06 (37)	0.71 ± 0.19 (37)
Mean Diameter (µm)	0.94 ± 0.28 (37)	1.04 ± 0.23 (37)
Mean Rall's Ratio	1.27 ± 0.15 (37)	0.89 ± 0.43 (37)
Fractal Dimension	1.07 ± 0.02 (37)	1.03 ± 0.14 (37)
Max Branch Order	10.62 ± 4.81 (37)	2.52 ± 2.10 (37)
Max Euclidean Distance (µm)	174.57 ± 44.13 (37)	435.20 ± 179.56 (37)
Max Path Distance (µm)	274.00 ± 65.42 (37)	699.56 ± 236.47 (37)
Number of Bifurcations	23.02 ± 27.57 (8)	4.88 ± 3.14 (8)
Number of Branches	77.70 ± 53.10 (8)	13.05 ± 5.62 (8)
Overall Depth (µm)	97.80 ± 57.83 (8)	77.11 ± 94.13 (8)
Overall Height (µm)	115.51 ± 51.40 (37)	569.14 ± 286.67 (37)
Overall Width (µm)	92.05 ± 39.73 (37)	177.18 ± 130.90 (37)
Partition Asymmetry	0.52 ± 0.10 (37)	0.28 ± 0.21 (37)
Total Length (µm)	1,049.13 ± 478.38 (8)	1,617.03 ± 1,156.48 (8)
Total Surface (μm^2)	2,902.06 ± 1,881.73 (8)	8,368.72 ± 3,231.42 (8)
Total Volume (μm^3)	1,351.55 ± 1,127.77 (8)	1,663.74 ± 1,099.35 (8)

Sources:
Burton and Urban (2014), Burton et al. (2017), Fukunaga et al. (2012)

Table 5: Statistics of Morphology Metrics of Tufted Cell Reconstructions

Morphology Metrics of Granule Cell Reconstructions

Number of Stems		2.67 ± 1.21 (149)
Soma Surface Area (μm^2)		263.15 ± 181.14 (149)
	Apical Dendrite	*Basal Dendrite*
Mean Bifurcation Angle Local (°)	76.86 ± 20.51 (499)	8.05 ± 26.93 (482)
Mean Bifurcation Angle Remote (°)	45.97 ± 15.62 (499)	6.74 ± 23.20 (482)
Mean Contraction	0.92 ± 0.04 (412)	0.16 ± 0.34 (401)
Mean Diameter (µm)	1.02 ± 0.20 (357)	0.22 ± 0.50 (401)
Mean Rall's Ratio	1.97 ± 0.20 (357)	0.12 ± 0.64 (401)
Fractal Dimension	1.02 ± 0.03 (499)	0.31 ± 0.48 (488)
Max Branch Order	3.36 ± 1.61 (499)	0.23 ± 0.68 (482)
Max Euclidean Distance (µm)	241.16 ± 84.02 (499)	11.36 ± 24.08 (488)
Max Path Distance (µm)	285.48 ± 96.92 (499)	13.63 ± 25.97 (488)
Number of Bifurcations	2.67 ± 1.83 (45)	0.28 ± 0.47 (39)
Number of Branches	6.45 ± 4.48 (45)	2.14 ± 1.53 (45)
Overall Depth (µm)	41.59 ± 53.56 (45)	6.10 ± 7.48 (45)
Overall Height (µm)	223.42 ± 81.14 (499)	9.15 ± 21.41 (488)
Overall Width (µm)	59.32 ± 39.90 (499)	7.45 ± 15.90 (488)
Partition Asymmetry	0.47 ± 0.22 (499)	0.01 ± 0.07 (482)
Total Length (µm)	421.69 ± 375.10 (45)	38.85 ± 34.08 (45)

Sources:
Belnoue et al. (2016), Breton-Provencher et al. (2016), Dahlen et al. (2011), Daroles et al. (2016), Denizet et al. (2017), McDole et al. (2015), Pun et al. (2012), Sailor et al. (2016), Siopi et al. (2016)

Table 6: Statistics of Morphology Metrics of Granule Cell Reconstructions

2.1.4 Evaluation of Previous Cell Models

ModelDB (Hines et al., 2004; McDougal et al., 2015) was searched to identify previously developed models of olfactory bulb mitral, tufted, or granule cells (Bhalla & Bower, 1993; Chen, Shen, Shepherd, Hines, & Midtgaard, 2002; David, Linster, & Cleland, 2008; Davison, Feng, & Brown, 2000; Djurisic, Popovic, Carnevale, & Zecevic, 2008; Kaplan & Lansner, 2014; Li & Cleland, 2013; McTavish, Migliore, Shepherd, & Hines, 2012; Migliore et al., 2014, 2015, 2005; Migliore, Inzirillo, & Shepherd, 2007; Migliore & McTavish, 2013; Migliore & Shepherd, 2008; O'Connor et al., 2012; Rubin & Cleland, 2006; Saghatelyan et al., 2005; Shen, Chen, Midtgaard, Shepherd, & Hines, 1999; Short et al., 2016; Yu et al., 2013). Only models that were implemented in

NEURON (Hines & Carnevale, 1997) and modeled cells or cell networks were included for evaluation. To prepare models for evaluation, each cell model was isolated programmatically (inputs disconnected). Default or control condition ion channel conductance values were used.

The protocols used to measure experimental values of electrophysiology properties listed in Table 1 were codified into NeuronUnit tests. Most publications used slightly different protocols when measuring the property values (e.g. different length of current injection, different definition of action potential threshold). To remove this source of variability and to evaluate the models more fairly, each publication protocol was codified into its own NeuronUnit test. Each cell model's result in response to a publication's protocol to measure a property was compared to that publication's property summary statistics. Model deviation from a publication reported property value was computed as a Z-score. Model deviations from a set of experimental measurements of the same property under different conditions (e.g. rheobase current with different current injection duration or temperature) were combined by weighing each publication Z-scores by the publication reported sample sizes. Thus, each model and property combination received a "combined Z-score", which aggregated the property's sample-size-weighted Z-scores across publications.

To evaluate a model's overall correspondence to electrophysiology data, the combined Z-scores across electrophysiology properties reported for that cell type were aggregated to an overall model score by taking the square root of the sum of combined Z-score squared values (RMSE).

Model morphologies were evaluated separately from electrophysiology. Each model's morphology was extracted via conversion to the SWC format via the use of the Python hoc2swc package (Birgiolas, 2019/2019a, p. 2), and the pyLMeasure package was used to compute morphology metrics listed in Table 4, Table 5, and Table

6. Once computed, each model's morphology metrics were compared to corresponding experimental distributions (see the tables above) by computing the model-metric combination's Z-score. As for electrophysiology, the overall model morphology score was the square root of the sum of the squared Z-scores of each metric.

Mitral Cell Model Validation Results

	RMSE	AfterHyperpolarizationAmplitude	AfterHyperpolarizationTime	CellCapacitance	FISlope	ISICV	InputResistance	MembraneTimeConstant	ReboundSpiking	RestingVoltage	Rheobase	SagVoltage	SpikeAccommodation	SpikeAccommodationTimeConstant	SpikeAmplitude	SpikeHalfWidth	SpikePeak	SpikeThreshold
Birgiolas2020 MC1	2.4	-0.1	0.2	0.2	0.3	-0.4	0.6	0.2	0.0	0.8	0.1	0.8	-0.4	-1.2	-0.4	0.9	0.4	1.0
Birgiolas2020 MC5	3.5	0.0	0.4	-0.1	-0.5	-0.2	0.4	-0.2	0.0	0.1	0.4	0.8	0.4	2.9	-0.2	0.4	0.7	1.1
Birgiolas2020 MC2	3.9	1.2	1.5	-0.1	-0.5	0.2	0.3	-0.3	0.0	0.4	0.4	0.8	0.2	2.9	0.3	0.9	0.5	0.2
Birgiolas2020 MC3	3.9	-1.1	-0.1	0.6	-0.3	-0.5	-0.6	-0.5	0.0	-0.3	-0.2	0.8	0.2	3.0	0.8	1.4	0.9	0.0
Birgiolas2020 MC4	4.1	0.8	-0.4	0.3	-1.9	-0.5	-0.4	-0.4	0.0	0.9	0.4	0.8	0.1	2.9	0.4	0.4	0.9	0.4
Shen1999	4.8	0.6	1.9	0.0	0.7	-0.2	0.2	-0.3	0.0	0.3	0.9	0.7	-0.1	3.0	-0.4	-2.6	0.0	0.4
Saghatelyan2005	5.7	1.4	0.0	-0.2	0.2	-1.2	0.5	-0.2	0.0	0.3	0.4	0.7	-0.1	2.9	1.8	2.9	2.6	1.0
Migliore2008	6.0	-0.3	-0.1	-0.4	1.6	-1.2	-0.5	-1.1	0.0	0.5	0.6	0.7	-0.1	3.0	2.8	2.2	2.7	-0.3
Migliore2007	6.2	-0.3	-0.3	-0.4	1.8	-1.1	-0.5	-1.1	0.0	0.5	0.6	0.7	-0.1	3.0	2.8	2.8	2.6	-0.3
McTavish2012	6.3	-0.5	-0.1	-0.3	1.5	-1.1	-0.7	-1.1	0.0	0.5	1.0	0.7	-0.1	3.0	2.8	2.9	2.6	-0.3
Short2016	6.3	-0.5	-0.1	-0.3	1.5	-1.1	-0.7	-1.1	0.0	0.5	1.0	0.7	-0.1	3.0	2.8	2.9	2.6	-0.3
MiglioreMcTavish2013	6.3	-0.5	-0.1	-0.4	1.9	-1.1	-0.7	-1.2	0.0	0.5	0.9	0.7	-0.1	3.0	2.8	2.8	2.6	-0.3
Migliore2005GJs	6.4	0.1	-0.2	-0.9	2.3	-1.1	0.2	-1.2	0.0	0.5	0.1	0.7	-0.1	2.9	2.6	2.8	2.8	0.1
Yu2012	6.4	-0.6	-0.1	-0.4	1.9	-1.2	-0.7	-1.2	0.0	0.5	0.9	0.7	-0.1	2.9	2.8	2.9	2.6	-0.3
Chen2002	6.9	-0.1	-1.2	-0.4	-0.5	-0.1	0.4	-0.6	0.0	1.0	-1.4	0.7	0.1	6.0	0.6	-2.1	0.1	-0.8
BhallaBower1993	7.2	0.0	-1.1	3.9	-1.8	1.0	-1.0	0.9	0.0	0.8	2.0	0.8	-0.4	3.4	0.7	-3.5	0.9	0.5
LiCleland2013	7.5	3.2	3.2	-1.1	-1.9	0.4	2.8	-0.4	0.0	0.2	0.1	0.7	0.8	3.0	-0.2	-3.4	0.8	1.3
David2008	8.9	1.1	-0.9	5.1	-2.1	0.6	-0.1	3.8	0.0	0.8	0.3	0.8	-1.5	3.1	0.5	-4.0	1.3	1.3
Djurisic2008	9.1	1.1	-2.0	-1.2	-2.6	-1.2	3.7	-0.3	0.0	1.0	3.8	0.7	-0.1	4.7	-1.5	-3.4	-0.4	1.4
Migliore2014	9.2	1.1	-0.9	0.4	-2.6	-1.1	-1.9	-1.8	0.0	0.5	6.0	0.7	-0.1	2.9	3.2	1.6	3.0	-0.4
Migliore2015	9.2	1.4	-1.0	0.6	-2.6	-1.1	-1.9	-1.7	0.0	0.5	6.0	0.7	-0.1	2.9	3.2	1.0	3.1	-0.3
Davison2000	9.5	1.2	-1.0	5.3	-2.2	1.0	-0.1	3.9	0.0	0.8	0.7	0.8	0.5	3.2	0.6	-4.5	2.0	1.3
Oconnor2012 MC2	10.6	-2.4	-2.0	-1.1	-2.2	-1.2	-1.2	-1.8	0.0	0.5	2.4	0.7	-0.1	4.7	3.5	6.0	3.4	1.0
Oconnor2012 MC5	10.8	0.1	-0.2	-0.3	-2.6	-0.7	-1.7	-1.7	0.0	-0.1	6.0	0.7	-2.0	3.0	3.2	5.5	3.6	0.3
Oconnor2012 MC6	10.9	-0.8	-2.0	-0.5	-2.6	-1.2	-1.7	-1.8	0.0	0.5	6.0	0.7	-0.1	4.7	2.2	5.0	3.2	1.1
Oconnor2012 MC3	11.2	-1.9	0.5	-1.2	-2.6	-0.8	-1.6	-1.9	0.0	0.5	6.0	0.7	-2.2	3.0	2.3	6.0	3.5	1.3
Oconnor2012 MC1	11.5	0.5	-0.1	-1.5	-2.6	-1.1	-1.6	-2.0	0.0	0.4	6.0	0.7	-0.1	4.7	2.4	6.0	3.7	1.4
RubinCleland2006	12.2	3.4	2.1	1.4	-2.6	0.7	-2.0	-1.7	0.5	1.3	6.0	2.6	0.5	6.0	3.6	-2.8	3.8	0.2
KaplanLansner2014	12.5	1.2	6.0	5.3	-1.0	1.9	-0.1	3.9	0.0	0.8	0.7	0.8	-5.6	3.1	0.8	-4.6	2.0	1.3
Oconnor2012 MC4	12.8	-0.4	6.0	-1.1	-2.6	-1.2	-1.0	-1.7	0.0	0.6	5.9	0.7	-0.1	4.7	1.0	6.0	3.2	2.9

Table 7: Mitral Cell Model Electrophysiology Validation Results. Left column lists the cell models that were compared to experimental electrophysiology data. The columns on the right show the electrophysiology properties computed for each model and their combined, sample size weighed Z-scores relative to the experimental distributions. RMSE column shows each model's overall score. The rows are sorted by RMSE. Z-scores were clamped to ±6 standard deviations. Models developed for this dissertation are the first five rows.

Tufted Cell Model Validation Results

	RMSE	AfterHyperpolarizationAmplitude	AfterHyperpolarizationTime	CellCapacitance	FISlope	ISICV	InputResistance	MembraneTimeConstant	ReboundSpiking	RestingVoltage	Rheobase	SagVoltage	SpikeAccommodation	SpikeAccommodationTimeConstant	SpikeAmplitude	SpikeHalfWidth	SpikeThreshold
Birgiolas2020 TC3	3.6	-0.6	-1.0	-0.9	-1.4	-0.6	0.7	-0.7	-1.0	-0.3	-0.5	0.9	0.1	-0.2	0.1	0.0	2.3
Birgiolas2020 TC4	3.7	-0.3	-1.0	-0.8	-2.3	-0.6	1.0	-0.4	0.0	0.5	0.2	1.6	-0.7	-0.6	0.7	0.0	0.9
Birgiolas2020 TC5	3.8	0.4	-1.0	-1.6	-0.5	-0.7	-0.2	-2.1	0.0	1.0	-0.8	1.0	1.1	-0.5	0.4	0.0	1.2
Birgiolas2020 TC2	3.8	-0.9	-1.0	-1.5	-1.4	-0.7	0.0	-2.0	-1.0	-0.1	-0.2	0.7	0.0	-0.5	-0.2	0.0	1.4
Birgiolas2020 TC1	3.8	-0.7	-1.0	-1.6	0.2	-1.0	0.4	-2.1	0.0	1.1	0.5	0.8	0.2	-0.7	0.4	0.0	1.5

Table 8: Tufted Cell Model Electrophysiology Validation Results. See description in Table 7.

Granule Cell Model Validation Results

Granule Cell Model	RMSE	AfterDepolarizationDepth	AfterDepolarizationTime	CellCapacitance	FISlope	InputResistance	MembraneTimeConstant	ReboundSpiking	RestingVoltage	Rheobase	SagVoltage	SpikeAccommodation	SpikeAmplitude	SpikeHalfWidth	SpikeThreshold
Birgiolas2020 GC1	3.44	0.00	-1.55	-0.48	-1.55	0.25	0.58	0.00	-0.15	0.50	2.09	0.00	-0.08	1.32	0.19
Birgiolas2020 GC5	3.71	0.02	-1.62	-0.31	-0.67	0.28	0.13	0.00	0.22	0.70	2.98	0.00	0.77	0.66	-0.21
Birgiolas2020 GC3	3.87	0.00	-0.46	-0.06	-0.30	-0.58	-0.17	0.00	2.05	0.72	2.96	0.00	0.47	0.66	0.46
Birgiolas2020 GC2	3.94	0.00	-1.56	-0.57	-0.97	-0.23	-0.02	0.00	0.24	0.65	2.95	0.46	0.81	1.32	0.01
Birgiolas2020 GC4	3.97	0.00	-1.65	-0.41	-1.67	0.01	0.36	0.00	0.30	0.64	2.96	0.35	0.35	0.66	0.08
Saghatelyan2005	8.44	2.73	-1.70	-1.95	-2.55	0.62	-0.25	0.00	2.84	1.94	2.95	0.00	-2.69	3.95	2.60
LiCleland2013	9.19	2.07	-1.78	-3.06	-1.48	3.24	-0.33	0.00	2.01	-1.13	-0.66	-6.00	1.45	3.29	0.22
Migliore2008	11.70	5.65	-1.65	-2.03	-1.55	0.65	-0.33	0.00	3.19	-0.24	2.95	-6.00	0.27	6.00	2.09
MiglioreMcTavish2013	11.70	5.65	-1.65	-2.03	-1.55	0.65	-0.33	0.00	3.19	-0.24	2.95	-6.00	0.27	6.00	2.09
McTavish2012	11.82	5.90	-1.68	-2.30	-1.55	1.51	-0.10	0.00	3.20	-0.60	2.24	-6.00	0.37	6.00	2.07
Short2016	11.82	5.90	-1.68	-2.30	-1.55	1.51	-0.10	0.00	3.20	-0.60	2.24	-6.00	0.37	6.00	2.07
Migliore2014	11.93	5.80	-1.69	-2.42	-1.58	1.49	-0.25	0.00	3.20	-0.62	2.95	-6.00	0.58	6.00	1.86
Migliore2015	11.97	5.90	-1.68	-2.30	-1.55	1.51	-0.10	0.00	3.20	-0.60	2.95	-6.00	0.37	6.00	2.07
Yu2012	11.97	5.90	-1.68	-2.30	-1.55	1.51	-0.10	0.00	3.20	-0.60	2.95	-6.00	0.37	6.00	2.07
Davison2003	12.31	1.90	-1.68	2.72	-2.27	1.61	6.00	0.00	3.56	-1.66	2.95	-5.74	0.63	6.00	-0.70
KaplanLansner2014	12.76	1.81	-1.70	3.89	-2.30	1.64	6.00	0.00	3.57	-1.66	2.95	-5.99	0.84	6.00	-0.96

Table 9: Granule Cell Model Electrophysiology Validation Results. See description in Table 7.

Mitral Cell Model Morphology Validation Results

	RMSE	NumberofStems	BasalDendriteNumberofBifurcations	BasalDendriteNumberofBranches	BasalDendriteOverallWidth	BasalDendriteOverallHeight	BasalDendriteOverallDepth	BasalDendriteAverageDiameter	BasalDendriteTotalLength	BasalDendriteTotalSurface	BasalDendriteTotalVolume	BasalDendriteMaxEuclideanDistance	BasalDendriteMaxPathDistance	BasalDendriteMaxBranchOrder	BasalDendriteAverageContraction	BasalDendritePartitionAsymmetry	BasalDendriteAverageRallsRatio	BasalDendriteAverageBifurcationAngleLocal	BasalDendriteAverageBifurcationAngleRemote	BasalDendriteFractalDimension	ApicalDendriteNumberofBifurcations	ApicalDendriteNumberofBranches	ApicalDendriteOverallWidth	ApicalDendriteOverallHeight	ApicalDendriteOverallDepth	ApicalDendriteAverageDiameter	ApicalDendriteTotalLength	ApicalDendriteTotalSurface	ApicalDendriteTotalVolume	ApicalDendriteMaxEuclideanDistance	ApicalDendriteMaxPathDistance	ApicalDendriteMaxBranchOrder	ApicalDendriteAverageContraction	ApicalDendritePartitionAsymmetry	ApicalDendriteAverageRallsRatio	ApicalDendriteAverageBifurcationAngleLocal	ApicalDendriteAverageBifurcationAngleRemote	ApicalDendriteFractalDimension
Oconnor2012 MC4	8.0	-0.9	-0.3	-0.3	0.3	-1.6	-1.2	-0.2	-1.0	-1.7	-1.6	-1.6	-1.5	0.1	0.0	1.2	1.8	-1.8	-0.7	2.1	-0.5	-0.2	-0.9	2.1	-1.3	-0.1	0.4	-0.3	-2.6	0.7	1.5	0.6	0.2	1.7	0.5	-3.9	0.4	0.0
Oconnor2012 MC5	8.1	0.9	0.5	1.0	-1.0	0.1	-1.3	0.7	-0.2	-0.6	-0.5	-0.6	-1.1	1.0	-0.3	1.0	1.3	-2.1	1.0	1.4	0.2	0.5	3.2	-1.6	-1.8	-0.1	-0.1	0.5	-0.7	3.5	1.4	-0.8	0.8	-0.1	2.0	-3.2	-1.2	0.0
Oconnor2012 MC6	8.3	-0.9	-0.6	-0.7	-0.7	-0.7	-1.7	0.6	-1.2	-1.8	-1.6	-0.9	-1.1	0.1	1.0	0.4	1.2	-3.0	0.5	0.8	-0.8	-0.6	1.5	0.8	-2.1	0.1	-0.5	-0.6	-2.2	1.8	0.5	-0.1	1.0	1.2	0.8	-4.5	-1.2	-0.2
Oconnor2012 MC3	8.4	-1.5	-0.6	-0.8	1.3	-1.7	-1.6	0.3	-1.2	-1.8	-1.6	0.1	0.5	0.6	1.0	-0.3	2.0	-1.9	0.6	0.7	0.2	0.4	-1.2	3.4	-2.2	0.0	0.8	1.0	-0.5	2.4	1.3	1.7	1.0	1.0	1.2	-3.1	-0.1	-0.2
Birgiolas2020 MC1	9.8	-0.3	-0.6	-0.7	1.5	0.4	-0.3	1.7	-0.1	-0.1	0.4	0.3	0.2	0.1	1.9	-1.6	2.9	-3.5	0.3	-0.6	-0.5	-0.2	-1.3	-1.1	1.6	0.4	0.6	1.5	1.8	-0.3	-0.6	-0.1	0.9	-0.2	3.8	-5.9	0.0	-0.2
Birgiolas2020 MC2	10.7	0.9	0.3	0.6	1.5	-0.3	-0.7	0.4	0.3	-0.4	-0.4	0.2	0.8	0.6	2.1	0.2	2.9	-3.5	0.1	-0.8	-1.5	-1.1	-1.7	-1.8	2.6	0.0	-1.6	-1.5	-2.9	0.2	-0.6	-1.9	0.7	-0.5	3.8	-5.9	0.7	-0.1
Birgiolas2020 MC4	11.0	-0.3	0.8	1.3	3.0	1.1	-0.7	0.9	1.9	1.8	2.1	1.0	1.1	1.5	2.2	0.6	2.8	-2.8	-0.1	-0.8	-1.3	-1.0	-1.9	-1.5	2.9	0.6	-1.7	-0.4	-0.1	0.2	-0.3	-0.8	0.8	0.0	3.8	-5.9	0.1	-0.1
Birgiolas2020 MC5	11.3	-0.9	0.9	1.4	2.2	0.4	-0.6	0.8	1.2	0.9	1.0	0.6	0.3	0.6	2.2	0.5	2.9	-3.5	0.0	-0.9	-1.5	-1.2	-1.8	-1.6	1.9	1.6	-2.1	0.4	2.8	-0.7	-0.7	-1.5	0.5	-2.4	3.8	-5.9	1.1	-0.1
Oconnor2012 MC1	12.1	-0.9	-0.6	-0.8	3.4	-1.6	-1.5	-0.2	-0.6	-1.4	-1.4	0.7	0.7	0.1	0.6	-0.6	1.6	0.9	0.0	0.6	3.9	3.7	-1.1	4.0	-1.7	-0.5	6.0	1.8	-0.8	2.8	1.6	1.3	0.7	0.7	1.8	-3.6	-0.7	-0.1
Birgiolas2020 MC3	12.3	0.3	0.1	0.5	2.0	0.5	-0.4	2.1	1.2	1.9	3.0	0.2	0.2	0.1	2.1	0.0	2.9	-3.5	0.6	-1.0	0.0	0.2	-1.7	-1.4	1.7	0.8	0.3	2.6	6.0	-0.6	-0.8	0.3	0.9	0.5	3.8	-5.9	-0.3	-0.2
Oconnor2012 MC2	13.0	-2.1	-0.8	-1.1	0.1	-2.1	-1.4	-0.1	-1.3	-2.0	-1.8	-1.4	-1.7	0.6	1.4	0.0	1.2	-1.8	1.2	-0.2	5.2	4.7	-0.2	3.1	-2.0	-0.4	6.0	3.6	-0.4	2.7	1.3	1.7	0.9	0.3	1.2	-2.9	-0.7	-0.1
Popovic2005	14.7	-1.5	-1.3	-1.8	1.7	-1.6	-1.5	-0.3	-1.4	-2.1	-1.8	-0.1	-1.0	-0.9	3.6	-1.6	-2.8	-3.5	-2.4	-1.8	1.1	1.2	1.7	6.0	-1.8	-0.1	4.8	3.8	1.7	6.0	3.9	0.3	1.4	0.6	-0.2	-2.0	-0.7	-0.4
Saghatelyan2005	15.3	-1.5	-1.1	-1.7	-1.4	-1.0	4.5	3.5	-1.2	-1.4	-0.8	0.2	-0.7	-0.9	3.6	-1.6	2.9	-1.4	0.1	-1.8	-2.1	-1.6	-2.3	4.2	-2.3	0.0	-1.5	-0.4	-0.9	3.9	1.4	-2.9	1.4	-3.1	-5.7	-5.9	-4.0	-0.4
LiCleland2013	15.8	-1.5	-1.3	-1.9	-1.4	-1.0	-1.9	6.0	-1.6	-1.8	-0.7	-0.7	-1.5	-1.4	3.6	-1.6	-2.8	-3.5	-2.4	-1.8	-2.1	-1.6	-2.3	3.4	-2.3	1.5	-1.9	0.5	1.0	2.0	0.5	-2.9	1.4	-3.1	-5.7	-5.9	-4.0	-0.4
Migliore2007	16.0	-1.5	-1.1	-1.7	0.3	-1.2	-1.9	3.5	-1.4	-1.7	-1.1	-0.8	-1.6	-0.9	3.6	-1.6	2.9	-1.4	0.1	-1.8	-2.1	-1.6	4.7	2.9	-2.3	-0.2	-0.7	-0.5	-1.4	6.0	3.0	-2.9	1.4	-3.1	-5.7	-5.9	-4.0	-0.4
Chen2002	16.2	-1.5	-1.3	-1.8	-1.4	-1.4	2.9	6.0	-1.4	-1.2	0.4	-0.8	-1.6	-0.9	3.6	-1.6	-2.8	-3.5	-2.4	-1.8	-2.0	-1.5	-2.3	6.0	3.3	1.1	1.5	3.1	1.8	6.0	3.6	-2.6	1.4	-3.1	-1.7	-2.8	-1.3	-0.4
Migliore2015	16.3	-1.5	-0.2	-0.4	3.9	0.5	3.9	5.1	0.6	3.0	6.0	1.1	1.4	1.5	2.8	0.6	2.8	-0.9	1.4	-1.3	-1.8	-1.3	1.0	0.1	6.0	1.5	-0.2	4.2	6.0	4.1	2.6	-1.9	1.1	1.3	0.9	1.8	1.5	-0.3
Shen1999	16.3	-0.9	-1.1	-1.6	0.5	-1.6	-1.9	6.0	-1.4	-1.2	0.5	-0.8	-1.7	-0.9	3.6	-1.6	2.9	-1.4	0.1	-1.8	-1.9	-1.4	3.1	6.0	-2.3	0.8	2.2	5.0	4.7	6.0	4.2	-2.2	1.4	0.2	-0.9	-2.8	-2.1	-0.4
Migliore2008	16.4	-1.5	-1.3	-1.8	0.2	-1.2	-1.9	3.5	-1.4	-1.7	-1.1	-0.8	-1.7	-0.9	3.6	-1.6	-2.8	-3.5	-2.4	-1.8	-2.1	-1.6	4.8	2.1	-2.3	-0.5	-0.7	-0.5	-1.4	6.0	2.9	-2.9	1.4	-3.1	-5.7	-5.9	-4.0	-0.4
Migliore2014	16.9	0.3	0.8	1.3	3.8	1.2	3.5	3.9	3.0	6.0	6.0	2.6	3.6	0.6	3.0	0.7	3.4	-1.8	-0.4	-1.4	-1.8	-1.3	0.6	0.9	5.3	1.5	-0.4	3.7	6.0	3.7	2.3	-1.9	1.0	1.3	0.9	1.0	0.6	-0.3
MiglioreMcTavish2013	17.2	-1.5	-1.1	-1.7	-1.4	-0.4	6.0	3.5	-1.0	-1.0	-0.3	1.6	0.7	-0.9	3.6	-1.6	2.9	-1.4	0.1	-1.8	-2.1	-1.6	-2.3	6.0	-2.3	-0.5	-0.7	-0.5	-1.4	6.0	2.9	-2.9	1.4	-3.1	-5.7	-5.9	-4.0	-0.4
Djurisic2008	17.5	-0.9	-1.1	-1.5	1.5	-2.1	-1.3	1.0	-1.4	-2.0	-1.7	-0.5	-0.9	-0.9	1.2	-1.6	2.1	0.9	1.2	0.2	-2.1	-1.6	-2.3	-2.0	-2.3	-1.1	-4.0	-3.7	-4.8	-4.4	-3.8	-2.9	-4.9	-3.1	-5.7	-5.9	-4.0	-6.0
Migliore2005GJs	17.6	-1.5	-1.3	-1.8	-1.4	-2.3	-0.9	3.5	-1.7	-2.3	-1.9	-2.7	-3.5	-0.9	3.6	-1.6	-2.8	-3.5	-2.4	-1.8	-2.1	-1.6	-2.3	6.0	-2.3	-0.5	-0.7	-0.5	-1.4	6.0	3.0	-2.9	1.4	-3.1	-5.7	-5.9	-4.0	-0.4
McTavish2012	19.2	-1.5	-1.1	-1.7	-1.4	3.1	-1.9	3.5	-1.0	-1.0	-0.3	1.6	0.9	-0.9	3.6	-1.6	2.9	4.9	6.0	-6.0	-2.1	-1.6	4.9	-2.0	-2.3	0.6	-1.2	-0.2	-1.0	4.7	2.0	-2.9	1.4	-3.1	-5.7	-5.9	-4.0	-6.0
Short2016	19.2	-1.5	-1.1	-1.7	-1.4	3.1	-1.9	3.5	-1.0	-1.0	-0.3	1.6	0.9	-0.9	3.6	-1.6	2.9	4.9	6.0	-6.0	-2.1	-1.6	4.9	-2.0	-2.3	0.6	-1.2	-0.2	-1.0	4.7	2.0	-2.9	1.4	-3.1	-5.7	-5.9	-4.0	-6.0
Yu2012	20.0	-1.5	-1.1	-1.7	-1.4	3.1	-1.9	3.5	-1.0	-1.0	-0.3	1.6	0.9	-0.9	3.6	-1.6	2.9	4.9	6.0	-6.0	-2.1	-1.6	6.0	-2.0	-2.3	0.5	-0.7	-0.4	-1.2	6.0	3.0	-2.9	1.4	-3.1	-5.7	-5.9	-4.0	-6.0
RubinCleland2006	20.1	-2.1	-1.3	-1.9	-1.4	-1.9	-1.9	6.0	-1.7	3.6	6.0	-2.2	-3.1	-1.4	3.6	-1.6	-2.8	-3.5	-2.4	-1.8	-2.1	-1.6	-2.3	1.0	-2.3	6.0	-2.6	6.0	6.0	-0.9	-0.5	-2.9	1.4	-3.1	-5.7	-5.9	-4.0	-0.4
Davison2000	20.1	-2.1	-1.3	-1.9	-1.4	-1.9	-1.9	6.0	-1.7	3.6	6.0	-2.2	-3.1	-1.4	3.6	-1.6	-2.8	-3.5	-2.4	-1.8	-2.1	-1.6	-2.3	1.0	-2.3	6.0	-2.6	6.0	6.0	-0.9	-0.5	-2.9	1.4	-3.1	-5.7	-5.9	-4.0	-0.4
KaplanLansner2014	20.1	-2.1	-1.3	-1.9	-1.4	-1.9	-1.9	6.0	-1.7	3.6	6.0	-2.2	-3.1	-1.4	3.6	-1.6	-2.8	-3.5	-2.4	-1.8	-2.1	-1.6	-2.3	1.0	-2.3	6.0	-2.6	6.0	6.0	-0.9	-0.5	-2.9	1.4	-3.1	-5.7	-5.9	-4.0	-0.4
David2008	20.6	-2.1	-1.3	-1.9	-1.4	0.4	-1.9	6.0	-1.4	3.6	6.0	2.1	1.2	-1.4	3.6	-1.6	-2.8	-3.5	-2.4	-1.8	-2.1	-1.6	-2.3	-2.0	-2.3	-1.1	-4.0	-3.7	-4.8	-4.4	-3.8	-2.9	-4.9	-3.1	-5.7	-5.9	-4.0	-6.0
BhallaBower1993	22.5	-1.5	1.3	1.7	6.0	-1.2	6.0	3.8	3.3	6.0	6.0	5.6	6.0	2.5	3.4	1.8	0.9	-1.7	1.4	-1.7	3.1	3.0	-0.2	6.0	0.6	-0.1	6.0	6.0	6.0	6.0	5.3	0.3	1.2	1.5	0.4	-0.4	0.8	0.2

Table 10: Mitral Cell Morphology Validation Results. Models in the left column are sorted by morphology property RMSE. All other values are morphology property Z-scores for each model. Z-scores were clamped to ±6 standard deviations. O'Connor2012, Birgiolas2020, and Popovic2005 models used reconstructed cell morphologies.

Tufted Cell Model Morphology Validation Results

	RMSE	NumberofStems	BasalDendriteNumberofBifurcations	BasalDendriteNumberofBranches	BasalDendriteOverallWidth	BasalDendriteOverallHeight	BasalDendriteOverallDepth	BasalDendriteAverageDiameter	BasalDendriteTotalLength	BasalDendriteTotalSurface	BasalDendriteTotalVolume	BasalDendriteMaxEuclideanDistance	BasalDendriteMaxPathDistance	BasalDendriteMaxBranchOrder	BasalDendriteAverageContraction	BasalDendritePartitionAsymmetry	BasalDendriteAverageRallsRatio	BasalDendriteAverageBifurcationAngleLocal	BasalDendriteAverageBifurcationAngleRemote	BasalDendriteFractalDimension	ApicalDendriteNumberofBifurcations	ApicalDendriteNumberofBranches	ApicalDendriteOverallWidth	ApicalDendriteOverallHeight	ApicalDendriteOverallDepth	ApicalDendriteAverageDiameter	ApicalDendriteTotalLength	ApicalDendriteTotalSurface	ApicalDendriteTotalVolume	ApicalDendriteMaxEuclideanDistance	ApicalDendriteMaxPathDistance	ApicalDendriteMaxBranchOrder	ApicalDendriteAverageContraction	ApicalDendritePartitionAsymmetry	ApicalDendriteAverageRallsRatio	ApicalDendriteAverageBifurcationAngleLocal	ApicalDendriteAverageBifurcationAngleRemote	ApicalDendriteFractalDimension
Birgiolas2020 TC4	**9.7**	-0.6	0.4	0.2	0.8	0.0	1.1	-1.0	1.0	-0.5	0.1	-0.4	-0.2	0.2	0.3	-0.3	2.6	-2.5	0.4	0.1	1.8	1.3	0.0	-1.7	-0.1	-1.5	1.5	0.1	-0.5	-0.4	-0.6	0.3	1.4	0.0	5.0	-6.0	-0.7	-0.7
Birgiolas2020 TC3	**10.3**	-0.1	-0.6	-0.9	-0.6	-0.7	0.7	0.4	-0.7	-1.8	-0.8	-0.9	-1.5	-0.3	0.8	0.3	2.6	-2.5	0.7	0.1	-0.5	-1.1	-0.3	-1.4	-0.8	-0.5	-1.1	-0.8	-0.9	-1.6	-2.2	-1.0	1.3	-0.5	5.0	-6.0	-1.3	-0.9
Birgiolas2020 TC2	**10.8**	0.4	-0.3	-0.4	1.6	1.3	0.9	-1.8	1.1	-0.9	-0.5	1.9	1.3	0.7	0.4	2.2	2.6	-2.5	0.0	0.0	0.2	-0.4	-1.0	-1.4	0.1	-1.7	0.2	-0.6	-0.8	-0.7	-1.4	-0.5	1.9	0.1	5.0	-6.0	-2.4	-1.7
Birgiolas2020 TC5	**10.8**	-1.0	0.7	0.5	0.3	1.6	2.7	-2.6	1.3	-1.3	-1.1	1.2	0.7	0.2	0.8	0.7	2.6	-2.5	-0.1	-0.1	-0.6	-1.2	1.8	-1.4	0.3	-1.2	-1.2	-1.0	-1.0	0.8	-0.1	-1.2	0.2	-1.8	5.0	-6.0	0.2	-0.4
Birgiolas2020 TC1	**11.0**	-1.0	0.0	-0.5	1.8	-1.8	1.4	-2.6	-0.4	-2.1	-1.3	0.2	-0.8	0.7	1.0	0.9	2.6	-2.5	-1.3	-0.1	0.5	-0.1	-0.6	-0.9	-0.1	-2.2	0.5	-0.9	-1.1	-1.8	-1.9	-0.5	1.2	-1.4	5.0	-6.0	-0.6	-0.8

Table 11: Tufted Cell Model Morphology Validation Results. See Table 10 for description.

Granule Cell Model Morphology Validation Results

	RMSE	NumberofStems	BasalDendriteNumberofBifurcations	BasalDendriteNumberofBranches	BasalDendriteOverallWidth	BasalDendriteOverallHeight	BasalDendriteOverallDepth	BasalDendriteAverageDiameter	BasalDendriteTotalLength	BasalDendriteMaxEuclideanDistance	BasalDendriteMaxPathDistance	BasalDendriteMaxBranchOrder	BasalDendriteAverageContraction	BasalDendritePartitionAsymmetry	BasalDendriteAverageRallsRatio	BasalDendriteAverageBifurcationAngleLocal	BasalDendriteAverageBifurcationAngleRemote	BasalDendriteFractalDimension	ApicalDendriteNumberofBifurcations	ApicalDendriteNumberofBranches	ApicalDendriteOverallWidth	ApicalDendriteOverallHeight	ApicalDendriteOverallDepth	ApicalDendriteAverageDiameter	ApicalDendriteTotalLength	ApicalDendriteMaxEuclideanDistance	ApicalDendriteMaxPathDistance	ApicalDendriteMaxBranchOrder	ApicalDendriteAverageContraction	ApicalDendritePartitionAsymmetry	ApicalDendriteAverageRallsRatio	ApicalDendriteAverageBifurcationAngleLocal	ApicalDendriteAverageBifurcationAngleRemote	ApicalDendriteFractalDimension
Birgiolas2020 GC5	5.5	-1.4	-0.6	-1.4	-0.5	-0.4	-0.8	-0.4	-1.1	-0.5	-0.5	-0.3	-0.5	-0.1	-0.2	-0.3	-0.3	-0.7	0.7	0.6	0.1	0.5	1.2	-0.5	0.7	0.5	0.8	0.4	-1.2	1.3	0.2	-3.8	0.5	0.4
Birgiolas2020 GC1	5.7	-1.4	-0.6	-1.4	-0.5	-0.4	-0.8	-0.4	-1.1	-0.5	-0.5	-0.3	-0.5	-0.1	-0.2	-0.3	-0.3	-0.7	1.3	1.0	0.7	0.6	0.9	-2.0	1.2	0.6	0.5	-0.2	-0.3	-0.3	0.2	-3.8	-0.3	0.0
Birgiolas2020 GC2	6.2	-1.4	-0.6	-1.4	-0.5	-0.4	-0.8	-0.4	-1.1	-0.5	-0.5	-0.3	-0.5	-0.1	-0.2	-0.3	-0.3	-0.7	0.7	0.6	2.5	-1.1	1.0	-2.2	0.5	-0.8	-0.7	-0.2	-0.5	-0.6	0.2	-3.8	0.5	-0.2
Migliore2008	6.3	-1.4	-0.6	-1.4	-0.5	-0.4	-0.8	-0.4	-1.1	-0.5	-0.5	-0.3	-0.5	-0.1	-0.2	-0.3	-0.3	-0.7	1.8	1.5	-1.5	-0.9	1.1	-2.8	0.3	-0.9	-0.1	0.4	1.0	0.3	1.4	1.6	2.7	-0.6
Migliore2007	6.5	-1.4	-0.6	-1.4	-0.5	-0.4	-0.8	-0.4	-1.1	-0.5	-0.5	-0.3	-0.5	-0.1	-0.2	-0.3	-0.3	-0.7	-0.4	-0.3	-1.5	-0.8	1.1	-2.7	-0.3	-0.9	-0.6	-0.9	-0.4	0.2	-2.2	-3.8	1.0	-0.6
Birgiolas2020 GC4	6.6	-1.4	-0.6	-1.4	-0.5	-0.4	-0.8	-0.4	-1.1	-0.5	-0.5	-0.3	-0.5	-0.1	-0.2	-0.3	-0.3	-0.7	0.7	0.6	1.0	0.3	1.0	-3.9	0.8	0.3	0.3	0.4	-0.4	1.3	0.2	-3.8	0.2	0.1
Birgiolas2020 GC3	6.8	-1.4	-0.6	-1.4	-0.5	-0.4	-0.8	-0.4	-1.1	-0.5	-0.5	-0.3	-0.5	-0.1	-0.2	-0.3	-0.3	-0.7	1.3	1.0	1.4	1.4	2.3	-2.5	1.4	1.5	1.4	0.4	-0.1	0.0	0.2	-3.7	0.7	0.1
Saghatelyan2005	9.0	-1.4	-0.6	-1.4	-0.5	-0.4	-0.8	-0.4	-1.1	-0.5	-0.5	-0.3	-0.5	-0.1	-0.2	-0.3	-0.3	-0.7	-0.9	-0.8	-1.5	3.2	-0.7	-0.3	0.2	3.2	2.3	-1.5	-0.4	-2.1	-4.7	-3.8	-0.1	-0.6
LiCleland2013	9.5	-1.4	-0.6	-1.4	-0.5	-0.4	-0.8	-0.4	-1.1	-0.5	-0.5	-0.3	-0.5	-0.1	-0.2	-0.3	-0.3	-0.7	-1.5	-1.2	-1.5	-0.8	-0.8	-0.1	-0.7	-1.0	-1.3	-2.1	1.9	-2.1	-6.0	-3.8	-2.9	-0.6
Yu2012	10.1	-1.4	-0.6	-1.4	-0.5	-0.4	-0.8	-0.4	-1.1	-0.5	-0.5	-0.3	-0.5	-0.1	-0.2	-0.3	-0.3	-0.7	-1.5	-1.2	-1.5	0.1	-0.8	-3.0	-0.4	-0.2	0.0	-2.1	-3.0	-2.1	-6.0	-3.8	-2.9	1.1
McTavish2012	11.3	-0.6	-0.6	-1.4	-0.5	-0.4	-0.8	-0.4	-1.1	-0.5	-0.5	-0.3	-0.5	-0.1	-0.2	-0.3	-0.3	-0.7	-1.5	-1.0	-1.5	0.1	-0.8	-2.9	-0.1	-0.2	-0.6	-2.1	1.9	-2.1	-6.0	-3.8	-2.9	-6.0
Migliore2015	11.3	-0.6	-0.6	-1.4	-0.5	-0.4	-0.8	-0.4	-1.1	-0.5	-0.5	-0.3	-0.5	-0.1	-0.2	-0.3	-0.3	-0.7	-1.5	-1.0	-1.5	0.1	-0.8	-2.9	-0.1	-0.2	-0.6	-2.1	1.9	-2.1	-6.0	-3.8	-2.9	-6.0
Short2016	11.3	-0.6	-0.6	-1.4	-0.5	-0.4	-0.8	-0.4	-1.1	-0.5	-0.5	-0.3	-0.5	-0.1	-0.2	-0.3	-0.3	-0.7	-1.5	-1.0	-1.5	0.1	-0.8	-2.9	-0.1	-0.2	-0.6	-2.1	1.9	-2.1	-6.0	-3.8	-2.9	-6.0
Migliore2014	11.4	-0.6	-0.6	-1.4	-0.5	-0.4	-0.8	-0.4	-1.1	-0.5	-0.5	-0.3	-0.5	-0.1	-0.2	-0.3	-0.3	-0.7	-1.5	-1.0	-1.5	0.9	-0.8	-2.9	-0.2	0.7	0.1	-2.1	1.9	-2.1	-6.0	-3.8	-2.9	-6.0
Davison2003	14.8	-0.6	-0.6	-0.8	-0.5	4.3	-0.8	6.0	0.4	3.7	3.4	-0.3	2.5	-0.1	-0.2	-0.3	-0.3	1.5	-1.5	-1.2	-1.5	-2.1	-0.8	6.0	-0.9	-2.3	-1.9	-2.1	1.9	-2.1	-6.0	-3.8	-2.9	-0.6
KaplanLansner2014	14.8	-0.6	-0.6	-0.8	-0.5	4.3	-0.8	6.0	1.1	3.7	3.4	-0.3	2.5	-0.1	-0.2	-0.3	-0.3	1.5	-1.5	-1.2	-1.5	-2.1	-0.8	6.0	-0.9	-2.3	-1.9	-2.1	1.9	-2.1	-6.0	-3.8	-2.9	-0.6
MiglioreMcTavish2013	23.7	-1.4	6.0	6.0	-0.5	6.0	6.0	0.5	6.0	6.0	6.0	5.6	2.5	6.0	3.3	3.0	3.6	1.5	-1.5	-1.4	-1.5	-2.8	-0.8	-5.2	-1.1	-2.9	-3.0	-2.1	-6.0	-2.1	-6.0	-3.8	-2.9	-6.0

Table 12: Granule Cell Model Morphology Validation Results. See Table 10 for description.

2.1.5 Novel Cell Model Development

After evaluating existing models, novel cell models were developed with lower deviation from experimental data. Additionally, multiple models of each cell type were developed to better account for natural heterogeneity found in real cells. The full biophysically realistic models were developed by adding ion channel models to the membranes of representative morphologies and performing automated parameter searches using the electrophysiology RMSE as the cost function.

For each cell type, five reconstructions were randomly selected from a set of cleaned full-cell reconstructions. Granule cell reconstructions were from Sailor et al. (2016), and mitral and tufted cell reconstructions were from Fukunaga et al. (2012). Using neuTube's "edit SWC" tool, SWC nodes that were closer than 1 μm were merged. Axons, if any, were truncated to 30 μm. NEURON's import SWC function was used to create NEURON sections from the morphologies. NEURON's d_lambda rule with frequency parameter set to 100 Hz was used to discretize the imported sections into compartments ("Using the d_lambda Rule," 2019).

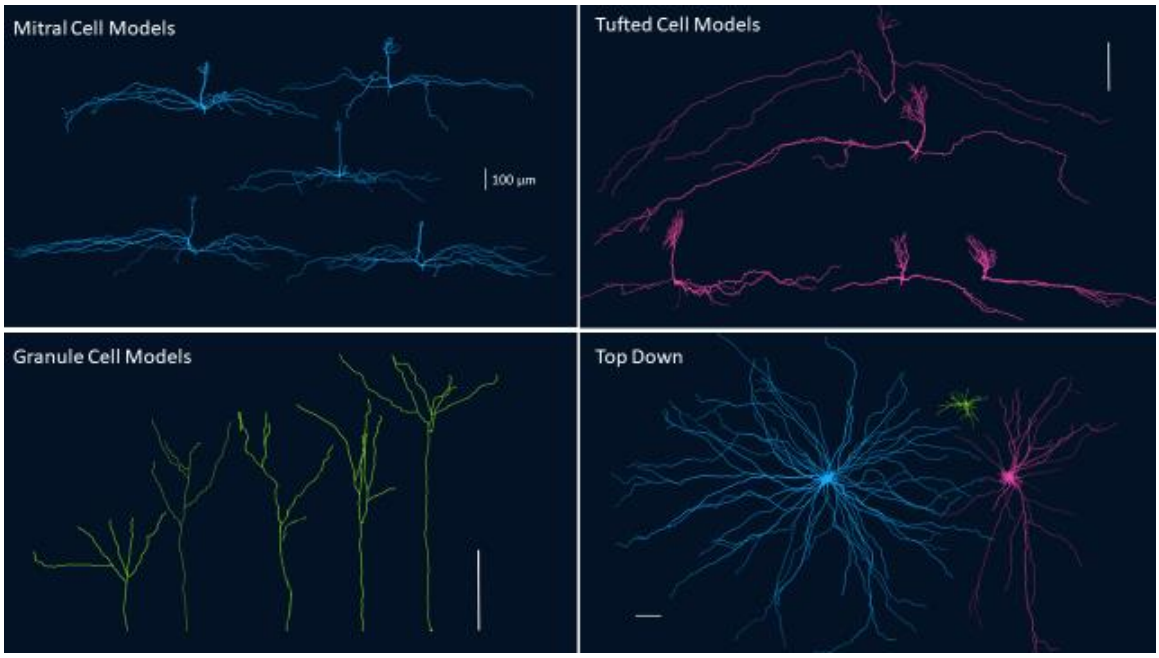

Figure 4: Morphologies of Novel Models of Mitral, Tufted, and Granule Cells

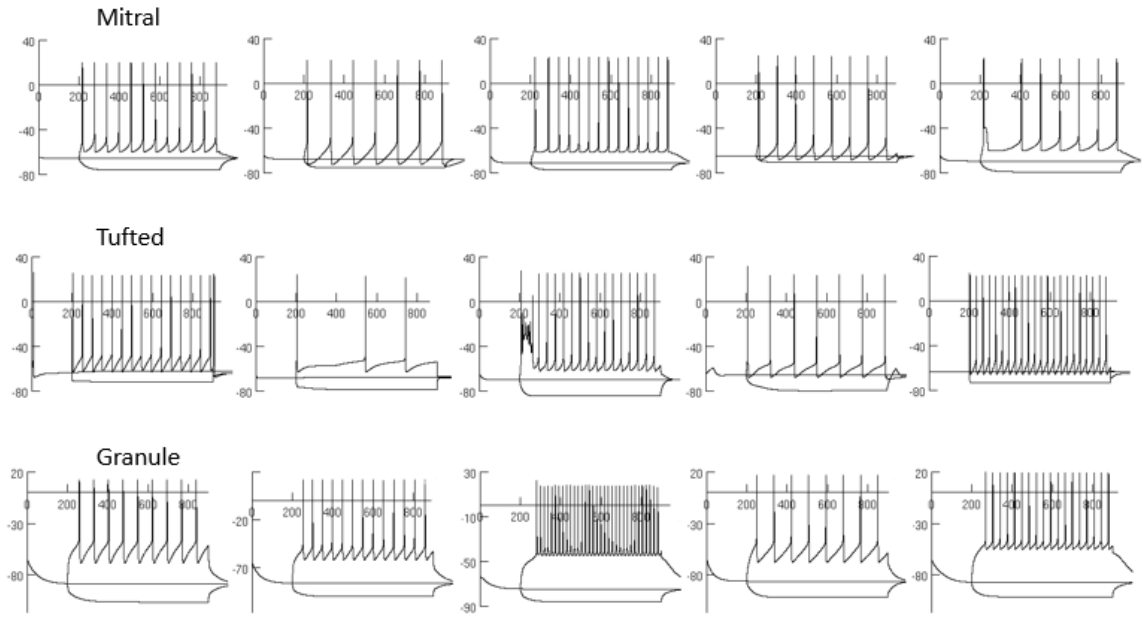

Figure 5: Electrophysiology of Novel Models of Mitral, Tufted, and Granule Cells. Each row contains somatic membrane potential traces of five novel cell models in response to 700 ms square current injections. Mitral and tufted cell models were injected 0.25, -0.1, and 0 nA. Granule cell models were injected 0.06, -0.02, and 0 nA. Simulation temperature was 35 ºC. Y-axis units are mV; X-axis units are ms.

The lateral dendrites of each mitral and tufted cell reconstruction reflect their local olfactory bulb curvature. In order to build a network model and ensure that the

lateral dendrites are confined to their respective locations within the layers regardless of their position in the bulb, the lateral dendrites were planarized by manually rotating the dendritic branches around the branch points. This transformation preserved the surface area (no changes to lengths or radii of the sections). When these base cell models were inserted into a specific location within the bulb, a novel algorithm was used to confine the planarized dendrites to their appropriate portions of the plexiform layer (see "2.3.4 Cell and Dendrite Orientations") resulting in lateral dendrites that reflect the local bulbar curvature.

Similarly, to aid later cell orientation, the apical dendrites were aligned with the Z-axis. In some cases, mitral/tufted cell apical dendrites were rotated "up-right" to be roughly perpendicular to the lateral dendrite plane. From this position, the apical dendrites were aligned towards a nearby glomerulus when placing the cell within the bulb layers.

To perform the surface area conserving rotations, an add-on, BlenderNEURON (Birgiolas, 2018/2019a), was developed for the 3D modeling software Blender (Blender Foundation, 2019). Using Blender and NEURON Python interfaces, the add-on establishes a two-way communication channel, which allows the import of models instantiated in NEURON into Blender. Once in Blender, a variety of complex 3D manipulations can be performed using Blender's built-in functionality. Specifically, BlenderNEURON establishes parent-child object relations between cell model sections, which allows rotations applied to a base branch section to be applied to descendant sections as well (see Figure 6). This functionality was used to planarize mitral/tufted cell lateral dendrites and to rotate cells and align their apical dendrites with the Z-axis. The manipulation does not alter section sizes and preserves cell surface area, which prevents the need to re-fit cell model electrophysiology. Once the 3D manipulations

were finished, BlenderNEURON exported changes to the sections back to NEURON for simulation.

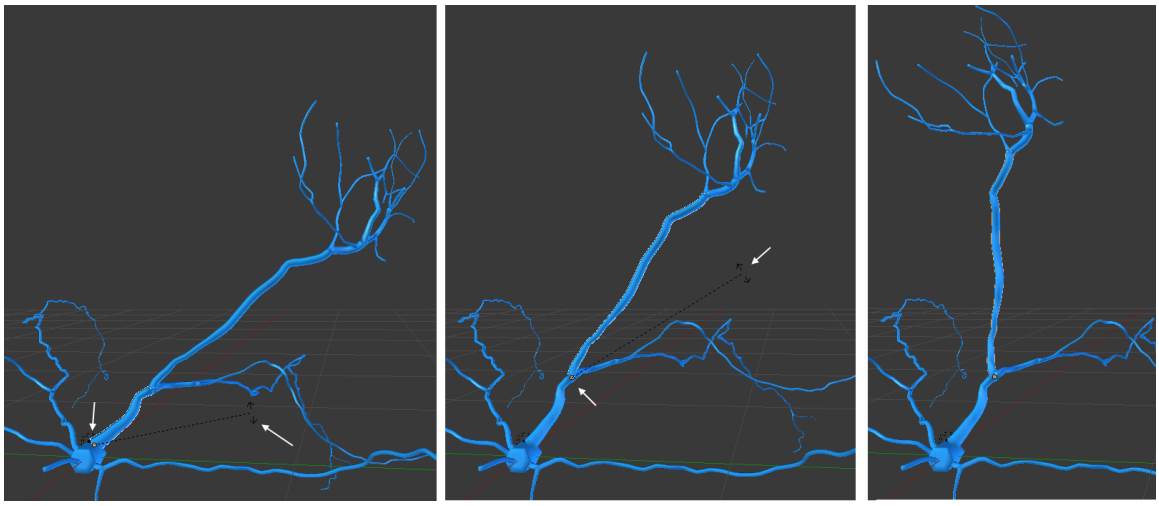

Figure 6: Branch Rotations Using BlenderNEURON. BlenderNEURON add-on imports NEURON sections into Blender. The sections/cells can then be manipulated (e.g. rotated, translated) and exported back to NEURON for simulation.

Once a cell model morphology was in NEURON, ion channel models were added to the cell model membrane. Channel models were taken from previously published models. The channel models included: passive (Hines & Carnevale, 1997), Na, Kd, KA (Short et al., 2016) KM, Kslow, LCa, CaT, Ih (Li & Cleland, 2013) and KCa (O'Connor et al., 2012). A calcium pool model (Li & Cleland, 2013) was also included in compartments with calcium channels. Base 3 temperature correction factor Q10 was added to Kslow, LCa, and CaT channels.

All sections of mitral and tufted cell models contained the passive, Na, K_d, LCa, K_{slow}, K_A, and KCa channels. Mitral and tufted apical dendrite sections contained the CaT and I_h channels. All sections of granule cell models contained the passive, Na, and K_d channels. Granular soma sections had the K_M, K_A, and I_h channels.

Once the channels were added, parameters in Table 13 were allowed to vary freely (within the specified ranges) while a genetic algorithm was used to find

parameter value combinations that minimized each model's overall electrophysiology property RMSE.

	Mitral			**Tufted**			**Granule**		
Parameter	*Loc*	*Range*		*Loc*	*Range*		*Loc*	*Range*	
diam scale	A,B,AX	0.1	5	A,B,AX	0.1	2	A	0.1	3
Length	S	6.58	13.37	S	3.5	11.6	S	0.89	5.04
Ra	All	1	150	All	1	150	All	5	150
cm	All	0.1	2	All	0.1	5	All	0.1	10
ena	All	20	80	All	20	80	All	10	90
ek	All	-100	-50	All	-100	-50	All	-100	-30
e_pas	All	-90	-50	All	-90	-50	All	-100	-50
g_pas	All	0	0.0002	All	0	0.0004	All	0	0.004
sh_Na	All	0	10	All	0	10	All	0	10
gbar_Na	All	0	0.2	All	0	0.1	S	0	5
gbar_Kd	All	0	0.1	All	0	0.2	S	0	5
gbar_KA	All	0	0.02	All	0	0.02	S	0	0.8
gbar_Kslow	All	0	0.002	All	0	0.002			
gbar_KCa	All	0	0.016	All	0	0.016			
gbar_LCa	All	0	0.0005	All	0	0.001			
tau_CaPool	All	1	300	All	1	300			
gbar_CaT	A	0	0.02	A	0	0.02			
eh	A	-40	-10	A	-40	-10	S	-60	-10
gbar_Ih	A	0	0.000006	A	0	0.00006	S	0	0.0002
gbar_KM							S	0	0.13
gbar_Na							A	0	0.4
gbar_Kd							A	0	1.6

Table 13: Parameters and Their Ranges Used for Cell Model Fitting. Parameter column lists the parameters that were varied. Parameters with underscores follow the NEURON convention (param_mechanism). "diam scale" was a scaling factor by which original reconstruction diameters were scaled. Loc columns refer to the cell parts where the parameters were varied (A: apical, B: basal/lateral, AX: axonal, S somatic). Range columns show the allowed low-high value range.

The genetic algorithm used for fitting was implemented using the DEAP package (Fortin, Rainville, Gardner, Parizeau, & Gagné, 2012). Each model was optimized using 30 individuals over 200 generations. The cost function was the electrophysiology property RMSE. The "bounded simulated binary crossover" rule with eta parameter set to 0.1 was used for mating. The "polynomial mutation" rule with eta parameter set to 0.1 and mutation probability set to 0.9 was used for mutations. Elitism was implemented by retaining the top 20% individuals of each generation. 25% of offspring had elite parents, another 25% had random parents, while the remaining offspring

were randomly generated. Each simulation was performed using NEURON's variable step integration method (CVODE) with 0.001 as the absolute tolerance. Parameter sets that resulted in long running (>2.5 minutes) or unstable (integrator errors) simulations were assigned high cost values (e.g. 90, while typical well-behaved model RMSEs were below 20 and completed under 2 minutes).

After optimization, the electrophysiology RMSE values of all 15 novel models were below the RMSE values of all previous models of each cell type (Birgiolas2020 models in Table 7, Table 8, and Table 9). Morphology RMSE values of novel models were below or in the close vicinity of RMSE values of earlier models whose morphologies were based on neuron reconstructions (Table 10, Table 11, and Table 12). These 15 novel models were selected for inclusion in the network model.

2.2 Layer Reconstruction

An anatomical model of the 3D cell layers of mouse olfactory bulb was developed and the reconstructed layers were used to place and orient the cell models within their appropriate locations.

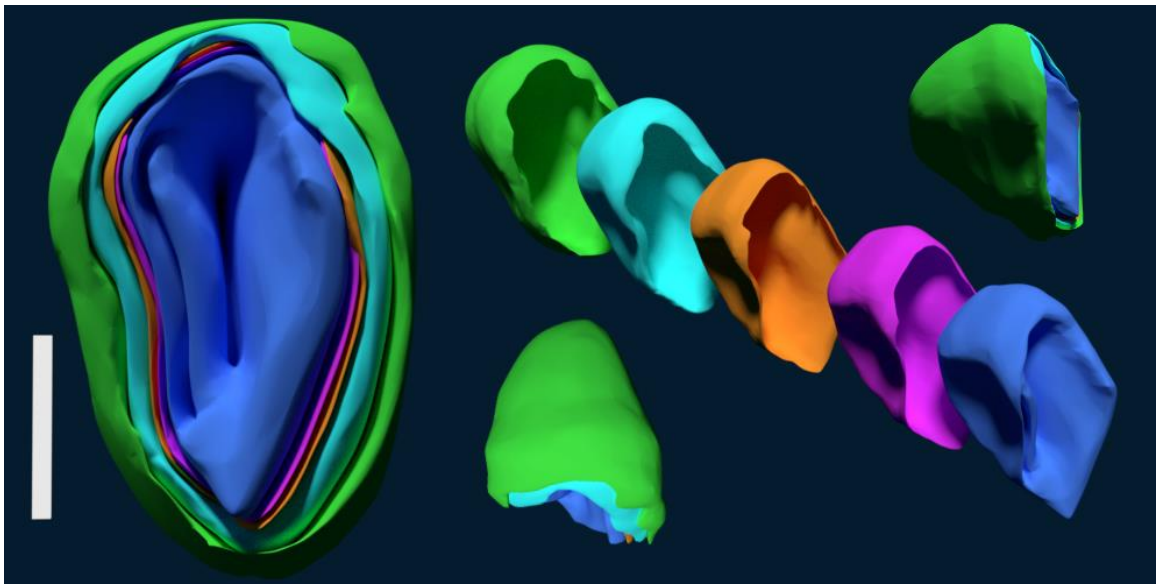

Figure 7: Reconstructed Layers of the Olfactory Bulb. Green: glomerular layer, Aqua: external plexiform layer, Orange: mitral cell layer, Purple: internal plexiform layer, Blue: granule cell layer. Scale bar: 1000 μm. An interactive, downloadable version of the model shown in this figure is available online at: https://skfb.ly/6NpHL.

The Allen Mouse Brain Atlas ("Interactive Atlas Viewer: Atlas Viewer," 2019; Oh et al., 2014) contains labeled adult mouse coronal and sagittal brain slices that include all layers of the olfactory bulb. However, while the sagittal slices contain the entire bulb, they are lower resolution, 200 μm thick, slices. Alternatively, the coronal slices are higher resolution, 100 μm thick, but do not contain the most anterior portion of the bulb. To ensure the model contained the full bulb while preserving the most detail, Blender was used to combine the laminar structures obtained from partial, higher resolution coronal slices with the laminar structure obtained from complete, but lower resolution sagittal slices.

First, labeled 2D coronal and sagittal slice stacks of the bulb were combined into 3D models of each cut direction. Layer outlines contained in 2D slice images were converted to vector format using Inkscape (Bah, 2011) and the resulting SVG files were imported into Blender. Polygons were created between vertices of nearby slices using Blender's "Bridge Edge Loops" or "Make Edge/Face" tools as necessary. The

combined, higher-resolution 3D model of the bulb with the missing anterior portion obtained from coronal slices was fused with the lower-resolution 3D model of the anterior portion of the bulb obtained from the sagittal slices. Fusing of the anterior portion with the rest of the bulb was performed by manually aligning the vertices of the two partial 3D meshes and using Blender's "Merge Vertex" tool. The final 3D model consisted of 3D meshes of glomerular, external plexiform, mitral cell, internal plexiform, and granule cell layers (Figure 7). To reduce the number of polygons and achieve roughly uniform vertex density, layer meshes were simplified by manually sculpting each mesh with Blender's "Dyntopo" tool, which simplifies the vertices under the cursor while maintaining the overall curvature. The layer vertices were saved as Blender files, which were later accessed using Blender's Python API.

2.3 Cell Model Placement within Olfactory Bulb Layers

After the olfactory bulb structural model was constructed, the cell models were placed and oriented within the correct layers of the anatomical model. The locations of the model somas of each cell type were identified based on the layers in which each cell type is found and the cell counts of each type found in the literature. Once the somas were placed within layers, cell apical dendrites were oriented towards nearby glomeruli while lateral dendrites, if any, were confined to appropriate sub-layer regions.

2.3.1 Virtual Slices

A virtual slice paradigm was employed to make to make it possible to build network models at different scales. Common experimental slice preparations as well as arbitrary 3D shapes (called meshes in Blender nomenclature) can be defined as "virtual slices" (see Figure 8). Once defined, the name of the slice object is passed into a script that builds the network model, selecting the glomeruli and cell somas that are

within that slice for inclusion in the network simulation. The virtual slices do not truncate the dendrites that fall outside of the slice boundaries.

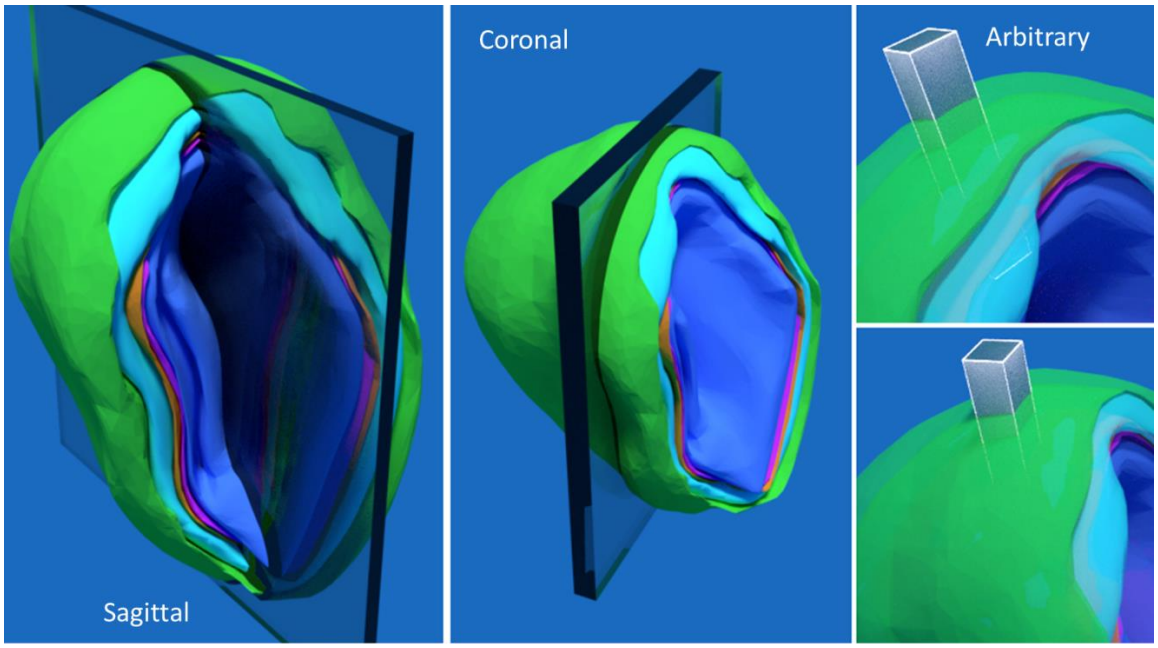

Figure 8: Examples of Virtual Slices. Virtual slices can be defined by arbitrary 3D meshes. The sagittal slice shown is 100 μm thick, the coronal slice is 200 μm thick, while the arbitrary slice defines a column of size 100x100x1000 μm. Glomeruli and cells that are inside a virtual slice are included in the simulation.

2.3.2 Cell and Glomerular Counts

Published literature was surveyed to identify the number of cells of each type in adult mouse olfactory bulb (Table 14). Each reported measurement was treated as a Gaussian distribution parameterized by the mean (μ) and standard deviation (σ) of the reported value, from which n (reported sample size) random values were picked and combined into pools for each cell type. To select a specific number of cells to include in the whole bulb model, a random number was picked from each pool. If a publication did not report the sample size, the standard deviation was assumed to be zero and n to be one. The same method was used to select the number of glomeruli to include in the whole bulb model (also in Table 14).

The selected values are reported in the right column of Table 14. Virtual slices were used to select a subset of the whole bulb. If a virtual slice were defined to be large enough to encompass the full bulb, and thereby include all cells and glomeruli, it would include approximately 800,000 cells.

Experimental (Adult Mouse) and Model Counts of Glomeruli and Cells

	μ ± σ (n)	Source	Full Model
Glomeruli	1,943 ± 171 (10)	Pomeroy et al. (1990)	1,915
	1,810 ± 164 (16)	Royet et al. (1988)	
Mitral Cells	38,355 ± 2,856 (4)	Benson et al. (1984)	39,660
	45,250 ± 0 (1)	Purves el. al. (2004)	
Tufted Cells	95,888 ± 9,784 (2)	Shepherd (1972)	93,564
	76,710 ± 0 (1)	Shepherd et al. (2010)	
	90,500 ± 0 (1)	Purves el. al. (2004)	
Granule Cells	758,313 ± 248,050 (33)	Gheusi et al. (2000)	672,353
	537,064 ± 30,637 (16)	Breton-Provencher et al. (2009)	

Table 14: Experimental and Model Counts of Cells and Glomeruli. Left columns show the summary statistics of cell and glomerular counts reported in experimental literature. The last column shows the maximum number of cells that would be included if the entire bulb was selected for simulation (see section 2.3.2 for details). Virtual slices include subsets of these cells.

2.3.3 Glomerular and Soma Locations

In order to place cells, their soma locations were pre-determined within layers via the use of a space-filling algorithm. Blender comes with built in "particles" functionality that uses a white noise distribution to select random locations of particles within the confines of a 3D mesh (e.g. a layer). These locations can then be used for cell placement. However, a white noise distribution tends to create random regions with high and low densities, which are not realistic in a compact neuropil setting. Blender also has a built-in physics simulation, which can be used to evenly pack soma-like spheres within layers. However, for the granule cell layer, this would require

running a computationally expensive ~800,000-body force-field simulation. A computationally efficient alternative that approximates biological realism is the use of a blue noise distribution (Yuksel, 2015), which results in more even, yet random, distribution of points within a mesh. The algorithm is implemented in a Blender add-on (BorisTheBrave, 2017/2019), which was used to select cell/glomerular locations within glomerular, external plexiform, mitral cell, and granule cell layers. When creating a virtual slice, only soma/glomerular locations that are within the slice mesh are used. The generated cell locations were saved in a Blender file and later accessed via the Blender Python API.

2.3.4 Cell and Dendrite Orientations

Once a virtual slice has been selected and soma and glomerular locations within it identified, cell models were placed and oriented at each location.

Mitral and tufted cells were placed using a similar procedure (see Figure 9). First, a random soma location within the slice was chosen and distance to the closest point in the glomerular layer was computed. The set of five available cell models was filtered to the set of cells whose apical dendrite could extend into the glomerular layer. A cell was randomly picked from this filtered set. If no cell could extend that far, the model with the longest apical dendrite was selected. When selecting a granule cell model, the full granule cell model set was filtered to those models whose apical dendrites could extend within the external plexiform layer. As with mitral/tufted cells, the granule cell model with the longest apical dendrite was selected if no cell could extend into the external plexiform layer.

The selected mitral/tufted cell was placed at the selected soma location and rotated so that its apical dendrite pointed towards the closest glomerulus. The cell soma and the glomerulus formed a vector around which the whole cell was rotated by a random degree. Because the reach of the apical dendrite did not always coincide

with the distance to the closest glomerulus, a nearby glomerulus was identified such that the distance to it was approximately the same as the reach of the apical dendrite. The apical dendrite was then rotated towards the matching glomerulus. Granule cells did not require this step.

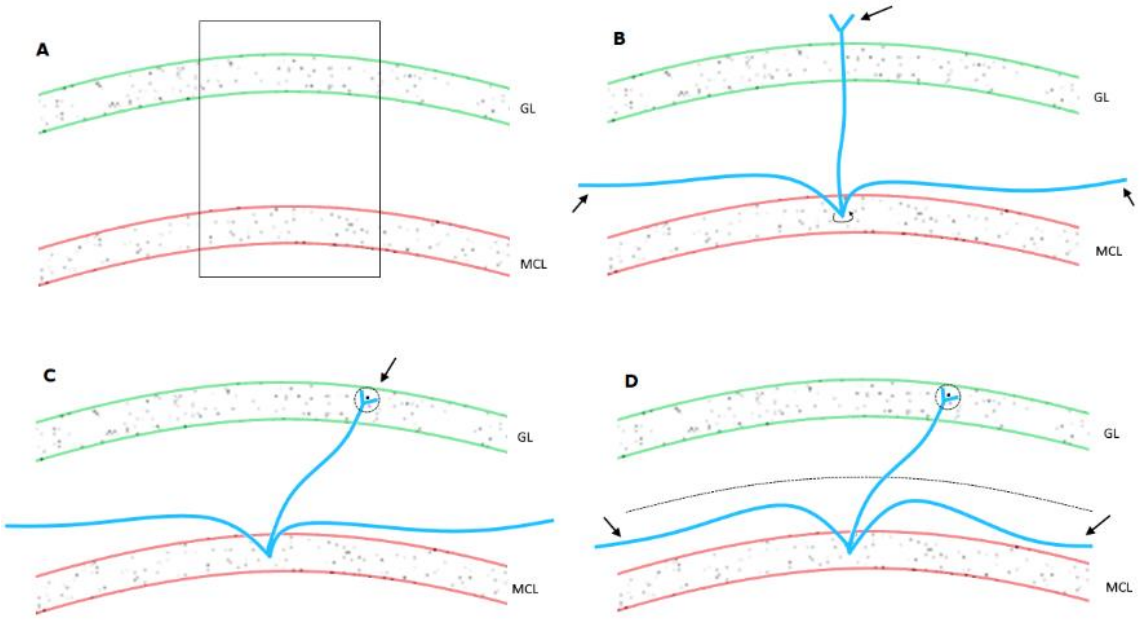

Figure 9: The Process for Placing Mitral Cell Models. A: A virtual slice defines cell model soma and glomerulus locations for inclusion in the slice model. B: A mitral cell model is placed at a random soma location in the mitral cell layer. The whole cell is rotated by a random amount around the apical dendrite. This model's apical dendrite extends beyond the glomerular layer, and the lateral dendrites do not follow the curvature of the bulb layers. C: The apical dendrite is rotated towards a glomerulus whose distance matches the extent of the apical dendrite. D: The lateral dendrites are confined to the lower portion of the external plexiform layer.

Mitral and tufted cell dendrites are confined to approximately deeper and superficial halves of the external plexiform layer, **r**espectively (Fukunaga et al., 2012, 2014; Mori et al., 1983; Nagayama, Igarashi, et al., 2014). In order to make sure the dendrites in this model reflect these distributions, a novel algorithm was developed to confine the dendrites of the cell models within their respective sub-layer regions. The algorithm takes two Blender meshes that define deeper and superficial boundaries for dendrite confinement, low-high fractions that define the confinement portion between

the layers, and a maximum angle by which dendritic branches can be rotated about their branch points. Starting with lateral dendrite sections closest to the soma, the algorithm rotates the section and its descendant sections (as in Figure 6) towards a random position between the two layers. It then repeats the rotations to descendant dendritic sections. At the end of the process, all lateral dendrites become confined to the space between the specified layer boundaries.

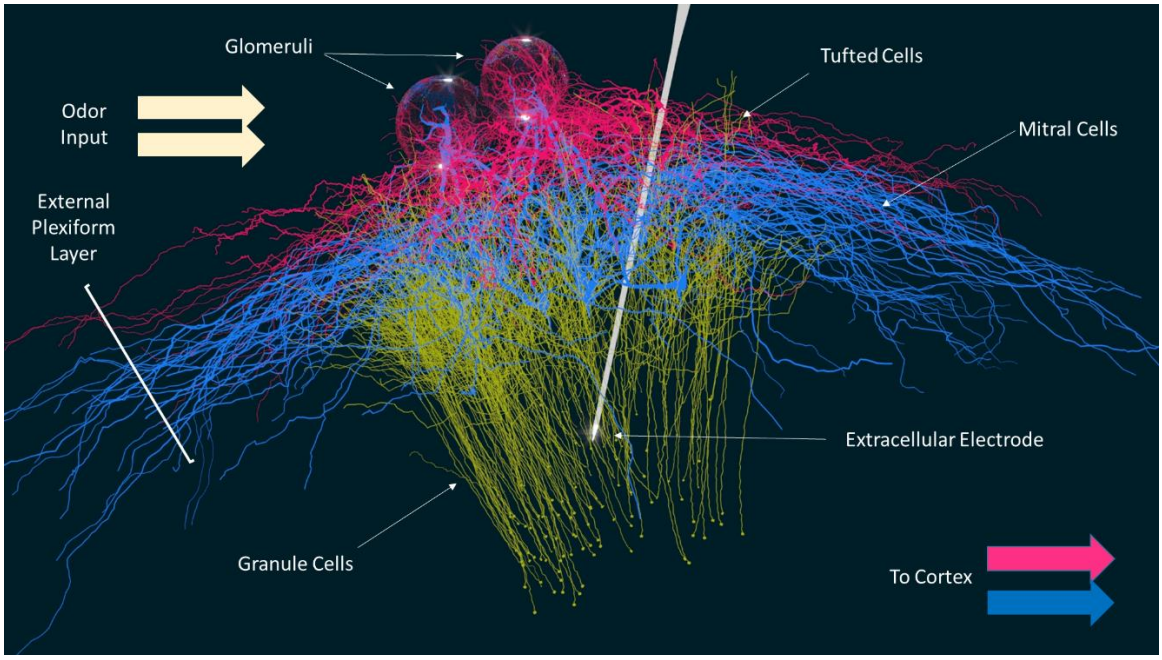

Figure 10: Placement and Dendritic Locations of a Column Slice Model. Mitral cell model (blue) somas are placed in the mitral cell layer, with apical dendrites reaching towards glomeruli, while the lateral dendrites are confined to the deeper portion of the external plexiform layer. Tufted cell (pink) model somas are located throughout the external plexiform layer, while their lateral dendrites are confined to the superficial portion of the external plexiform layer. Granule cell (yellow) model somas are placed in the granule cell layer with apical dendrites extending into the external plexiform layer.

The placement, rotation, apical dendrite alignment, and lateral dendrite confinement is repeated for all cell models specified by the virtual slice. After this step, the model cells are ready to be connected with synapse models. In this model (Figure 10), a virtual 100x100x1000 μm column slice of the dorsal olfactory bulb (Figure 8), contained a total of 10 mitral, 23 tufted, and 170 granule cell models.

2.4 Synapses

Once cell models were placed and oriented, mitral and tufted cell dendrites were connected to the dendrites of granule cell models. Apical tuft dendrites of tufted and mitral cell models were connected with glomerular electrical synapses.

2.4.1 Chemical Synapses

Reciprocal synapses were formed between the dendrites of tufted/mitral and granule cell models based on a proximity rule (Peters & Feldman, 1976). See Rees et. al. (2017) for review of this approach. The Blender API was used to locate dendritic section pairs that were within 5 μm of each other. 5 μm is the typical maximum length of adult mouse granule cell spines (Whitman & Greer, 2007). For each pair, an AMPA/NMDA synapse model (Migliore et al., 2014) monitored mitral/tufted sections for action potentials and, once detected, triggered excitatory currents in the appropriate granule cell model section. In the reverse direction, a GABA synapse model (Migliore et al., 2014) monitored granule sections for action potentials and, once detected, triggered inhibitory currents in the appropriate mitral/tufted cell model sections. With the exception of parameters varied as described in section "3.1 Reproduced Gamma Fingerprint", all other parameters were set to default values.

2.4.2 Electrical Synapses

Electrical synapse models (Stacey, Lazarewicz, & Litt, 2009) were added between tufted cell model apical tuft dendrites that shared glomeruli. Each glomerular tufted cell model was connected to two other tufted cell models in a round robin fashion. The same procedure was used to connect mitral cell model tufts as well.

2.5 Inputs

Once the network was assembled and connected, simulated odors were applied to the glomeruli. Optical imaging recordings of glomerular activity during odor presentation (Vincis, Gschwend, Bhaukaurally, Béroud, & Carleton, 2012) were used

to construct inputs to the network model. Odor triggered maximal activations of glomeruli in the dorsal surface of the olfactory bulb were based on those obtained in a previously published model (Migliore et al., 2014).

To apply odor activations based on Vincis et. al. (2012) to the glomeruli of this model, I identified glomeruli in this model that are homologous to the glomeruli of the Migliore (2014) model. To do this, the mitral cell models of the Migliore (2014) model were imported into Blender and aligned with the glomerular layer of the model developed here. Then, the glomeruli that were closest to the glomeruli of the Migliore model were identified and maximal activations were assigned to them. Given that the glomerular positions in the Migliore et. al. (2014) model were directly mapped from the glomerular positions in Vincis et. al. (2012), the number of glomeruli in this model was selected from experimental distributions (see Table 14), and the glomeruli were uniformly distributed throughout the reconstructed glomerular layer (see "2.2 Layer Reconstruction" and "2.3.3 Glomerular and Soma Locations" sections), the positions of the dorsal glomeruli in this model are expected to correspond well to those observed in Vincis et. al. (2012).

Maximal glomerular activations were combined with a sniffing model to generate simulated olfactory receptor input into mitral/tufted cell model tufted dendrites. Each inhalation was modeled by a train of action potentials whose times were picked from a random Gaussian distribution. The mean and standard deviation of the distribution were chosen so that its 99% range (±2.576 standard deviations) spanned the duration of the inhalation (100-150 ms (Manabe & Mori, 2013)). The number of spikes was set to be proportional to the normalized glomerular activation (0-1) with the maximum scale to correspond to the maximum olfactory receptor firing rate of ~150 Hz (Duchamp-Viret, Duchamp, & Chaput, 2000). Action potential times

outside the 99% range were not allowed. No input action potentials were generated during the exhalation phase (100-300 ms (Manabe & Mori, 2013)).

Action potentials from the sniffing model were monitored by double exponential synapse models (Hines & Carnevale, 1997) that triggered excitatory currents (τ_1=6, τ_2=12 ms (Gilra & Bhalla, 2015a)) in apical tufts of the mitral and tufted cells. Cell models connected to each glomerulus received an appropriate random train of action potentials.

2.6 Outputs

During model development, BlenderNEURON was used to visualize model structure and simulation results. The add-on was configured to monitor all cell model sections and map their membrane potentials to brightness. Blender's "Timeline" feature was then used to replay action potential propagation through the network. To visualize network activity in figures, membrane potentials of all soma sections, grouped by cell type, were plotted over time.

Local field potentials were recorded using the LFPsimpy library (Birgiolas, 2019/2019b) which is an MPI-compatible, Python version of the LFPsim project (Parasuram et al., 2016). To replicated the conditions in the Manabe & Mori (2013) study, an extracellular electrode was placed in the ventral portion of the granule cell layer of the model. The "line source" method was used to compute the extracellular potential sampled at 10 kHz. The recorded potential was band-pass filtered (30-120 Hz) with 4th-order Butterworth filter (Selesnick & Burrus, 1998). For spectral decomposition, the PyWavelets library (Lee, Gommers, Waselewski, Wohlfahrt, & O'Leary, 2019) was used to perform a continuous wavelets transform of the band-pass filtered signal. The wavelet was the 5th-order complex Gaussian with 50 evenly spaced scales ranging from 3 to 32 (corresponding to 30-140 Hz range). The power values of resulting spectrograms of each sniff were sniff-phase aligned and averaged to create

composite sniff local field potential signatures. The spectrogram of the first sniff in the simulation was not used.

2.7 Simulation

The data and source code used to create and validate the model are stored in a public online GitHub repository (Birgiolas, 2018/2019b). The "commit history" feature can be used to examine the line-by-line evolution of the model over time. The SQLite database used for storing experimental database is also stored in the repository and can be downloaded for offline analysis. Similarly, Blender files that store layer information are also in the repository.

The model was architected to be executable on a single machine with multiple cores or multi-machine clusters. This was done using Parallel NEURON (Migliore et al., 2006) features to assign cell models to different parallel processes (MPI ranks). During model initialization, a heap data structure was used to keep track of rank complexity (measured as the number of assigned compartments) and to dynamically assign cell models to the rank with the lowest complexity. Global identifiers were assigned to each pre- and post- synaptic compartment by taking the first 9 digits of the SHA256 hash of the compartment's single rank address. For reproducibility of spike trains in a parallel processing environment, a fixed random seed was assigned to the simulation and to each glomerulus.

Simulations were performed on local and remote machines and machine clusters, each running Ubuntu Linux. Local simulations were performed on a 20-thread Intel i9 7900X machine, while remote simulations were performed either on a 40-thread Intel Xeon E5-2640 v4 machine or a cluster of four 96-thread c5.24xlarge Amazon Web Services instances. Cluster management was performed using the StarCluster package ("STAR: Cluster—Home," 2019).

3 RESULTS

Once the gamma fingerprint was reproduced in the slice model, a series of experimental manipulations were performed to perturb the gamma fingerprint behavior and to test the mechanistic fingerprint hypothesis outlined above.

3.1 Reproduced Gamma Fingerprint

Once the slice network was created, a manual network parameter search was performed (Table 15) until the gamma fingerprint was visible in the local field potential spectrogram (Figure 11).

First, the network was silenced by disabling all reciprocal synapses. The silent network was administered with 9 200 ms long sniffs of "Apple" odor (Migliore et al., 2014; Vincis et al., 2012) at 0.2 relative concentration, which generated a series of random spike trains during each 125 ms inhalation phase. The spikes activated excitatory synapses located on the tufted dendrites of the mitral and tufted cell models. This resulted in clear spiking activity in all mitral and tufted cell models. Then, dendritic tuft electrical synapse conductances were doubled starting from 1 μS until clear synchronization between spikes of mitral and tufted cell populations became apparent at 32 μS. Next, the maximum conductances of AMPA/NMDA synapses were doubled from 1 μS until mitral and tufted cell model spikes were followed by spikes in the majority of companion granule cell models (at 64 μS). Next, the maximum conductances of GABA synapse models were doubled from 0.25 μS until the number of mitral and tufted cell model spikes were reduced by approximately 50%.

Finally, the time constant of the GABA synapse model, and the maximum conductances of the input synapses to tufted and mitral cell models were simultaneously varied until a combination of GABA τ_2 = 36 ms, g_{TC} = 0.8 μS, g_{TC} = 0.2 μS resulted in a clear two cluster pattern in the average local field potential spectrogram (see Figure 11 and Table 15). The same parameter combination elicited

qualitatively similar patterns in response to other odors and their relative concentrations and durations.

Search Parameters (in search order)	Search Range	Fingerprint Range	This Model
Electrical synapse conductance (μS)	0-128	32-128	32
AMPA/NMDA synapse max. conductance (nS)	0-256	64-256	64
GABA synapse max. conductance (μS)	0-8	2-4	2
GABA synapse time constant τ_2 (ms)	0-150	15-50	36
Tufted cell input syn. max. conductance (μS)	0-1	0.6-1	0.8
Mitral cell input syn. max. conductance (μS)	0-1	0.15-0.3	0.2

Table 15: Network Parameters Varied to Identify the Gamma Fingerprint. The six listed parameters were allowed to vary during the parameter search as described in the text. "Fingerprint Range" column shows the parameter value range where a two-cluster fingerprint is visible. The right column provides the set of parameter values that results in a fingerprint that closely matches the experimental fingerprint (Manabe & Mori, 2013).

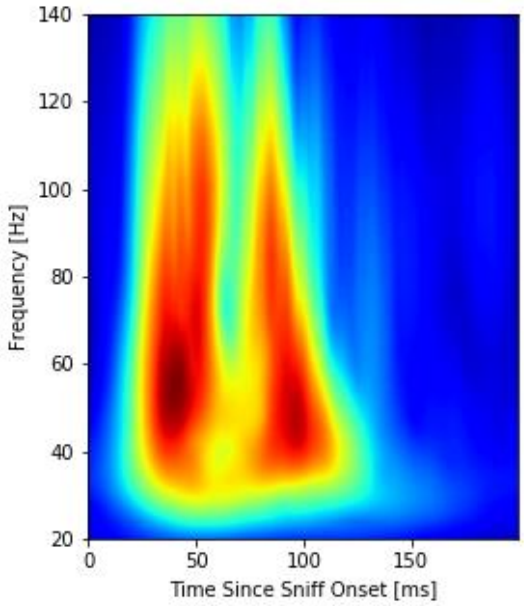

Figure 11: Reproduced Gamma Fingerprint. The two-cluster gamma fingerprint is visible in the average local field potential wavelet spectrogram.

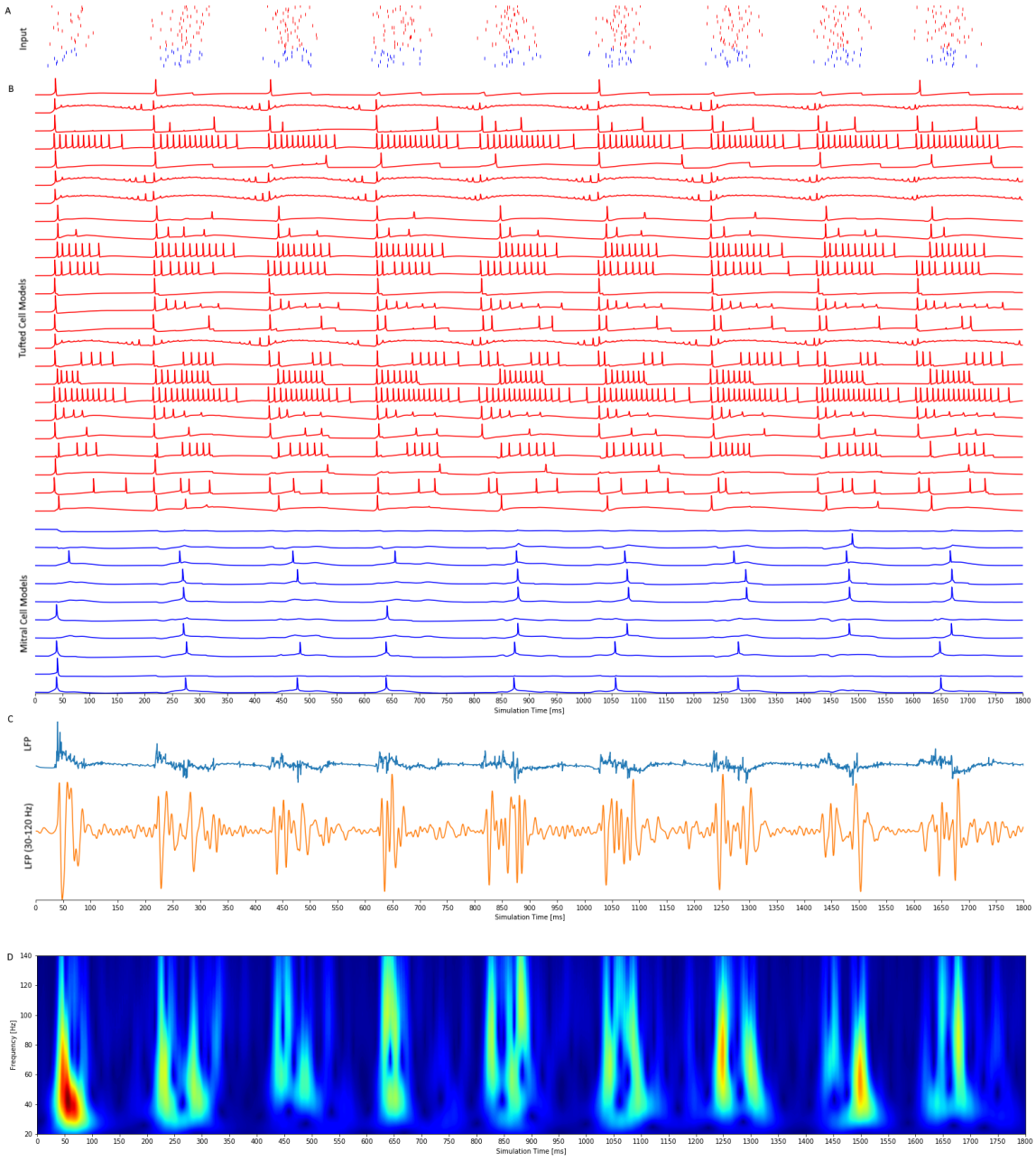

Figure 12: Network Activity Underlying the Gamma Fingerprint. A) Odor input spikes to each principal cell (red: to tufted, blue: to mitral cell models). B) Red and blue curves show somatic membrane potentials of tufted and mitral cell models respectively. C) Blue: The raw local field potential recorded in the granule cell layer. Orange: 30-120 Hz (gamma) filtered, 10-fold amplified version. D) Spectrogram of the continuous wavelet transformation of the band-pass filtered local field potential. Figure 11 is the average of the spectrograms of the last 8 sniffs (first sniff is ignored). Scales are in arbitrary units for visualization purposes.

In this model, each pair of mitral/tufted cell models was connected by one electrical synapse model. Thus, the electrical synapse conductance in Table 15 corresponds to the total conductance of all electrical synapses between a pair of mitral/tufted cells within a glomerulus. The value is consistent with the high coupling observed between intra-glomerular mitral/tufted cell pairs (Schoppa & Westbrook, 2001).

The network model included only a small subset of all cells in the olfactory bulb and did not model input from distant mitral or neighboring granule cells. Because of this and because the values of the conductances of excitatory and inhibitory synapses were chosen to reliably induce granule cell spiking and inhibition of mitral/tufted cells, the conductance values are higher than those observed in experimental preparations (Cang & Isaacson, 2003; Schoppa, Kinzie, Sahara, Segerson, & Westbrook, 1998). I expect that smaller values would be sufficient in larger network models. GABA synapse model time constant was consistent with experimental observations (Chen, Xiong, & Shepherd, 2000; Schoppa et al., 1998).

The four-fold difference of synaptic input strengths between tufted and mitral cells is consistent with experimentally observed charge deposition and firing rate differences between tufted and mitral cells induced by olfactory nerve stimulation (Burton & Urban, 2014; Gire et al., 2012).

To assess the robustness of the selected parameter value set, a one-at-a-time sensitivity analysis (Czitrom, 1999; Daniel, 1973) was performed. Starting with the selected parameter value combination ("This Model" in Table 15) each parameter was varied within its search range while the other parameters remained fixed. The range of parameter values that resulted in the formation of a two-cluster pattern in the spectrogram were noted and summarized in "Fingerprint Range" column of Table 15.

3.2 Effect of Blocking Tufted Cell Model Electrical Synapses

Blocking electrical synapses that connect tufted cell apical tufts was expected to result in reduced synchronization of tufted cell model spiking and be observable as a smearing of the tufted cell gamma cluster. The mitral cell cluster was expected to be preserved but temporally advanced, occurring earlier in the sniff cycle due to reduced delay caused by tufted cell induced inhibition. The results of the reproduced gamma fingerprint simulation with blocked tufted cell electrical synapses (conductances set to 0) agreed with the predictions.

Blocking tufted cell electrical synapses resulted in desynchronized tufted cell spiking onset (see Figure 13). The synchronization of mitral cell spikes remained intact.

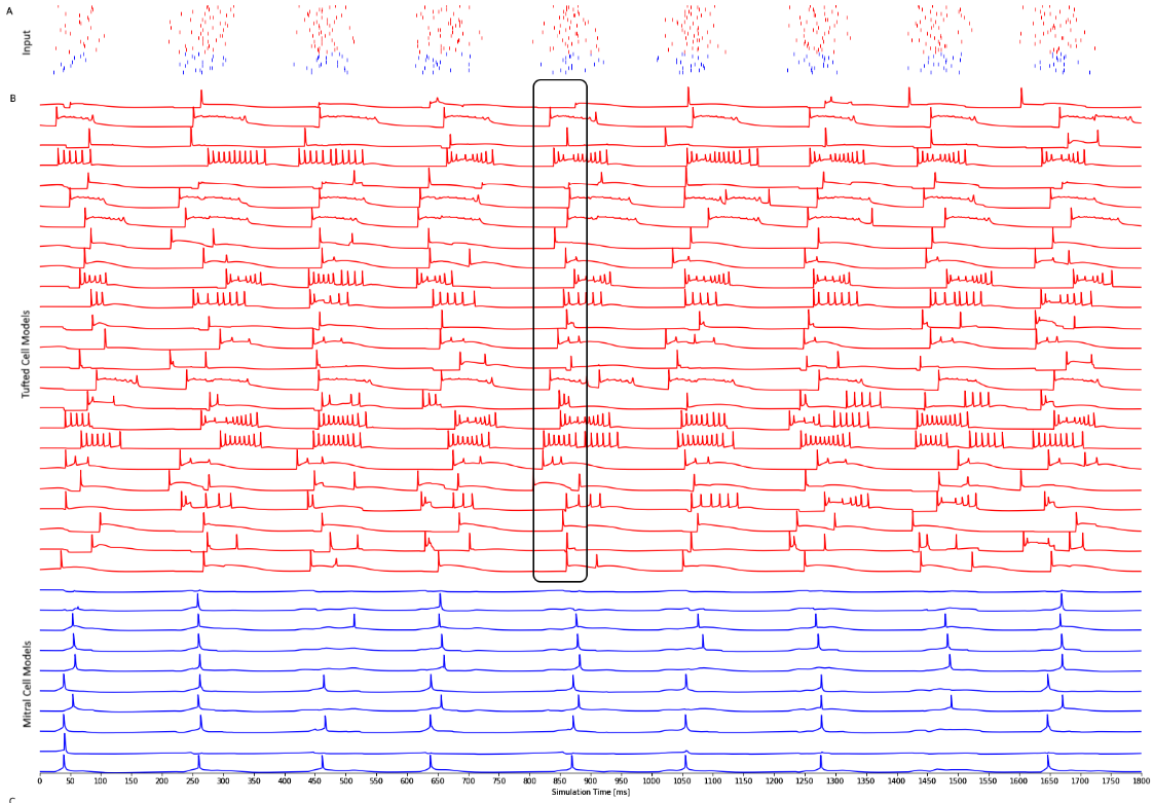

Figure 13: Effect of Blocking Tufted Cell Electrical Synapses on Spike Trains. Blocking tufted cell electrical synapses resulted in desynchronized tufted cell (red) spike onset (compare region to Figure 12). Mitral cell spikes (blue) remained synchronized.

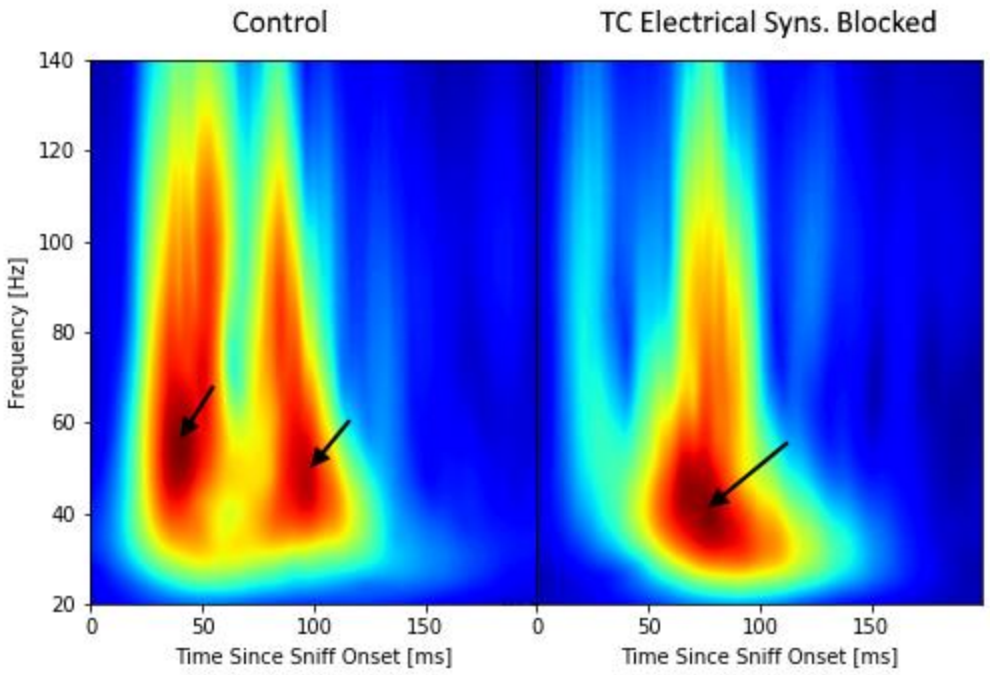

Figure 14: Effect of Blocking Tufted Cell Electrical Synapses on Gamma Activity. Blocking tufted cell electrical synapses abolished the early gamma cluster and advanced the second cluster by approximately 20 ms.

3.3 Effect of Blocking Mitral Cell Model Electrical Synapses

Similar to blocking tufted cell electrical synapses, blocking electrical synapses that connect mitral cell tufted dendrites was expected to reduce mitral cell spiking onset synchronization, while leaving tufted cell synchronization intact. Results of a simulation with blocked mitral cell electrical synapses agreed with the prediction.

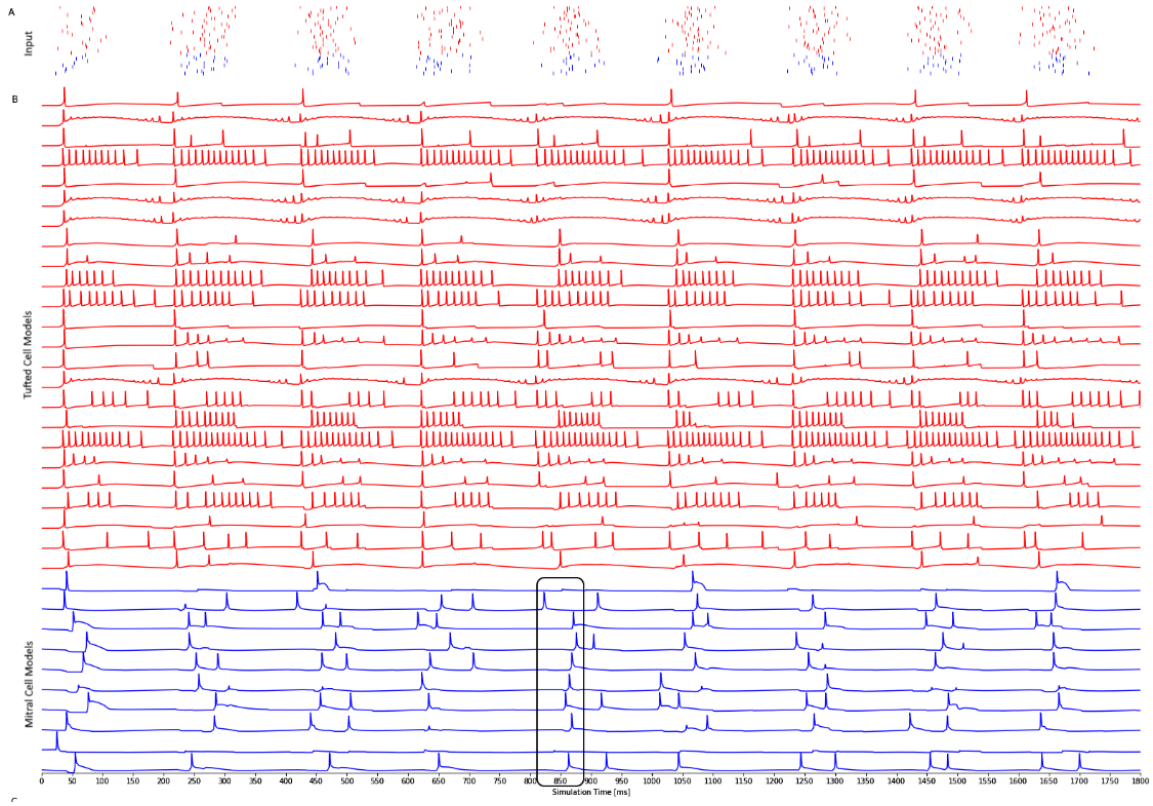

Figure 15: Effect of Blocking Mitral Cell Electrical Synapses on Spike Trains. Blocking electrical synapses connecting mitral cell tufted dendrites results in desynchronized onset of mitral cell (blue) spiking.

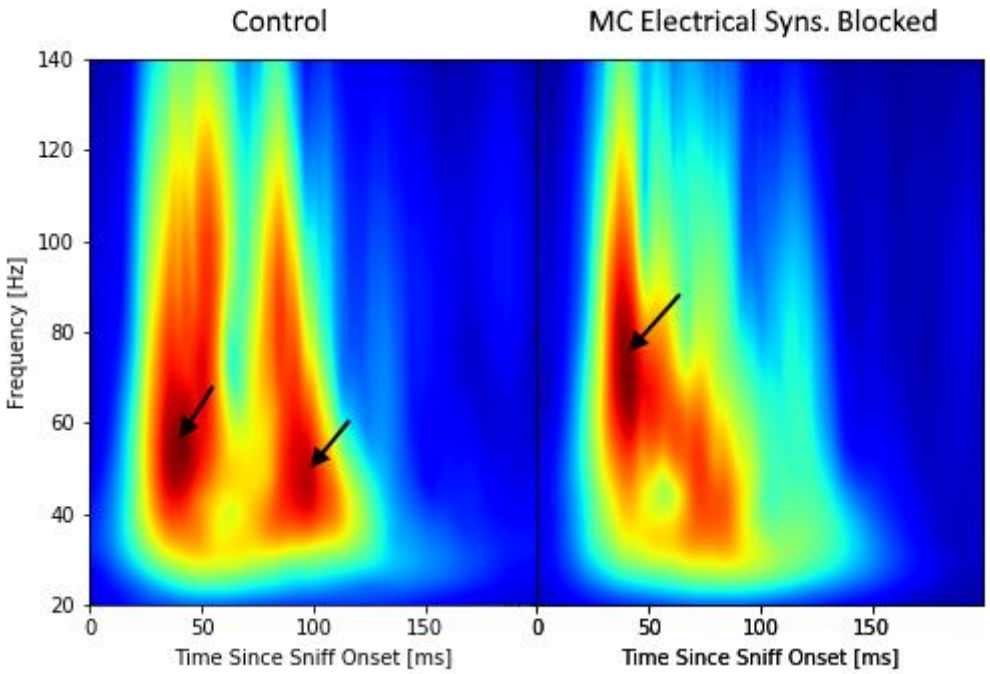

Figure 16: Effect of Blocking Mitral Cell Electrical Synapses on Gamma Activity. Blocking mitral cell electrical synapses preserves the first gamma cluster while abolishing the coherence of the second cluster.

In each sniff cycle, the synchronization of mitral cell spiking onset was reduced, while the tufted cell spike synchronization remained intact (see Figure 15). As expected, this resulted in preservation of the first gamma cluster while the intensity of the second cluster was diminished (Figure 16).

3.4 Effect of Equalizing Mitral and Tufted Cell Model Input Strength

When mitral cell input strength is lower than input to tufted cells, the tufted cells are hypothesized to activate first, and granule cells that share connections between mitral and tufted cells inhibit mitral cells, thus causing a delay in mitral cell spike onset. However, if input strengths of mitral and tufted cells connected to a glomerulus are approximately equal, the two populations are expected to receive a similar amount of post-synaptic excitation and fire at approximately the same time. Without the input strength difference, mitral cell firing should not be delayed and the second cluster should not be formed. Results of a simulation where input strength to

mitral and tufted cell tufted dendrites was equalized (maximum tufted and mitral input synapse conductance = 0.8 μS) agreed with this prediction (Figure 17).

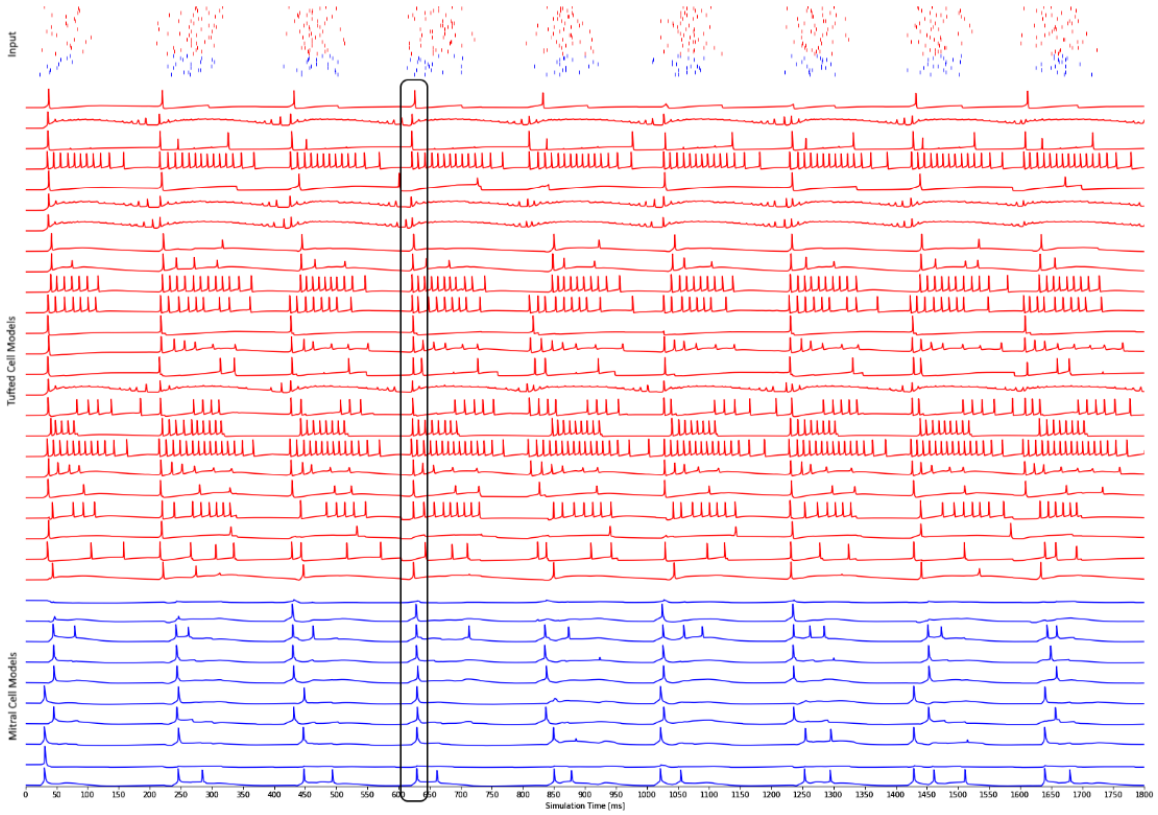

Figure 17: Effect of Equalizing Input Strength on Spike Trains. Equal input strengths to mitral and tufted cells abolish the delay of mitral cell spiking onset

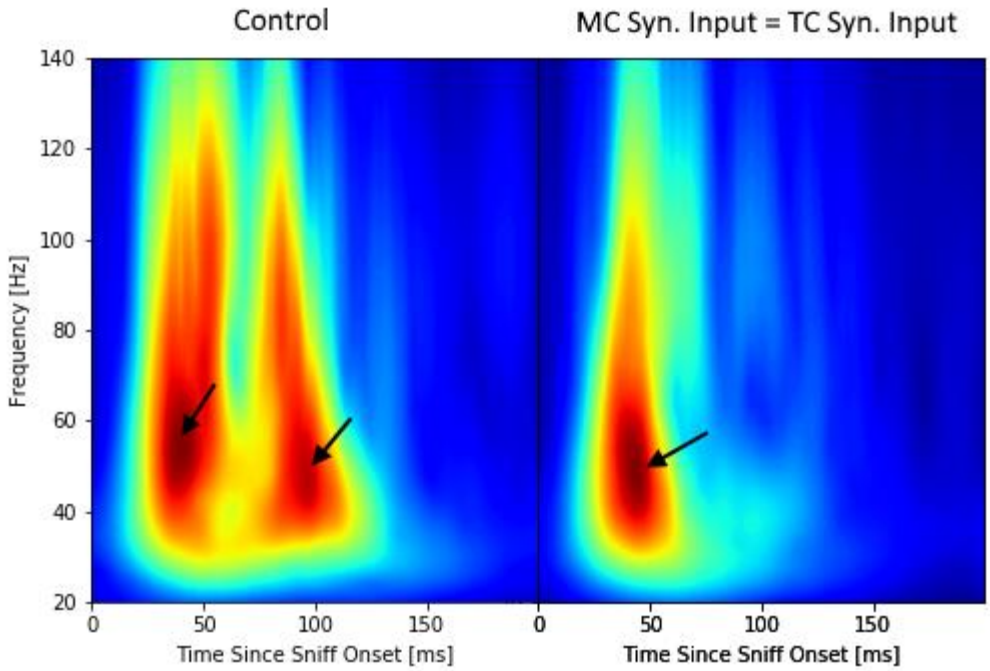

Figure 18: Effect of Equalizing Input Strength on Gamma Activity. Equalizing mitral and tufted cell input results in a single cluster.

When the maximum conductances of mitral and tufted cell input synapses are equalized, the onset of mitral cell spikes is approximately the same as the onset of tufted cell spikes (see Figure 17). In this case, synchronized activity of tufted cells can no longer be distinguished from the synchronized activity of mitral cells in the spectrogram (Figure 18).

3.5 Effect of Blocking Inhibition

In the hypothesis tested here, early inhibition of mitral cells by tufted cell activates granule cells and results in a delay of mitral cell spiking onset. If so, blocking granule cell inhibition should result in the advancement of mitral cell firing onset. The results of a simulation with blocked granule cell GABA synapses (maximum conductance set to 0) agreed with this prediction.

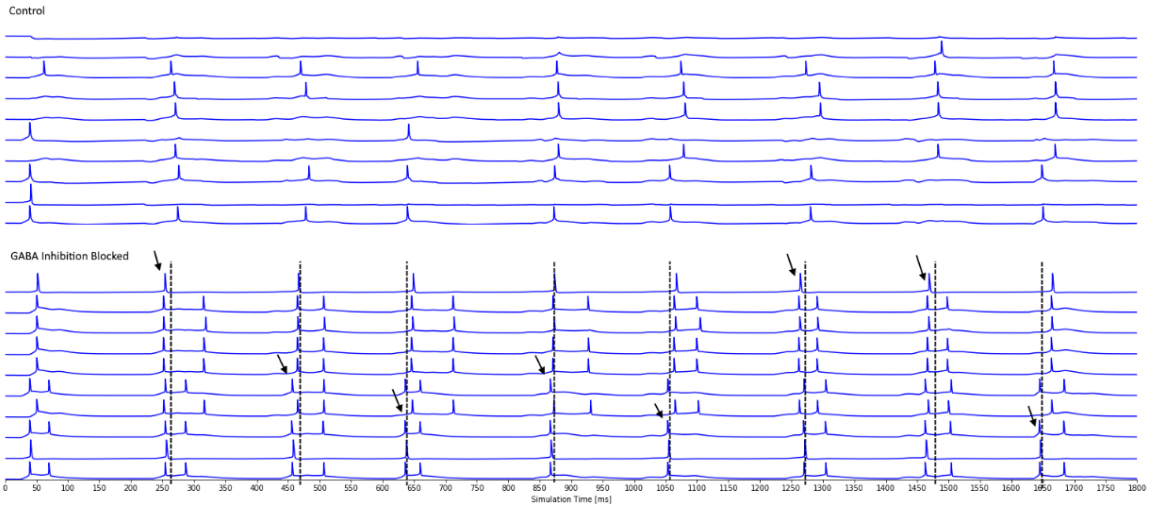

Figure 19: Effect of Inhibition Blocking on Spike Trains. Mitral cell spike onset is advanced when granule cell inhibition is blocked. Dashed lines mark the time of the first mitral cell spike of each sniff in the control condition (inhibition intact). When GABA synapses are blocked, mitral cells spike earlier in each sniff cycle (arrows) than in the control condition.

Blocking inhibition resulted in increased network activity; however, in this experiment the focus is to observe the effect on mitral cell spike onset. In response to glomerular stimulation that is identical to stimulation in the control condition, mitral cells spike earlier in each sniff cycle (Figure 19), demonstrating that granule cell inhibition causes a delay in mitral cell spike onset.

4 DISCUSSION

4.1 Olfactory Bulb Modeling Platform

In this work, published experimental data were aggregated and synthesized into a scalable, extendable, open-source model of the mouse olfactory bulb. Electrophysiology and morphology data of three major cell types were curated and stored in a novel database, which was used to validate previous models and develop novel biophysically realistic models of the three cell types. Labeled slices were used to reconstruct the layer structure of the bulb, within which the novel cell models were placed and oriented using novel open-source software developed for this purpose. The data, models, and software are freely accessible online. When used together, they make up a computational modeling platform that is applicable for modeling a variety of experimental setups.

To demonstrate the utility of the platform, virtual slicing functionality was used to create a model of a glomerular column. The model was then used to reproduce the gamma frequency range oscillation pattern ("gamma fingerprint") observed in extracellular recordings of rodent olfactory bulb. Once reproduced (Figure 11), a mechanistic hypothesis was developed to explain the underlying causes of the fingerprint. The hypothesis was then tested by a series of computational experiments, which can be replicated in experimental investigations.

4.2 Role of Electrical Synapses, Input Strength, and Inhibition

The gamma fingerprint consists of two clusters: early-fast and late-slow. The two clusters correspond to brief periods of synchronized activity in mitral and tufted cell subnetworks in each sniff cycle. Experiments conducted with the olfactory bulb network model, demonstrate the important roles of electrical synapses in formation of the synchronization. Figure 14 and Figure 16 show the effects of blocking electrical synapses between tufted and mitral cells respectively. When electrical synapses

between tufted cells are blocked, tufted cell synchronization is reduced, resulting in elimination of the early-fast gamma cluster in extracellular recordings (Figure 14). Similarly, when electrical synapses between mitral cells are blocked, mitral cells desynchronize, resulting in extinguishment of the late-slow gamma cluster (Figure 16). Thus, electrical synapses between mitral and tufted cell dendritic tufts are necessary for synchronized activity within their respective sub-networks. Electrical synapses are widely expressed in the glomerular layer in mouse (Zhang & Restrepo, 2003) and have been detected between mitral cell tufted dendrites (Christie et al., 2005). While it is not clear if electrical synapses exist between pairs of tufted cell dendrites (Kosaka & Kosaka, 2005), their existence is supported by demonstration of electrical coupling between tufted cell pairs (Ma & Lowe, 2010). This model suggests that electrical synapses exist between tufted cell tufted dendrites and that their blockage or genetic knock-out should disturb the gamma fingerprint.

As discussed earlier, tufted cells have been shown to receive greater effective input than mitral cells (Burton & Urban, 2014; Gire et al., 2012). The model here demonstrates that this property is necessary for the formation of the gamma clusters. When mitral cell input strength was set equal to tufted cell input strength in simulation experiments, mitral cell spiking delay was eliminated (compare mitral cell spike onset in Figure 12 (Control) to Figure 17), and the late-slow gamma cluster fused with the early-fast cluster (Figure 18). The hypothesis for the mechanism underlying this effect is that the delay in mitral cell spiking onset due to reduced input is exaggerated by granule cell inhibition (discussed next). This finding could be tested experimentally, by, for example, monitoring the olfactory receptor activity in a glomerulus and then artificially amplifying mitral cell input via optogenetic stimulation of mitral cell dendritic tufts. Such manipulation should result in the collapse of the second gamma cluster.

Finally, the apical dendrites of "Type I" granule cells span the external plexiform layer (Mori et al., 1983) where they form synapses with dendrites of mitral and tufted cells (Orona et al., 1983). This type of granule cell enables interaction between mitral and tufted cell sub-networks. An experiment with this model demonstrated that granule cell inhibition exaggerates mitral cell spike onset delay caused by reduced mitral cell glomerular input. When granule cell inhibitory GABA synapses were blocked, the delay of mitral cell spike onset was greatly reduced (Figure 19), consistent with the gap between the two gamma clusters. Experimentally, such a finding could be tested by examining the effect of blocking granule cell inhibition on mitral cell spike onsets.

These experiments establish a clear picture of the mechanisms underlying the dynamics of the gamma fingerprint. During each sniff, the early olfactory receptor spikes induce synchronized activity that is mediated by electrical synapses (early-fast cluster) in glomerular tufted cell populations (Figure 20). During this time, due to reduced synaptic input, mitral cell populations have not been excited enough to produce spikes. As action potentials of active tufted cells spread through their lateral dendrites, they excite Type I granule cells. In turn, the granule cells inhibit connected mitral cells, just as they approach their spiking thresholds, suppressing the would-be mitral cell spikes. As inhibition by granule cells subsides and odor input spikes continue to excite mitral cells (Figure 21), mitral cells are able to overcome the early inhibition and produce delayed, electrical synapse synchronized spikes (late-slow cluster).

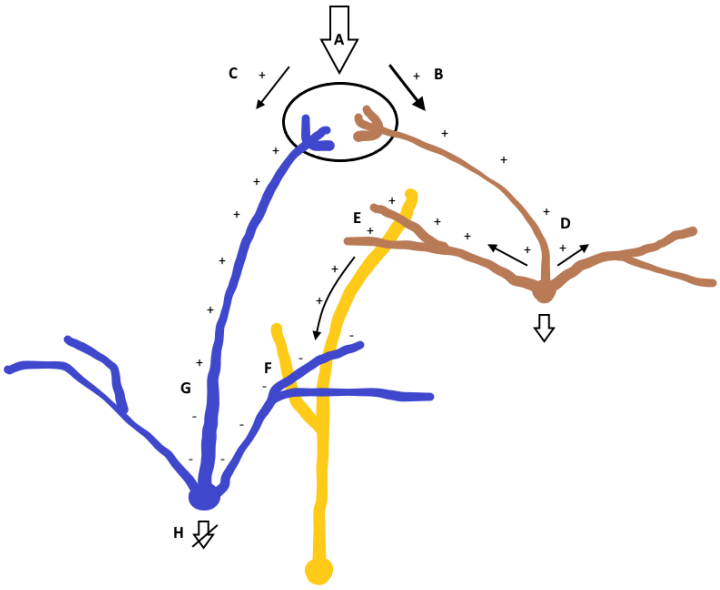

Figure 20: Mechanism of the Early-Fast Cluster of the Gamma Fingerprint. A) Odor input spikes reach a glomerulus shared by tufted (brown) and mitral (blue) cells. B) Tufted cells are more excitable and receive greater input than (C) mitral cells. D) Tufted cells spike first, exciting ('+') granule (gold) cells (E) which inhibit ('-') mitral cells (F). Inhibition spreads to mitral cell soma, canceling the weak incoming glomerular excitation (G) and resulting in a mitral cell spike blockade (H).

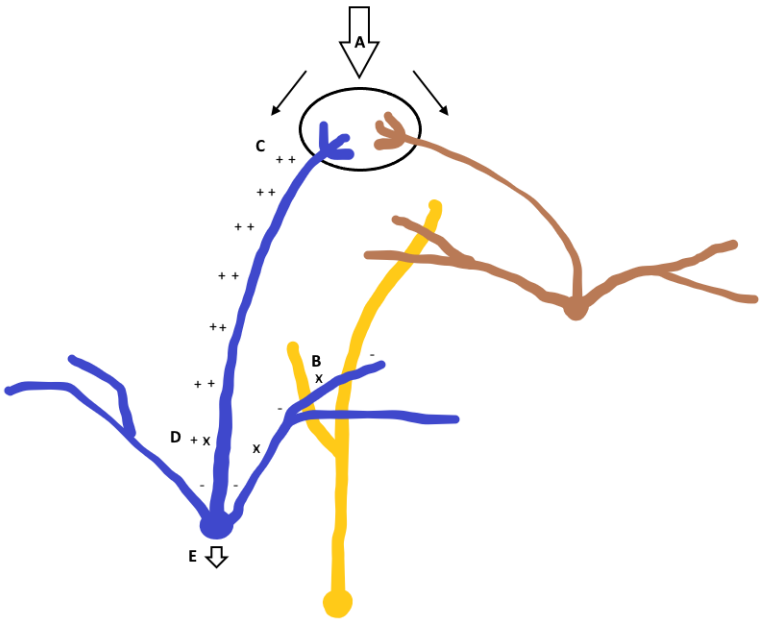

Figure 21: Mechanism of the Late-Slow Cluster of the Gamma Fingerprint. A) After the initial spike blockade, odor input spikes continue to excite the glomerulus during the inhalation phase of a sniff. B) Simultaneously, the initial granule cell inhibition of mitral cells is subsiding ('⁎'s), while excitation continues to build up in the mitral cell apical dendrite (C). D) Glomerular excitation overwhelms the remaining mitral cell inhibition, resulting in a mitral cell spike (E).

4.3 Limitations

One limitation of this study is that the cell models validated against experimental data were all implemented using NEURON. Olfactory models implemented in other simulators (David, Courtiol, Buonviso, & Fourcaud-Trocmé, 2015; Gilra & Bhalla, 2015a) or custom code (Osinski & Kay, 2016) were not evaluated, leaving the possibility that one of those models would have a better correspondence to experimental data. Given the non-trivial amount of effort required to learn the nomenclature of other simulators, conversion of those models to NEURON was not within the scope of this project. However, the NeuronUnit electrophysiology and morphology tests are only dependent on simulator capabilities. If adapter code is written to allow execution of NeuronUnit tests using other simulators, those models could be evaluated and compared to the cell models evaluated here.

Another limitation is imperfect match between experimental morphology and electrophysiology data used to constrain the cell models. Cell model morphologies were taken from intact cell reconstructions, while electrophysiology data was obtained from cells in slices. Dendritic truncations due to slicing, variability in slice bath ionic concentrations (Tripathy et al., 2014), and signal filtering effects due to choice of electrode (e.g. patch pipette, sharp electrode) were not controlled and may contribute to electrical behavior differences between cell models and intact cells. Future modeling studies could constrain the models using data collected under more uniform conditions or replicate the experimental conditions computationally while evaluating the models (similar to how variability in experimental temperature and current injection protocols were replicated during the constraining of novel cell models).

The network parameter set that reproduces the gamma fingerprint was found manually, albeit mostly relying on widely accepted neuroscience principles. It is possible that the parameter combination is not optimal, so that another combination of parameter values could produce a better correspondence to the experimental fingerprint. However, the results of the sensitivity analysis (Table 15) demonstrate that the combination is robust to perturbations in parameter values. Future studies could utilize more automated means to explore the parameter space further and identify other stable parameter combinations.

Besides the three types of cells modeled here, other cells (Burton, 2017; Kosaka, Toida, Aika, & Kosaka, 1998) and mechanisms (Bokil, Laaris, Blinder, Ennis, & Keller, 2001; Schoppa & Westbrook, 2001) could interact to produce a similar fingerprint. For example, there is evidence that mitral cell firing might be primarily driven poly-synaptically by juxtaglomerular cells known as *external* tufted cells rather than by direct mono-synaptic excitation by olfactory receptor neurons (Gire et al., 2012; Najac et al., 2011). Because of the extensible design of this modeling platform, future studies could follow a process similar to the one described here and add additional cells and mechanisms. For example, external tufted cell models could be added to the bulb model and the odor input model could be modified to excite external tufted cells models. The effect of such circuit modification on the gamma fingerprint could be assessed. If the fingerprint could be reproduced using an alternative model, it could be used to form an alternative hypothesis. All alternative models could be inspected and a set of experiments could be identified to efficiently resolve between the alternative explanations.

4.4 Future Directions

The olfactory bulb is involved in depression (Kelly et al., 1997; Negoias et al., 2010), which has been shown to be responsive to ketamine treatments (Murrough et

al., 2013). More recently, administration of ketamine, an NMDA antagonist, has been demonstrated to induce high-frequency oscillations in the olfactory bulb (Hunt et al., 2019). A process similar to this study could be used to reproduce the oscillations and form mechanistic hypotheses of their origin.

The modeling platform supports arbitrary slice shapes (Figure 8). There is some evidence that slice thickness affects gamma oscillations (Cleland, personal communication). Similarly, researchers have proposed that mitral cell bi-stability (Heyward et al., 2001) might be dependent on slice preparation (Burton, personal communication). Such hypotheses could be investigated by adding additional detail to the current model and by adding new functionality to BlenderNEURON to simulate dendritic truncations. The virtual slicing functionality could also be used to construct bulbar models for investigating the function of mediolateral glomerular symmetries and intra-bulbar projections (Zhou & Belluscio, 2008, 2012).

The purpose of the odor information segregation between mitral and tufted cell pathways remains unclear. Examining the differences between glomerular input odor patterns and mitral/tufted output patterns could be used to investigate information processing differences between the two networks.

Another possible use of the model would be to model the effects of synaptic plasticity or effects of the addition of new granule cells (Whitman & Greer, 2007). For example, models of adult-born granule cells could be gradually added to the network model and their effect on network activity investigated.

This model only models the activity of a single olfactory bulb. Future models could include the second bulb and include interactions between them (Shepherd, 2011). A similar process that was used to develop this model (cell validation, layers, cell placement) could be used to develop models of cortical regions that the olfactory bulb is known to interact with (Igarashi et al., 2012; Mori, 2014; Nagayama, Igarashi,

et al., 2014). Such models could then be connected to the bulbar model to gain better understanding of cortical feedback mechanisms.

Finally, in the distant future, as more experimental data is collected, organized, and made accessible, and computing power continues to increase, the data could be synthesized to create models of all brain regions and then assembled into models of whole brains. Such models could receive sensory input and produce output, in the form of behavior, within simulated virtual reality environments. Such models could be used for the development of novel neuropsychopharmaceuticals and reduce the reliance on animal models.

Whole brain emulation refers to the theoretical possibility of creating a computational model of a particular person's brain in sufficient detail that the behavior of the model would be practically indistinguishable from the behavior of the simulated person (Koene, 2012; Sandberg, Bostrom, & Martin, 2008). In the next section, I describe how the discovery of an efficient algorithm to particularize generic biophysically realistic models would result in valuable medical applications and offer a novel route to whole brain emulation.

In the past, models were built from data collected across different species. For example the (Bhalla & Bower, 1993) model incorporated data from mice, rats, rabbits, and turtles to create what can be called "inter-species models". As more data have become available, more recent models (Gilra & Bhalla, 2015b) were constrained by data collected from fewer species: mice and rats. Here, I developed a model constrained only by adult mouse data. If this trend continues, there will be a time where models will be constrained by data collected from a single individual from one species. Brains of conspecifics are simultaneously different and similar, thus when creating a model of a specific individual, a model created from data obtained from conspecific brains would likely be a better starting point than trying to create the

specific model *de novo*. However, the aid of such a model would depend on the existence of an algorithm that could efficiently fine-tune or particularize the more general multi-individual model to a single-individual model. If discovered, such generic-to-individual model fine tuning algorithms could be used to efficiently create biophysically realistic models of brain regions of specific individuals. Such models of specific human brain regions would be useful as neural prostheses for individuals affected by stroke, brain injury, or neurodegenerative disease (Berger & Glanzman, 2005; Berger et al., 2011).

Such fine-tuning is already possible using neural population models developed with the Virtual Brain software (Sanz Leon et al., 2013). For example, models of specific mouse (Melozzi, Woodman, Jirsa, & Bernard, 2017) and human brains (Bansal, Medaglia, Bassett, Vettel, & Muldoon, 2018; Bansal, Nakuci, & Muldoon, 2018) have been created by constraining generic whole brain models with an individual's large-scale brain connectivity and region volume data. Further in the future, similar algorithms could be used to individualize generic biophysically realistic human brain models to models of brains of individual humans. If so, a generic model fine-tuning approach could be another route to whole brain emulation (Sandberg et al., 2008).

BIBLIOGRAPHY

Abraham, N. M., Egger, V., Shimshek, D. R., Renden, R., Fukunaga, I., Sprengel, R., … Kuner, T. (2010). Synaptic Inhibition in the Olfactory Bulb Accelerates Odor Discrimination in Mice. *Neuron*, *65*(3), 399–411. https://doi.org/10.1016/j.neuron.2010.01.009

Angelo, K., Rancz, E. A., Pimentel, D., Hundahl, C., Hannibal, J., Fleischmann, A., … Margrie, T. W. (2012). A biophysical signature of network affiliation and sensory processing in mitral cells. *Nature*, *488*(7411), 375–378. https://doi.org/10.1038/nature11291

Ansari, K. A., & Johnson, A. (1975). Olfactory function in patients with Parkinson's disease. *Journal of Chronic Diseases*, *28*(9), 493–497. https://doi.org/10.1016/0021-9681(75)90058-2

Arnott, S. R., Binns, M. A., Grady, C. L., & Alain, C. (2004). Assessing the auditory dual-pathway model in humans. *NeuroImage*, *22*(1), 401–408. https://doi.org/10.1016/j.neuroimage.2004.01.014

Ascoli, G. A., Donohue, D. E., & Halavi, M. (2007). NeuroMorpho.Org: A central resource for neuronal morphologies. *The Journal of Neuroscience: The Official Journal of the Society for Neuroscience*, *27*(35), 9247–9251. https://doi.org/10.1523/JNEUROSCI.2055-07.2007

Bah, T. (2011). *Inkscape: Guide to a vector drawing program* (Vol. 559). Prentice Hall Upper Saddle River, NJ, USA.

Bansal, K., Medaglia, J. D., Bassett, D. S., Vettel, J. M., & Muldoon, S. F. (2018). Data-driven brain network models differentiate variability across language tasks. *PLOS Computational Biology*, *14*(10), e1006487. https://doi.org/10.1371/journal.pcbi.1006487

Bansal, K., Nakuci, J., & Muldoon, S. F. (2018). Personalized brain network models for assessing structure–function relationships. *Current Opinion in Neurobiology*, *52*, 42–47. https://doi.org/10.1016/j.conb.2018.04.014

Barry, D., & Stanienda, T. (1998). Solving the Java object storage problem. *Computer*, *31*(11), 33–40. https://doi.org/10.1109/2.730734

Belnoue, L., Malvaut, S., Ladevèze, E., Abrous, D. N., & Koehl, M. (2016). Plasticity in the olfactory bulb of the maternal mouse is prevented by gestational stress. *Scientific Reports*, *6*, 37615. https://doi.org/10.1038/srep37615

Benson, T. E., Ryugo, D. K., & Hinds, J. W. (1984). Effects of sensory deprivation on the developing mouse olfactory system: A light and electron microscopic, morphometric analysis. *Journal of Neuroscience*, *4*(3), 638–653. https://doi.org/10.1523/JNEUROSCI.04-03-00638.1984

Berger, T. W., & Glanzman, D. (2005). *Toward replacement parts for the brain: Implantable biomimetic electronics as neural prostheses*. MIT Press.

Berger, T. W., Hampson, R. E., Song, D., Goonawardena, A., Marmarelis, V. Z., & Deadwyler, S. A. (2011). A cortical neural prosthesis for restoring and enhancing memory. *Journal of Neural Engineering*, *8*(4), 046017.

Bezaire, M. J., Raikov, I., Burk, K., Vyas, D., & Soltesz, I. (2016). Interneuronal mechanisms of hippocampal theta oscillations in a full-scale model of the rodent CA1 circuit. *ELife*, *5*. https://doi.org/10.7554/eLife.18566

Bhalla, U. S., & Bower, J. M. (1993). Exploring parameter space in detailed single neuron models: Simulations of the mitral and granule cells of the olfactory bulb. *Journal of Neurophysiology*, *69*(6), 1948–1965.

Birgiolas, J. (2019a). *Hoc2swc*. Retrieved from https://github.com/JustasB/hoc2swc (Original work published 2019)

Birgiolas, J. (2019a). *JustasB/BlenderNEURON* [Python]. Retrieved from https://github.com/JustasB/BlenderNEURON (Original work published 2018)

Birgiolas, J. (2019b). *JustasB/LFPsimpy*. Retrieved from https://github.com/JustasB/LFPsimpy (Original work published 2019)

Birgiolas, J. (2019b). *JustasB/OlfactoryBulb* [Jupyter Notebook]. Retrieved from https://github.com/JustasB/OlfactoryBulb (Original work published 2018)

Birgiolas, J. (2019c). *JustasB/pylmeasure* [HTML]. Retrieved from https://github.com/JustasB/pylmeasure (Original work published 2019)

Birgiolas, J., Gerkin, R. C., & Crook, S. M. (2016). Is the Model Any Good? Objective Criteria for Computational Neuroscience Model Selection. *BMC Neuroscience*, *17*(Suppl 1), O10. https://doi.org/10.1186/s12868-016-0283-6

Birgiolas, J., Gerkin, R. C., & Crook, S. M. (2018). Resources for Modeling in Computational Neuroscience. In *Springer Series in Computational Neuroscience*: *Vol. 2197–1900*. *Hippocampal Microcircuits* (2nd ed., pp. 805–821). Retrieved from https://www.springer.com/us/book/9783319991023

Blender Foundation. (2019). Blender.org. Retrieved October 21, 2019, from Blender.org website: https://www.blender.org/

Bokil, H., Laaris, N., Blinder, K., Ennis, M., & Keller, A. (2001). Ephaptic interactions in the mammalian olfactory system. *Journal of Neuroscience*, *21*(20), RC173–RC173.

BorisTheBrave. (2019). *BorisTheBrave/blue-noise-particles* [Python]. Retrieved from https://github.com/BorisTheBrave/blue-noise-particles (Original work published 2017)

Bourne, J. N., & Schoppa, N. E. (2016). Three-dimensional synaptic analyses of mitral cell and external tufted cell dendrites in rat olfactory bulb glomeruli. *Journal of Comparative Neurology*, n/a-n/a. https://doi.org/10.1002/cne.24089

Boyd, A. M., Kato, H. K., Komiyama, T., & Isaacson, J. S. (2015). Broadcasting of Cortical Activity to the Olfactory Bulb. *Cell Reports*, *10*(7), 1032–1039. https://doi.org/10.1016/j.celrep.2015.01.047

Breton-Provencher, V., Lemasson, M., Peralta, M. R., & Saghatelyan, A. (2009). Interneurons Produced in Adulthood Are Required for the Normal Functioning of the Olfactory Bulb Network and for the Execution of Selected Olfactory Behaviors. *Journal of Neuroscience*, *29*(48), 15245–15257. https://doi.org/10.1523/JNEUROSCI.3606-09.2009

Brown, A. G. (1973). Ascending and Long Spinal Pathways: Dorsal Columns, Spinocervical Tract and Spinothalamic Tract. In A. Iggo (Ed.), *Somatosensory System* (pp. 315–338). https://doi.org/10.1007/978-3-642-65438-1_11

Burton, S. D. (2017). Inhibitory circuits of the mammalian main olfactory bulb. *Journal of Neurophysiology*, *118*(4), 2034–2051. https://doi.org/10.1152/jn.00109.2017

Burton, S. D., LaRocca, G., Liu, A., Cheetham, C. E. J., & Urban, N. N. (2017). Olfactory Bulb Deep Short-Axon Cells Mediate Widespread Inhibition of Tufted Cell Apical Dendrites. *The Journal of Neuroscience: The Official Journal of the Society for Neuroscience*, *37*(5), 1117–1138. https://doi.org/10.1523/JNEUROSCI.2880-16.2016

Burton, S. D., & Urban, N. N. (2014). Greater excitability and firing irregularity of tufted cells underlies distinct afferent-evoked activity of olfactory bulb mitral and tufted cells. *The Journal of Physiology*, *592*(10), 2097–2118. https://doi.org/10.1113/jphysiol.2013.269886

Burton, S. D., & Urban, N. N. (2015). Rapid Feedforward Inhibition and Asynchronous Excitation Regulate Granule Cell Activity in the Mammalian Main Olfactory Bulb. *Journal of Neuroscience*, *35*(42), 14103–14122. https://doi.org/10.1523/JNEUROSCI.0746-15.2015

Cang, J., & Isaacson, J. S. (2003). In Vivo Whole-Cell Recording of Odor-Evoked Synaptic Transmission in the Rat Olfactory Bulb. *Journal of Neuroscience*, *23*(10), 4108–4116. https://doi.org/10.1523/JNEUROSCI.23-10-04108.2003

Case, D. T., Burton, S. D., Gedeon, J. Y., Williams, S.-P. G., Urban, N. N., & Seal, R. P. (2017). Layer- and cell type-selective co-transmission by a basal forebrain cholinergic projection to the olfactory bulb. *Nature Communications*, *8*(1), 652. https://doi.org/10.1038/s41467-017-00765-4

Cavarretta, F., Burton, S. D., Igarashi, K. M., Shepherd, G. M., Hines, M. L., & Migliore, M. (2018). Parallel odor processing by mitral and middle tufted cells in the olfactory bulb. *Scientific Reports*, *8*(1), 1–15. https://doi.org/10.1038/s41598-018-25740-x

Chen, W. R., Shen, G. Y., Shepherd, G. M., Hines, M. L., & Midtgaard, J. (2002). Multiple modes of action potential initiation and propagation in mitral cell primary dendrite. *Journal of Neurophysiology*, *88*(5), 2755–2764. https://doi.org/10.1152/jn.00057.2002

Chen, W. R., & Shepherd, G. M. (1997). Membrane and synaptic properties of mitral cells in slices of rat olfactory bulb. *Brain Research*, *745*(1–2), 189–196.

Chen, W. R., Xiong, W., & Shepherd, G. M. (2000). Analysis of Relations between NMDA Receptors and GABA Release at Olfactory Bulb Reciprocal Synapses. *Neuron*, *25*(3), 625–633. https://doi.org/10.1016/S0896-6273(00)81065-X

Christie, J. M., Bark, C., Hormuzdi, S. G., Helbig, I., Monyer, H., & Westbrook, G. L. (2005). Connexin36 Mediates Spike Synchrony in Olfactory Bulb Glomeruli. *Neuron*, *46*(5), 761–772. https://doi.org/10.1016/j.neuron.2005.04.030

Christie, J. M., & Westbrook, G. L. (2006). Lateral Excitation within the Olfactory Bulb. *Journal of Neuroscience*, *26*(8), 2269–2277.

Christie, Schoppa, N. E., & Westbrook, G. L. (2001). Tufted Cell Dendrodendritic Inhibition in the Olfactory Bulb Is Dependent on NMDA Receptor Activity. *Journal of Neurophysiology*, *85*(1), 169–173.

Czitrom, V. (1999). One-Factor-at-a-Time versus Designed Experiments. *The American Statistician*, *53*(2), 126–131. https://doi.org/10.1080/00031305.1999.10474445

Dahlen, J. E., Jimenez, D. A., Gerkin, R. C., & Urban, N. N. (2011). Morphological analysis of activity-reduced adult-born neurons in the mouse olfactory bulb. *Frontiers in Neuroscience*, *5*, 66. https://doi.org/10.3389/fnins.2011.00066

Daniel, C. (1973). One-at-a-Time Plans. *Journal of the American Statistical Association*, *68*(342), 353–360. https://doi.org/10.1080/01621459.1973.10482433

Daroles, L., Gribaudo, S., Doulazmi, M., Scotto-Lomassese, S., Dubacq, C., Mandairon, N., … Caillé, I. (2016). Fragile X Mental Retardation Protein and Dendritic Local Translation of the Alpha Subunit of the Calcium/Calmodulin-Dependent Kinase II Messenger RNA Are Required for the Structural Plasticity Underlying Olfactory Learning. *Biological Psychiatry*, *80*(2), 149–159. https://doi.org/10.1016/j.biopsych.2015.07.023

David, F., Courtiol, E., Buonviso, N., & Fourcaud-Trocmé, N. (2015). Competing Mechanisms of Gamma and Beta Oscillations in the Olfactory Bulb Based on Multimodal Inhibition of Mitral Cells Over a Respiratory Cycle. *ENeuro*, *2*(6). https://doi.org/10.1523/ENEURO.0018-15.2015

David, F., Linster, C., & Cleland, T. A. (2008). Lateral dendritic shunt inhibition can regularize mitral cell spike patterning. *Journal of Computational Neuroscience*, *25*(1), 25–38. https://doi.org/10.1007/s10827-007-0063-5

Davison, Feng, J., & Brown, D. (2000). A reduced compartmental model of the mitral cell for use in network models of the olfactory bulb. *Brain Research Bulletin*, *51*(5), 393–399. https://doi.org/10.1016/s0361-9230(99)00256-7

Davison, Feng, J., & Brown, D. (2003). Dendrodendritic Inhibition and Simulated Odor Responses in a Detailed Olfactory Bulb Network Model. *Journal of Neurophysiology*, *90*(3), 1921–1935. https://doi.org/10.1152/jn.00623.2002

Denizet, M., Cotter, L., Lledo, P.-M., & Lazarini, F. (2017). Sensory deprivation increases phagocytosis of adult-born neurons by activated microglia in the olfactory bulb. *Brain, Behavior, and Immunity*, *60*, 38–43. https://doi.org/10.1016/j.bbi.2016.09.015

Desmaisons, D., Vincent, J.-D., & Lledo, P.-M. (1999). Control of action potential timing by intrinsic subthreshold oscillations in olfactory bulb output neurons. *Journal of Neuroscience*, *19*(24), 10727–10737.

Djurisic, M., Popovic, M., Carnevale, N., & Zecevic, D. (2008). Functional structure of the mitral cell dendritic tuft in the rat olfactory bulb. *The Journal of Neuroscience: The Official Journal of the Society for Neuroscience*, *28*(15), 4057–4068. https://doi.org/10.1523/JNEUROSCI.5296-07.2008

Duchamp-Viret, P., Duchamp, A., & Chaput, M. A. (2000). Peripheral Odor Coding in the Rat and Frog: Quality and Intensity Specification. *Journal of Neuroscience*, *20*(6), 2383–2390. https://doi.org/10.1523/JNEUROSCI.20-06-02383.2000

Dudani, N., Ray, S., George, S., & Bhalla, U. S. (2009). Multiscale modeling and interoperability in MOOSE. *BMC Neuroscience*, *10*(1), 1.

Dura-Bernal, S., Suter, B. A., Neymotin, S. A., Kerr, C. C., Quintana, A., Gleeson, Padraig, … Lytton, William. (2016). NetPyNE: a Python package for NEURON to facilitate development and parallel simulation of biological neuronal networks. *BMC Neuroscience*, *17*(Suppl 1), P105.

Ekstrand, J. J., Domroese, M. E., Johnson, D. M. G., Feig, S. L., Knodel, S. M., Behan, M., & Haberly, L. B. (2001). A new subdivision of anterior piriform cortex and associated deep nucleus with novel features of interest for olfaction and epilepsy. *The Journal of Comparative Neurology*, *434*(3), 289–307. https://doi.org/10.1002/cne.1178

Feng, L., Zhao, T., & Kim, J. (2015). neuTube 1.0: A New Design for Efficient Neuron Reconstruction Software Based on the SWC Format. *ENeuro*, *2*(1), ENEURO.0049-14.2014. https://doi.org/10.1523/ENEURO.0049-14.2014

Fitzgerald, J. E., Bui, E. T. H., Simon, N. M., & Fenniri, H. (2017). Artificial Nose Technology: Status and Prospects in Diagnostics. *Trends in Biotechnology*, *35*(1), 33–42. https://doi.org/10.1016/j.tibtech.2016.08.005

Fleischer, J., Breer, H., Strotmann, J., Fleischer, J., Breer, H., & Strotmann, J. (2009). Mammalian olfactory receptors. *Frontiers in Cellular Neuroscience*, *3*, 9. https://doi.org/10.3389/neuro.03.009.2009

Fortin, F.-A., Rainville, F.-M. D., Gardner, M.-A., Parizeau, M., & Gagné, C. (2012). DEAP: Evolutionary Algorithms Made Easy. *Journal of Machine Learning Research*, *13*, 2171–2175.

Fourcaud-Trocmé, N., Courtiol, E., & Buonviso, N. (2014). Two distinct olfactory bulb sublaminar networks involved in gamma and beta oscillation generation: A CSD study in the anesthetized rat. *Frontiers in Neural Circuits*, *8*. https://doi.org/10.3389/fncir.2014.00088

Fukunaga, I., Berning, M., Kollo, M., Schmaltz, A., & Schaefer, A. T. (2012). Two Distinct Channels of Olfactory Bulb Output. *Neuron*, *75*(2), 320–329. https://doi.org/10.1016/j.neuron.2012.05.017

Fukunaga, I., Herb, J., Kollo, M., Boyden, E. S., & Schaefer, A. T. (2014). Independent control of gamma and theta activity by distinct interneuron networks in the olfactory bulb. *Nature Neuroscience*, *17*(9), 1208–1216. https://doi.org/10.1038/nn.3760

Gerkin, R. C., Birgiolas, J., Jarvis, R. J., Omar, C., & Crook, S. M. (2019). NeuronUnit: A package for data-driven validation of neuron models using SciUnit. *BioRxiv*, 665331. https://doi.org/10.1101/665331

Gheusi, G., Cremer, H., McLean, H., Chazal, G., Vincent, J.-D., & Lledo, P.-M. (2000). Importance of newly generated neurons in the adult olfactory bulb for odor discrimination. *Proceedings of the National Academy of Sciences*, *97*(4), 1823–1828. https://doi.org/10.1073/pnas.97.4.1823

Gilra, A., & Bhalla, U. S. (2015a). Bulbar Microcircuit Model Predicts Connectivity and Roles of Interneurons in Odor Coding. *PLOS ONE*, *10*(5), e0098045. https://doi.org/10.1371/journal.pone.0098045

Gilra, A., & Bhalla, U. S. (2015b). Bulbar Microcircuit Model Predicts Connectivity and Roles of Interneurons in Odor Coding. *PLOS ONE*, *10*(5), e0098045. https://doi.org/10.1371/journal.pone.0098045

Gire, D. H., Franks, K. M., Zak, J. D., Tanaka, K. F., Whitesell, J. D., Mulligan, A. A., … Schoppa, N. E. (2012). Mitral cells in the olfactory bulb are mainly excited through a multistep signaling path. *The Journal of Neuroscience: The Official Journal of the Society for Neuroscience*, *32*(9), 2964–2975. https://doi.org/10.1523/JNEUROSCI.5580-11.2012

Gleeson, P., Cantarelli, M., Marin, B., Quintana, A., Earnshaw, M., Sadeh, S., … Silver, R. A. (2019). Open Source Brain: A Collaborative Resource for Visualizing, Analyzing, Simulating, and Developing Standardized Models of Neurons and Circuits. *Neuron*, *103*(3), 395-411.e5. https://doi.org/10.1016/j.neuron.2019.05.019

Golgi, C. (1875). Sulla fina struttura dei bulbi olfacttoria. *Riv. Sper. Freniatria Med. Legal.*, *1*, 66–78.

Gopinath, B., Anstey, K. J., Sue, C. M., Kifley, A., & Mitchell, P. (2011). Olfactory Impairment in Older Adults Is Associated With Depressive Symptoms and Poorer Quality of Life Scores. *The American Journal of Geriatric Psychiatry*, *19*(9), 830–834. https://doi.org/10.1097/JGP.0b013e318211c205

Haehner, A., Boesveldt, S., Berendse, H. W., Mackay-Sim, A., Fleischmann, J., Silburn, P. A., … Hummel, T. (2009). Prevalence of smell loss in Parkinson's disease – A multicenter study. *Parkinsonism & Related Disorders*, *15*(7), 490–494. https://doi.org/10.1016/j.parkreldis.2008.12.005

Heyward, P., Ennis, M., Keller, A., & Shipley, M. T. (2001). Membrane bistability in olfactory bulb mitral cells. *Journal of Neuroscience*, *21*(14), 5311–5320.

Hines, & Carnevale, N. T. (1997). The NEURON Simulation Environment. *Neural Computation*, *9*(6), 1179–1209. https://doi.org/10.1162/neco.1997.9.6.1179

Hines, Morse, T., Migliore, M., Carnevale, N. T., & Shepherd, G. M. (2004). ModelDB: A Database to Support Computational Neuroscience. *Journal of Computational Neuroscience*, *17*(1), 7–11. https://doi.org/10.1023/B:JCNS.0000023869.22017.2e

Hodgkin, A. L., & Huxley, A. F. (1952). A quantitative description of membrane current and its application to conduction and excitation in nerve. *The Journal of Physiology*, *117*(4), 500–544.

Hovis, K. R., Padmanabhan, K., & Urban, N. N. (2010). A simple method of in vitro electroporation allows visualization, recording, and calcium imaging of local neuronal circuits. *Journal of Neuroscience Methods*, *191*(1), 1–10. https://doi.org/10.1016/j.jneumeth.2010.05.017

Hu, R., Ferguson, K. A., Whiteus, C. B., Meijer, D. H., & Araneda, R. C. (2016). Hyperpolarization-Activated Currents and Subthreshold Resonance in Granule Cells of the Olfactory Bulb. *ENeuro*, *3*(5), ENEURO.0197-16.2016. https://doi.org/10.1523/ENEURO.0197-16.2016

Hunt, M. J., Adams, N. E., Średniawa, W., Wójcik, D. K., Simon, A., Kasicki, S., & Whittington, M. A. (2019). The olfactory bulb is a source of high-frequency oscillations (130–180 Hz) associated with a subanesthetic dose of ketamine in rodents. *Neuropsychopharmacology*, *44*(2), 435–442. https://doi.org/10.1038/s41386-018-0173-y

Igarashi, K. M., Ieki, N., An, M., Yamaguchi, Y., Nagayama, S., Kobayakawa, K., … Mori, K. (2012). Parallel Mitral and Tufted Cell Pathways Route Distinct Odor Information to Different Targets in the Olfactory Cortex. *Journal of Neuroscience*, *32*(23), 7970–7985. https://doi.org/10.1523/JNEUROSCI.0154-12.2012

Interactive Atlas Viewer: Atlas Viewer. (2019). Retrieved October 12, 2019, from https://atlas.brain-map.org/atlas?atlas=1#atlas=1&plate=100960504&structure=507&x=3143.9998372395835&y=2187.999979654948&zoom=-2&resolution=6.98&z=5

Johnston, J., & Delaney, K. R. (2010). Synaptic activation of T-type Ca2+ channels via mGluR activation in the primary dendrite of mitral cells. *Journal of Neurophysiology*, *103*(5), 2557–2569. https://doi.org/10.1152/jn.00796.2009

Jr, W. D. W. (1985). Central Nervous System Mechanisms for Pain Modulation. *Stereotactic and Functional Neurosurgery*, *48*(1–6), 153–165. https://doi.org/10.1159/000101121

Kaplan, B. A., & Lansner, A. (2014). A spiking neural network model of self-organized pattern recognition in the early mammalian olfactory system. *Frontiers in Neural Circuits*, *8*. https://doi.org/10.3389/fncir.2014.00005

Ke, M.-T., Fujimoto, S., & Imai, T. (2013). SeeDB: A simple and morphology-preserving optical clearing agent for neuronal circuit reconstruction. *Nature Neuroscience*, *16*(8), 1154–1161. https://doi.org/10.1038/nn.3447

Kelly, J. P., Wrynn, A. S., & Leonard, B. E. (1997). The olfactory bulbectomized rat as a model of depression: An update. *Pharmacology & Therapeutics*, *74*(3), 299–316. https://doi.org/10.1016/S0163-7258(97)00004-1

Kenny, P. J. (2011). Common cellular and molecular mechanisms in obesity and drug addiction. *Nature Reviews Neuroscience*, *12*(11), 638–651. https://doi.org/10.1038/nrn3105

Kikuta, S., Fletcher, M. L., Homma, R., Yamasoba, T., & Nagayama, S. (2013). Odorant Response Properties of Individual Neurons in an Olfactory Glomerular Module. *Neuron*, *77*(6), 1122–1135. https://doi.org/10.1016/j.neuron.2013.01.022

Kishi, K., Mori, K., & Ojima, H. (1984). Distribution of local axon collaterals of mitral, displaced mitral, and tufted cells in the rabbit olfactory bulb. *The Journal of Comparative Neurology*, *225*(4), 511–526. https://doi.org/10.1002/cne.902250404

Koene, R. A. (2012). Fundamentals of whole brain emulation: State, transition and update representations. *International Journal of Machine Consciousness*, *4*(01), 5–21.

Kosaka, K., Toida, K., Aika, Y., & Kosaka, T. (1998). How simple is the organization of the olfactory glomerulus?: The heterogeneity of so-called periglomerular cells. *Neuroscience Research*, *30*(2), 101–110. https://doi.org/10.1016/S0168-0102(98)00002-9

Kosaka, & Kosaka, K. (2005). Intraglomerular dendritic link connected by gap junctions and chemical synapses in the mouse main olfactory bulb: Electron microscopic serial section analyses. *Neuroscience*, *131*(3), 611–625. https://doi.org/10.1016/j.neuroscience.2004.11.050

Lee, G., Gommers, R., Waselewski, F., Wohlfahrt, K., & O'Leary, A. (2019, April 12). PyWavelets: A Python package for wavelet analysis. https://doi.org/10.21105/joss.01237

Leifer, C. (2019). *Coleifer/peewee* [Python]. Retrieved from https://github.com/coleifer/peewee (Original work published 2010)

Li, G., & Cleland, T. A. (2013). A Two-Layer Biophysical Model of Cholinergic Neuromodulation in Olfactory Bulb. *Journal of Neuroscience*, *33*(7), 3037–3058. https://doi.org/10.1523/JNEUROSCI.2831-12.2013

Lindén, H., Hagen, E., Leski, S., Norheim, E. S., Pettersen, K. H., & Einevoll, G. T. (2014). LFPy: A tool for biophysical simulation of extracellular potentials generated by detailed model neurons. *Frontiers in Neuroinformatics*, *7*. https://doi.org/10.3389/fninf.2013.00041

L-Measure functions. (n.d.). Retrieved October 9, 2019, from http://cng.gmu.edu:8080/Lm/help/index.htm

Ma, J., & Lowe, G. (2010). Correlated firing in tufted cells of mouse olfactory bulb. *Neuroscience*, *169*(4), 1715–1738. https://doi.org/10.1016/j.neuroscience.2010.06.033

Maher, B. J., McGinley, M. J., & Westbrook, G. L. (2009). Experience-dependent maturation of the glomerular microcircuit. *Proceedings of the National Academy of Sciences*, *106*(39), 16865–16870.

Manabe, H., & Mori, K. (2013). Sniff rhythm-paced fast and slow gamma-oscillations in the olfactory bulb: Relation to tufted and mitral cells and behavioral states. *Journal of Neurophysiology*, *110*(7), 1593–1599. https://doi.org/10.1152/jn.00379.2013

Maresh, A., Gil, D. R., Whitman, M. C., & Greer, C. A. (2008). Principles of Glomerular Organization in the Human Olfactory Bulb – Implications for Odor Processing. *PLOS ONE*, *3*(7), e2640. https://doi.org/10.1371/journal.pone.0002640

Markou, A., Kosten, T. R., & Koob, G. F. (1998). Neurobiological similarities in depression and drug dependence: A self-medication hypothesis. *Neuropsychopharmacology*, *18*(3), 135–174. https://doi.org/10.1016/S0893-133X(97)00113-9

Markram, H., Muller, E., Ramaswamy, S., Reimann, M. W., Abdellah, M., Sanchez, C. A., … Schürmann, F. (2015). Reconstruction and Simulation of Neocortical Microcircuitry. *Cell*, *163*(2), 456–492. https://doi.org/10.1016/j.cell.2015.09.029

Maunsell, J. H., Nealey, T. A., & DePriest, D. D. (1990). Magnocellular and parvocellular contributions to responses in the middle temporal visual area (MT) of the macaque monkey. *Journal of Neuroscience*, *10*(10), 3323–3334.

McDole, B., Isgor, C., Pare, C., & Guthrie, K. (2015). BDNF over-expression increases olfactory bulb granule cell dendritic spine density in vivo. *Neuroscience*, *304*, 146–160. https://doi.org/10.1016/j.neuroscience.2015.07.056

McDougal, R. A., Wang, R., Morse, T. M., Migliore, M., Marenco, L., Carnevale, T., … Shepherd, G. M. (2015). ModelDB. *Encyclopedia of Computational Neuroscience*, 1727–1730.

McGann, J. P. (2017). Poor human olfaction is a 19th-century myth. *Science*, *356*(6338). https://doi.org/10.1126/science.aam7263

McTavish, T. S., Migliore, M., Shepherd, G. M., & Hines, M. L. (2012). Mitral cell spike synchrony modulated by dendrodendritic synapse location. *Frontiers in Computational Neuroscience*, *6*, 3. https://doi.org/10.3389/fncom.2012.00003

Melozzi, F., Woodman, M. M., Jirsa, V. K., & Bernard, C. (2017). The Virtual Mouse Brain: A Computational Neuroinformatics Platform to Study Whole Mouse Brain Dynamics. *ENeuro*, *4*(3). https://doi.org/10.1523/ENEURO.0111-17.2017

Migliore, Cannia, C., Lytton, W. W., Markram, H., & Hines, M. L. (2006). Parallel Network Simulations with NEURON. *Journal of Computational Neuroscience*, *21*(2), 119–129. https://doi.org/10.1007/s10827-006-7949-5

Migliore, Cavarretta, F., Hines, M. L., & Shepherd, G. M. (2014). Distributed organization of a brain microcircuit analyzed by three-dimensional modeling: The olfactory bulb. *Frontiers in Computational Neuroscience*, *8*. https://doi.org/10.3389/fncom.2014.00050

Migliore, Cavarretta, F., Marasco, A., Tulumello, E., Hines, M. L., & Shepherd, G. M. (2015). Synaptic clusters function as odor operators in the olfactory bulb. *Proceedings of the National Academy of Sciences*, *112*(27), 8499–8504. https://doi.org/10.1073/pnas.1502513112

Migliore, Hines, M. L., & Shepherd, G. M. (2005). The role of distal dendritic gap junctions in synchronization of mitral cell axonal output. *Journal of Computational Neuroscience*, *18*(2), 151–161. https://doi.org/10.1007/s10827-005-6556-1

Migliore, M., Inzirillo, C., & Shepherd, G. M. (2007). Learning mechanism for column formation in the olfactory bulb. *Frontiers in Integrative Neuroscience*, *1*, 12. https://doi.org/10.3389/neuro.07.012.2007

Migliore, & McTavish, T. (2013). Olfactory Computation in Mitral-Granule Cell Circuits. In R. Jung (Ed.), *Encyclopedia of Computational Neuroscience* (pp. 1–4). https://doi.org/10.1007/978-1-4614-7320-6_615-4

Migliore, & Shepherd, G. M. (2008). Dendritic action potentials connect distributed dendrodendritic microcircuits. *Journal of Computational Neuroscience*, *24*(2), 207–221. https://doi.org/10.1007/s10827-007-0051-9

Mori, K. (2014). Piriform Cortex and Olfactory Tubercle. In K. Mori (Ed.), *The Olfactory System* (pp. 161–175). https://doi.org/10.1007/978-4-431-54376-3_8

Mori, K., Kishi, K., & Ojima, H. (1983). Distribution of dendrites of mitral, displaced mitral, tufted, and granule cells in the rabbit olfactory bulb. *The Journal of Comparative Neurology*, *219*(3), 339–355. https://doi.org/10.1002/cne.902190308

Mori, K., & Manabe, H. (2014). Unique Characteristics of the Olfactory System. In K. Mori (Ed.), *The Olfactory System* (pp. 1–18). https://doi.org/10.1007/978-4-431-54376-3_1

Murai, A., Iwata, R., Fujimoto, S., Aihara, S., Tsuboi, A., Muroyama, Y., … Imai, T. (2016). Distorted Coarse Axon Targeting and Reduced Dendrite Connectivity Underlie Dysosmia after Olfactory Axon Injury. *ENeuro*, *3*(5). https://doi.org/10.1523/ENEURO.0242-16.2016

Murrough, J. W., Iosifescu, D. V., Chang, L. C., Al Jurdi, R. K., Green, C. E., Perez, A. M., … Shah, A. (2013). Antidepressant efficacy of ketamine in treatment-resistant major depression: A two-site randomized controlled trial. *American Journal of Psychiatry*, *170*(10), 1134–1142.

Nagayama, S., Homma, R., & Imamura, F. (2014). Neuronal organization of olfactory bulb circuits. *Frontiers in Neural Circuits*, *8*. https://doi.org/10.3389/fncir.2014.00098

Nagayama, S., Igarashi, K. M., Manabe, H., & Mori, K. (2014). Parallel Tufted Cell and Mitral Cell Pathways from the Olfactory Bulb to the Olfactory Cortex. In K. Mori (Ed.), *The Olfactory System* (pp. 133–160). https://doi.org/10.1007/978-4-431-54376-3_7

Nagayama, S., Takahashi, Y. K., Yoshihara, Y., & Mori, K. (2004). Mitral and Tufted Cells Differ in the Decoding Manner of Odor Maps in the Rat Olfactory Bulb. *Journal of Neurophysiology*, *91*(6), 2532–2540. https://doi.org/10.1152/jn.01266.2003

Najac, M., Jan, D. D. S., Reguero, L., Grandes, P., & Charpak, S. (2011). Monosynaptic and Polysynaptic Feed-Forward Inputs to Mitral Cells from Olfactory Sensory Neurons. *Journal of Neuroscience*, *31*(24), 8722–8729. https://doi.org/10.1523/JNEUROSCI.0527-11.2011

Negoias, S., Croy, I., Gerber, J., Puschmann, S., Petrowski, K., Joraschky, P., & Hummel, T. (2010). Reduced olfactory bulb volume and olfactory sensitivity in patients with acute major depression. *Neuroscience*, *169*(1), 415–421. https://doi.org/10.1016/j.neuroscience.2010.05.012

O'Connor, S., Angelo, K., & Jacob, T. (2012). Burst firing versus synchrony in a gap junction connected olfactory bulb mitral cell network model. *Frontiers in Computational Neuroscience*, *6*. https://doi.org/10.3389/fncom.2012.00075

Oh, S. W., Harris, J. A., Ng, L., Winslow, B., Cain, N., Mihalas, S., … Zeng, H. (2014). A mesoscale connectome of the mouse brain. *Nature*, *508*(7495), 207–214. https://doi.org/10.1038/nature13186

Omar, C., Aldrich, J., & Gerkin, R. C. (2014). Collaborative Infrastructure for Test-driven Scientific Model Validation. *Companion Proceedings of the 36th International Conference on Software Engineering*, 524–527. https://doi.org/10.1145/2591062.2591129

Orona, E., Scott, J. W., & Rainer, E. C. (1983). Different granule cell populations innervate superficial and deep regions of the external plexiform layer in rat olfactory bulb. *The Journal of Comparative Neurology*, *217*(2), 227–237. https://doi.org/10.1002/cne.902170209

Osinski, B. L., & Kay, L. M. (2016). Granule cell excitability regulates gamma and beta oscillations in a model of the olfactory bulb dendrodendritic microcircuit. *Journal of Neurophysiology*, *116*(2), 522–539. https://doi.org/10.1152/jn.00988.2015

Parasuram, H., Nair, B., D'Angelo, E., Hines, M., Naldi, G., & Diwakar, S. (2016). Computational Modeling of Single Neuron Extracellular Electric Potentials and Network Local Field Potentials using LFPsim. *Frontiers in Computational Neuroscience*, *10*. https://doi.org/10.3389/fncom.2016.00065

Peters, A., & Feldman, M. L. (1976). The projection of the lateral geniculate nucleus to area 17 of the rat cerebral cortex. I. General description. *Journal of Neurocytology*, *5*(1), 63–84. https://doi.org/10.1007/BF01176183

Phillips, M. E., Sachdev, R. N. S., Willhite, D. C., & Shepherd, G. M. (2012). Respiration drives network activity and modulates synaptic and circuit processing of lateral inhibition in the olfactory bulb. *The Journal of Neuroscience : The Official Journal of the Society for Neuroscience*, *32*(1), 85–98. https://doi.org/10.1523/JNEUROSCI.4278-11.2012

Pinching, A. J., & Powell, T. P. S. (1971). The Neuropil of the Glomeruli of the Olfactory Bulb. *Journal of Cell Science*, *9*(2), 347–377.

Pobkrut, T., Eamsa-ard, T., & Kerdcharoen, T. (2016). Sensor drone for aerial odor mapping for agriculture and security services. *2016 13th International Conference on Electrical Engineering/Electronics, Computer, Telecommunications and Information Technology (ECTI-CON)*, 1–5. https://doi.org/10.1109/ECTICon.2016.7561340

Polese, D., Martinelli, E., Marco, S., Natale, C. D., & Gutierrez-Galvez, A. (2014). Understanding Odor Information Segregation in the Olfactory Bulb by Means of Mitral and Tufted Cells. *PLOS ONE*, *9*(10), e109716. https://doi.org/10.1371/journal.pone.0109716

Pomeroy, S. L., LaMantia, A. S., & Purves, D. (1990). Postnatal construction of neural circuitry in the mouse olfactory bulb. *Journal of Neuroscience*, *10*(6), 1952–1966. https://doi.org/10.1523/JNEUROSCI.10-06-01952.1990

Pun, R. Y. K., Rolle, I. J., LaSarge, C. L., Hosford, B. E., Rosen, J. M., Uhl, J. D., … Danzer, S. C. (2012). Excessive Activation of mTOR in Postnatally Generated Granule Cells Is Sufficient to Cause Epilepsy. *Neuron*, *75*(6), 1022–1034. https://doi.org/10.1016/j.neuron.2012.08.002

Purves, D., Augustine, G. J., Fitzpatrick, D., Katz, L. C., LaMantia, A.-S., McNamara, J. O., & Williams, S. M. (2001). The Olfactory Bulb. *Neuroscience. 2nd Edition*. Retrieved from https://www.ncbi.nlm.nih.gov/books/NBK11158/

Rall, W., Shepherd, G. M., Reese, T. S., & Brightman, M. W. (1966). Dendrodendritic synaptic pathway for inhibition in the olfactory bulb. *Experimental Neurology*, *14*(1), 44–56. https://doi.org/10.1016/0014-4886(66)90023-9

Rees, C. L., Moradi, K., & Ascoli, G. A. (2017). Weighing the Evidence in Peters' Rule: Does Neuronal Morphology Predict Connectivity? *Trends in Neurosciences*, *40*(2), 63–71. https://doi.org/10.1016/j.tins.2016.11.007

Rohatgi, A. (2011). *WebPlotDigitizer*.

Royet, J. P., Souchier, C., Jourdan, F., & Ploye, H. (1988). Morphometric study of the glomerular population in the mouse olfactory bulb: Numerical density and size distribution along the rostrocaudal axis. *Journal of Comparative Neurology*, *270*(4), 559–568. https://doi.org/10.1002/cne.902700409

Rubin, D. B., & Cleland, T. A. (2006). Dynamical mechanisms of odor processing in olfactory bulb mitral cells. *Journal of Neurophysiology*, *96*(2), 555–568. https://doi.org/10.1152/jn.00264.2006

Saghatelyan, A., Roux, P., Migliore, M., Rochefort, C., Desmaisons, D., Charneau, P., … Lledo, P.-M. (2005). Activity-dependent adjustments of the inhibitory network in the olfactory bulb following early postnatal deprivation. *Neuron*, *46*(1), 103–116. https://doi.org/10.1016/j.neuron.2005.02.016

Sailor, K. A., Valley, M. T., Wiechert, M. T., Riecke, H., Sun, G. J., Adams, W., … Lledo, P.-M. (2016). Persistent Structural Plasticity Optimizes Sensory Information Processing in the Olfactory Bulb. *Neuron*, *91*(2), 384–396. https://doi.org/10.1016/j.neuron.2016.06.004

Sandberg, A., Bostrom, N., & Martin, J. (2008). *Whole Brain Emulation*. Retrieved from https://pdfs.semanticscholar.org/8af6/c8ad90372835d8ed093c7910caf876d3b2ab.pdf

Sanz Leon, P., Knock, S. A., Woodman, M. M., Domide, L., Mersmann, J., McIntosh, A. R., & Jirsa, V. (2013). The Virtual Brain: A simulator of primate brain network dynamics. *Frontiers in Neuroinformatics*, *7*. https://doi.org/10.3389/fninf.2013.00010

Schoppa, N. E., Kinzie, J. M., Sahara, Y., Segerson, T. P., & Westbrook, G. L. (1998). Dendrodendritic Inhibition in the Olfactory Bulb Is Driven by NMDA Receptors. *Journal of Neuroscience*, *18*(17), 6790–6802. https://doi.org/10.1523/JNEUROSCI.18-17-06790.1998

Schoppa, N. E., & Westbrook, G. L. (2001). Glomerulus-Specific Synchronization of Mitral Cells in the Olfactory Bulb. *Neuron*, *31*(4), 639–651. https://doi.org/10.1016/S0896-6273(01)00389-0

Scorcioni, R., Polavaram, S., & Ascoli, G. A. (2008). L-Measure: A web-accessible tool for the analysis, comparison and search of digital reconstructions of neuronal morphologies. *Nature Protocols*, *3*(5), 866–876.

Selesnick, I. W., & Burrus, C. S. (1998). Generalized digital Butterworth filter design. *IEEE Transactions on Signal Processing*, *46*(6), 1688–1694. https://doi.org/10.1109/78.678493

Shao, Z., Puche, A. C., Liu, S., & Shipley, M. T. (2012). Intraglomerular inhibition shapes the strength and temporal structure of glomerular output. *Journal of Neurophysiology*, *108*(3), 782–793. https://doi.org/10.1152/jn.00119.2012

Shen, G. Y., Chen, W. R., Midtgaard, J., Shepherd, G. M., & Hines, M. L. (1999). Computational analysis of action potential initiation in mitral cell soma and dendrites based on dual patch recordings. *Journal of Neurophysiology*, *82*(6), 3006–3020. https://doi.org/10.1152/jn.1999.82.6.3006

Shepherd. (1972). Synaptic organization of the mammalian olfactory bulb. *Physiological Reviews*, *52*(4), 864–917. https://doi.org/10.1152/physrev.1972.52.4.864

Shepherd. (2011). The Olfactory Bulb: A Simple System in the Mammalian Brain. In *Comprehensive Physiology*. Retrieved from http://onlinelibrary.wiley.com/doi/10.1002/cphy.cp010125/abstract

Shepherd, G. M., Migliore, M., & Willhite, D. C. (2010). *Olfactory Bulb*. Retrieved from https://oxfordmedicine.com/view/10.1093/med/9780195389883.001.0001/med-9780195389883-chapter-024

Short, S. M., Morse, T. M., McTavish, T. S., Shepherd, G. M., & Verhagen, J. V. (2016). Respiration Gates Sensory Input Responses in the Mitral Cell Layer of the Olfactory Bulb. *PLOS ONE*, *11*(12), e0168356. https://doi.org/10.1371/journal.pone.0168356

Shpak, G., Zylbertal, A., Yarom, Y., & Wagner, S. (2012). Calcium-Activated Sustained Firing Responses Distinguish Accessory from Main Olfactory Bulb Mitral Cells. *Journal of Neuroscience*, *32*(18), 6251–6262. https://doi.org/10.1523/JNEUROSCI.4397-11.2012

Siopi, E., Denizet, M., Gabellec, M.-M., de Chaumont, F., Olivo-Marin, J.-C., Guilloux, J.-P., … Lazarini, F. (2016). Anxiety- and Depression-Like States Lead to Pronounced Olfactory Deficits and Impaired Adult Neurogenesis in Mice. *The Journal of Neuroscience: The Official Journal of the Society for Neuroscience*, *36*(2), 518–531. https://doi.org/10.1523/JNEUROSCI.2817-15.2016

Sivagnanam, S., Majumdar, A., Kumbhar, P., Hines, M., Yoshimoto, K., & Carnevale, T. (2014). *Neuroscience Gateway–Enabling HPC for Computational Neuroscience*. Presented at the Annual Meeting, Washington DC.

Stacey, W. C., Lazarewicz, M. T., & Litt, B. (2009). Synaptic Noise and Physiological Coupling Generate High-Frequency Oscillations in a Hippocampal Computational Model. *Journal of Neurophysiology*, *102*(4), 2342–2357. https://doi.org/10.1152/jn.00397.2009

STAR: Cluster—Home. (2019). Retrieved October 15, 2019, from http://star.mit.edu/cluster/

Stroh, O., Freichel, M., Kretz, O., Birnbaumer, L., Hartmann, J., & Egger, V. (2012). NMDA Receptor-Dependent Synaptic Activation of TRPC Channels in Olfactory Bulb Granule Cells. *Journal of Neuroscience*, *32*(17), 5737–5746. https://doi.org/10.1523/JNEUROSCI.3753-11.2012

Tripathy, S. J., Savitskaya, J., Burton, S. D., Urban, N. N., & Gerkin, R. C. (2014). NeuroElectro: A window to the world's neuron electrophysiology data. *Frontiers in Neuroinformatics*, *8*, 40. https://doi.org/10.3389/fninf.2014.00040

Using the d_lambda Rule. (2019). Retrieved October 21, 2019, from https://www.neuron.yale.edu/neuron/static/docs/d_lambda/d_lambda.html

Van Rossum, G., Warsaw, B., & Coghlan, N. (2001). PEP 8: Style guide for Python code. *Python. Org*, *1565*.

Vincis, R., Gschwend, O., Bhaukaurally, K., Béroud, J., & Carleton, A. (2012). Dense representation of natural odorants in the mouse olfactory bulb. *Nature Neuroscience*, *15*(4), 537–539. https://doi.org/10.1038/nn.3057

Wang, P., Zhuang, L., Zou, Y., & Hsia, K. J. (2015). Future Trends of Bioinspired Smell and Taste Sensors. In P. Wang, Q. Liu, C. Wu, & K. J. Hsia (Eds.), *Bioinspired Smell and Taste Sensors* (pp. 309–324). https://doi.org/10.1007/978-94-017-7333-1_15

Weiss, R. D., Griffin, M. L., & Mirin, S. M. (1992). Drug Abuse as Self-Medication for Depression: An Empirical Study. *The American Journal of Drug and Alcohol Abuse*, *18*(2), 121–129. https://doi.org/10.3109/00952999208992825

White, E. L. (1973). Synaptic organization of the mammalian olfactory glomerulus: New findings including an intraspecific variation. *Brain Research*, *60*(2), 299–313. https://doi.org/10.1016/0006-8993(73)90792-0

Whitman, M. C., & Greer, C. A. (2007). Synaptic Integration of Adult-Generated Olfactory Bulb Granule Cells: Basal Axodendritic Centrifugal Input Precedes Apical Dendrodendritic Local Circuits. *Journal of Neuroscience*, *27*(37), 9951–9961. https://doi.org/10.1523/JNEUROSCI.1633-07.2007

Wilson, M. A., Bhalla, U. S., Uhley, J. D., & Bower, J. M. (1989). *GENESIS: a system for simulating neural networks*. 485–492. Morgan Kaufmann Publishers Inc.

Yu, McTavish, T. S., Hines, M. L., Shepherd, G. M., Valenti, C., & Migliore, M. (2013). Sparse Distributed Representation of Odors in a Large-scale Olfactory Bulb Circuit. *PLOS Computational Biology*, *9*(3), e1003014. https://doi.org/10.1371/journal.pcbi.1003014

Yu, Y., Burton, S. D., Tripathy, S. J., & Urban, N. N. (2015). Postnatal development attunes olfactory bulb mitral cells to high-frequency signaling. *Journal of Neurophysiology*, *114*(5), 2830–2842. https://doi.org/10.1152/jn.00315.2015

Yuksel, C. (2015). Sample Elimination for Generating Poisson Disk Sample Sets. *Computer Graphics Forum*, *34*(2), 25–32. https://doi.org/10.1111/cgf.12538

Zhang, C., & Restrepo, D. (2003). Heterogeneous expression of connexin 36 in the olfactory epithelium and glomerular layer of the olfactory bulb. *Journal of Comparative Neurology*, *459*(4), 426–439. https://doi.org/10.1002/cne.10617

Zhou, Z., & Belluscio, L. (2008). Intrabulbar Projecting External Tufted Cells Mediate a Timing-Based Mechanism That Dynamically Gates Olfactory Bulb Output. *Journal of Neuroscience*, *28*(40), 9920–9928. https://doi.org/10.1523/JNEUROSCI.3082-08.2008

Zhou, Z., & Belluscio, L. (2012). Coding odorant concentration through activation timing between the medial and lateral olfactory bulb. *Cell Reports*, *2*(5), 1143–1150. https://doi.org/10.1016/j.celrep.2012.09.035

Zhuang, L., Zhang, B., Qin, Z., & Wang, P. (2019). Nasal Respiration is Necessary for the Generation of γ Oscillation in the Olfactory Bulb. *Neuroscience*, *398*, 218–230. https://doi.org/10.1016/j.neuroscience.2018.12.011

Zibman, S., Shpak, G., & Wagner, S. (2011). Distinct intrinsic membrane properties determine differential information processing between main and accessory olfactory bulb mitral cells. *Neuroscience*, *189*, 51–67. https://doi.org/10.1016/j.neuroscience.2011.05.039